THESIS

SYNOPTIC THROUGH MESOSCALE ENVIRONMENTS OF SOUTH AMERICAN THUNDERSTORMS

Submitted by

Jeremiah Otero Piersante

Department of Atmospheric Science

In partial fulfillment of the requirements

For the Degree of Master of Science

Colorado State University

Fort Collins, Colorado

Summer 2020

Master's Committee:

Advisor: Kristen L. Rasmussen
Co-Advisor: Russ S. Schumacher

Peter A. Nelson

ABSTRACT

SYNOPTIC THROUGH MESOSCALE ENVIRONMENTS OF SOUTH AMERICAN THUNDERSTORMS

Subtropical South America east of the Andes Mountains is a global hotspot for deep convection owing to frequent mesoscale convective systems (MCSs) that contribute to over 90% of the region's rainfall and produce severe weather including large hail, flash flooding, high winds, and tornadoes. Investigations of these high impact systems through the Tropical Rainfall Measuring Mission (TRMM) satellite's precipitation radar (PR) determined that unique orographic, synoptic, and mesoscale processes initiate and maintain larger and longer-lasting MCSs in subtropical South America relative to the United States. Prior to the initiation of convection, the South American low-level jet guided by the Andes Mountains advects warm and moist air southward from the Amazon basin into the subtropics. A deep mid-level trough simultaneously approaches the mountains from the west in most cases, inducing dry mid- to upper-level subsidence flow and creating a strong capping inversion over the moist air mass. This cap is overcome via terrain-induced lift by the Andes foothills and the Sierras de Córdoba, a secondary mountain range in northern Argentina, resulting in explosive convection. These unique topographic features often act as a platform for "back-building" in which convection remains tied to the western terrain as storms propagate eastward and grow upscale; the quasi-stationary nature of MCSs inflicts considerable damage to property and agriculture in Argentina.

To improve the predictability and understanding of the physical mechanisms leading to dangerous MCSs in subtropical South America relative to those in the U.S., two studies within this thesis employ data from the recently conducted Remote sensing of Electrification, Lightning, And Mesoscale/microscale Processes with Adaptive Ground Observations (RELAMPAGO) field campaign focusing on 1) the comparison of biases in warm-season Weather Research and Forecasting model (WRF) forecasts in North and South America and 2) a synoptic through mesoscale analysis of the driving factors behind upscale growth in subtropical South America. The first study uses WRF output over North and South America verified against Stage IV analyses and radiosonde observations to contrast magnitudes and sources of forecast error between continents. It is found that the cumulus parameterization, which is most active

during the warm-season, governs biases in North American precipitation forecasts. While both continents featured a mid-level dry bias, the South American bias is greater. The second study uses TRMM PR, ERA5 reanalysis, high-resolution soundings and GOES-16 infrared brightness temperature data to identify synoptic and mesoscale phenomena that induce upscale growth varying in size and season. Synoptic forcing decreased from large to small systems and from spring to summer, suggesting that terrain-induced lift is more important in the summer. Furthermore, a case study of an MCS that exhibited rapid upscale growth during RELAMPAGO highlights the role of southerly return flow associated with the western edge of the 850-hPa lee trough on low-level convergence, vertical wind shear, and thus convection initiation. These two studies are of importance to the atmospheric science community as they enhance the understanding of some of the world's most violent thunderstorms in a region that has been notably understudied. Knowledge gained can also be applied to similar regions whose convection is also modulated by orography and provide a greater understanding of convective processes on a global scale.

ACKNOWLEDGMENTS

Working with Russ Schumacher and Kristen Rasmussen has been an absolute pleasure. Through their mentorship over the past two years, I have grown tremendously as a scientist and a collaborator. I cannot fully express my gratitude for this opportunity to join them at CSU. I would also like to thank other graduate students, postdocs, and visitors of their groups for the provoking conversations we shared on research or simply life in the atmospheric science community. Additional thanks to my third committee member, Peter Nelson, and the coauthors on my second research paper, Lynn McMurdie and Angela Rowe. Lastly, I am incredibly supported by my family and friends – their encouragement has led me to where I am today. This research was supported by National Science Foundation grants ACI-1450089 and AGS-1661657.

TABLE OF CONTENTS

CHAPTER 1

INTRODUCTION

February 8, 2018 was a normal day in Villa Carlos Paz, Argentina. Victoria Druetta was tending to her laundromat in the afternoon when dark clouds filled the sky. After living in central Argentina for years, she had grown accustomed to these conditions and knew to expect sudden claps of thunder as the atmosphere endlessly spilled water and turned the city streets into rivers. Some hail was not out of the question either. Today, however, was different: little did she know that the largest hail recorded south of the equator would soon fall beside her laundromat, a "granizo" exceeding 18 cm in maximum diameter[1] (Kumjian et al. 2020).

While subtropical South America east of the Andes Mountains is as global hotspot for large thunderstorms that feature severe weather like Victoria witnessed, deep convection is prevalent alongside other great mountain ranges across the world such as the Rocky Mountains of North America and the Himalayas of Asia (Zipser et al. 2006; Houze et al. 2015). Many past studies have focused on storm formation in the Americas in particular given similarities in their three key ingredients: 1) a poleward moisture flux east of the high terrain, 2) a capping inversion inhibiting convection formed via mid- to upper-level flow subsidence flow, and 3) a triggering mechanism such as a frontal boundary or terrain (Carlson et al. 1983; Maddox 1983; Laing and Fritsch 1997; Rasmussen and Houze 2011, 2016). The result is widespread organized convection, known commonly as a mesoscale convective system (MCS), that is responsible for a majority of warm-season precipitation (Schumacher and Johnson 2005, 2006; Nesbitt et al. 2006; Rasmussen et al. 2016) and hazardous weather such as flooding, hail, and tornadoes (Maddox 1980; Houze 2004; Rasmussen et al. 2014) thus substantially impacting the economy (e.g., agriculture and infrastructure) in addition to societal well-being. This is particularly the case in north-central Argentina, one of the most agriculturally active regions in the continent due to its flourishing wine industry.

Although MCS frequency is similar in North and South America, the precipitation areas of South American MCSs are larger and longer-lived (Velasco and Fritsch 1987; Durkee et al. 2009; Durkee and Mote 2010). Many studies attribute this to the unique terrain of subtropical South America using the Tropical Rainfall Measuring Mission (TRMM) satellite's precipitation radar (PR) to identify convective

[1] https://www.washingtonpost.com/news/capital-weather-gang/wp/2018/02/09/hail-larger-than-softballs-pummeled-an-argentina-city-on-thursday/?noredirect=on

echoes in what would otherwise be a data-sparse region of the world (Kummerow et al. 1998; Romatschke and Houze 2010; Rasmussen and Houze 2011, 2016). First, because the Andes are much taller and narrower than the Rockies, convective available potential energy and convective inhibition are greater downstream such that convection becomes more intense once triggered (Rasmussen and Houze 2016). The steeper terrain also steers a deep South American low-level jet (SALLJ) which brings increased moisture from the Amazon southward into the subtropics (Insel et al. 2010). Second, convection tends to be initiated along unique topography of the region, such as the Andes foothills or the Sierras de Córdoba, a secondary mountain range in Argentina. This causes thunderstorms to form further west and become terrain tied, leaving particular areas under severe weather conditions for hours to days (Romatschke and Houze 2010; Rasmussen and Houze 2011). It has been shown for the austral summer (DJF) that this process commences as a large mid-level trough approaches the Andes from the west, inducing a cyclone and a trough at the lee (Rasmussen and Houze 2016). Despite the frequency of severe weather and extreme rainfall in the austral spring (SON; Rasmussen et al. 2014, 2016), no studies have investigated how this may change with season.

Despite modern advances in numerical weather prediction (NWP), forecasting severe weather remains a serious challenge. The immediate issue comes from the spatial resolution used in weather forecasting models. Because regional models have horizontal grid spacing greater than 4-km, convection cannot be resolved and thus it must be parameterized by schemes that make assumptions about microscale cloud processes (Weisman et al. 1997; Bryan et al. 2003; Petch 2006). As a result, these convection schemes among others have non-negligible, inherent biases regarding storm formation and thus precipitation (Davis et al. 2003; Jankov et al. 2005; Liu et al. 2006; Clark et al. 2007). Furthermore, coarse horizontal resolution smoothes topographic details that influence convective processes which can be especially problematic in South America. The lack of understanding of convective processes and poor model performance in global hotspots like South America led to the RELAMPAGO field campaign[2] of 1 November - 17 December 2018 which provided the first ground-based observation datasets of thunderstorms and model simulations across north-central Argentina. These new data present an opportunity for understanding what makes storms in South America more intense and longer-lived than their North American counterpart. Motivated by this overarching research question, this thesis combines two studies utilizing new RELAMPAGO data to understand 1) how discrepancies arise in NWP representation of warm-season thunderstorm environments in North America vs. South America

[2]https://sites.google.com/illinois.edu/relampago/home

and 2) how synoptic and mesoscale phenomena support larger, longer-lasting MCSs in South America. Both of these investigations are critical steps to improve the prediction of devastating thunderstorms across the planet, where warnings of storm onset even hours earlier could be the difference between life and death.

To compare sources and magnitudes of model bias between North and South America warm-season environments, Chapter 2 of this thesis has the following research objectives: 1) identify which physical parameterization has the most impact on precipitation forecasts in North America, 2) compare atmospheric profile forecasts of thunderstorm environments in North and South America, and 3) investigate probable causes of this error in the context of cases in each continent. The results from this study have been submitted to *Weather and Forecasting*[3]. 1) is completed by verifying precipitation forecasts against NCEP Stage IV analysis (Lin and Mitchell 2005); an identical analysis was not performed in South America due to the lack of a robust, multi-sensor precipitation dataset in the region, but this could serve as an interesting avenue for future work. Because temperature and moisture are essential components in thunderstorm environments, we verify atmospheric profile forecasts of temperature and relative humidity against 12-hourly sounding launches for 2). Lastly, for 3), events in both continents are chosen based on moments of exceptionally high (or low) model error. Initial results suggest while thermodynamic error increases in the presence of thunderstorms, error in South America is generally greater. This does not come as a surprise given the complexities of convection initiation in the region, but it also means unique phenomena contributing to this error must be identified.

To improve the predictability of persistent MCSs in subtropical South America by addressing gaps in knowledge regarding their seasonality and size, Chapter 3 has the following research objectives: 1) investigate the evolution of synoptic scale forcing for the largest thunderstorms in South American springs relative to summers, 2) determine the relationship (if any) between thunderstorm size and scale of synoptic forcing, and 3) identify mesoscale phenomena unique to South America that help strengthen and prolong thunderstorms. These results have been submitted to *Monthly Weather Review*[4]. Like many previous studies, TRMM PR is employed for 1) and 2). Here in particular, it identifies days in subtropical South America with the largest and smallest wide convective cores (WCCs), or convective echoes of extreme horizontal dimension, in austral spring and summer. ERA5 reanalysis is then used to create time-lagged daily composites of meteorological variables surrounding the storm. This

[3]Piersante et al. (2020): Comparison of Biases in Warm-Season WRF Forecasts in North and South America

[4]Piersante et al. (2020): A Synoptic Evolution Comparison of the Largest MCSs in Subtropical South America between Spring and Summer

work adds to Rasmussen and Houze (2016) who identified the synoptic evolution of all WCCs occurring just in DJF. It is found that spring synoptic forcing is similar to but stronger than the summer. Larger storms are also associated with enhanced forcing. To address 3), we perform a case study of a widespread and long-lived MCS event that occurred during RELAMPAGO using ERA5 reanalysis coupled with GOES-16 satellite infrared temperature and mobile sounding campaign data. Specifically, we diagnose precise roles of the LLJ, mid- to upper-level subsidence flow, and unique terrain on prolonged convection. These studies presented herein are of value to the meteorology community because they make use of new data that will continue to propel the understanding and prediction of storms with extreme characteristics in South America which can be applied to similar regions of the world.

CHAPTER 2

COMPARISON OF BIASES IN WARM-SEASON WRF FORECASTS IN NORTH AND SOUTH AMERICA

20-km horizontal resolution Weather Research and Forecasting Model ensembles with varying parameterizations are used to investigate and compare precipitation and atmospheric profile forecast biases in North and South America. By verifying a 19-member ensemble against NCEP Stage IV precipitation analyses, it is shown that the cumulus parameterization (CP), in addition to precipitation amount and season, has the largest influence on precipitation forecast skill in North America during 2016-2017. Verification of an ensemble subset against operational radiosondes in North and South America finds that forecasts in both continents feature a substantial mid-level dry bias, particularly at 700 hPa, during the warm season. Case-by-case analysis suggests that large mid-level error is associated with mesoscale convective systems (MCSs) east of the high terrain and westerly subsidence flow from the Rocky and Andes Mountains in North and South America. However, error in South America is consistently greater than North America. This is likely attributed to the complex terrain and higher average altitude of the Andes relative to the Rockies, which allow for a deeper low-level jet and long-lasting MCSs, both of which 20-km simulations struggle to resolve. In the wake of data availability from the RELAMPAGO field campaign, the authors hope that this work motivates further comparison of large precipitating systems in North and South America, given their high impact in both continents.

2.1 INTRODUCTION

North and South America are home to two of the world's largest mountain ranges: the Rocky and Andes Mountains. The altitude of these barriers, north-south orientation, and their position on the western side of the continents lead to substantial influences on the weather downstream because they modify midlatitude westerly and other associated flows. Interestingly, the regions east of the mountainous terrain in both continents are global hot spots for deep and organized convection, owing to the frequent occurrence of mesoscale convective systems (MCSs; Velasco and Fritsch 1987; Laing and Fritsch 1997; Houze 2004; Zipser et al. 2006; Houze et al. 2015).

Generally, convection initiation for MCSs in both continents involves the same key ingredients: 1) a poleward flux of low-level moisture from the Gulf of Mexico or the Amazon via the low-level jet (LLJ), 2) a capping inversion that prolongs the release of instability via westerly mid- to upper-level dry air subsidence from the high terrain, and 3) a lifting mechanism (Carlson et al. 1983; Maddox 1983; Laing and Fritsch 1997; Rasmussen and Houze 2011, 2016). A combination of these key ingredients east of the

high terrain of the Rockies and Andes results in environments favorable for deep and organized convection in both continents, although some evidence suggests that extreme storms in South America may be deeper and more frequent than in North America (Zipser et al. 2006; Houze et al. 2015). Elevated mixed layers (EMLs) are also associated with hazardous weather with southwesterly upper-level flow over the high terrain in North America and northwesterly flow in South America due to an anomalously strong upper-level trough over the mountains (Rasmussen and Houze 2016; Cordeira et al. 2017; Ribeiro and Bosart 2018). These large clusters of thunderstorms produce various forms of severe weather with substantial socioeconomic impacts such as extreme rainfall and flooding, hail, strong winds, and tornadoes in both regions (Maddox 1980; Schumacher and Johnson 2005, 2006; Romatschke and Houze 2010; Cecil and Blankenship 2012; Rasmussen and Houze 2011; Rasmussen et al. 2014). Several previous studies show that MCSs contribute 30-70% of warm-season precipitation in the U.S. (Fritsch et al. 1986; Durkee et al. 2009; Haberlie and Ashley 2019) and up to 95% of summertime precipitation in subtropical South America (Nesbitt et al. 2006; Romatschke and Houze 2010; Rasmussen et al. 2016).

However, despite the similarities in environmental conditions and storm impacts in both regions, there are several important differences among South American mesoscale features that suggest the convection of the region may be deeper and more frequent. For example, MCSs and their precipitation areas in South America tend to be substantially larger and longer-lived (Velasco and Fritsch 1987; Durkee et al. 2009) and occur over a smaller and more focused region east of the Andes Mountains in northern Argentina: the greater La Plata Basin (Zipser et al. 2006; Romatschke and Houze 2010; Rasmussen et al. 2016). It is also common for the main convective area of South American MCSs in this region to propagate upstream, opposing the low-level jet and moisture flux (Anabor et al. 2008). These systems resemble a more robust version of the "southward burst" observed in North America (Porter et al. 1955; Stensrud and Fritsch 1993) as they can support convection lasting anywhere from 19 to 69 hours (Anabor et al. 2008). This contrast is largely due to the complex terrain and deep LLJ of South America (referred to as the South American Low-Level Jet; SALLJ). Though narrower, the Andes are approximately double the average altitude of the Rocky Mountains and block low- to mid-tropospheric westerly flow, allowing for a much stronger northerly moisture flux along the terrain and enhanced lee cyclogenesis (Insel et al. 2010; Rasmussen and Houze 2016). Air then converges near the Andes foothills and the Sierras de Córdoba (SDC), a secondary north-south-oriented mountain range in northern Argentina, which provides enhanced lift to trigger deep convective cores and keep their western edge

tied to the terrain while they grow upscale towards the east (Rasmussen and Houze 2011, 2016; Rasmussen et al. 2014). This "back-building" phenomenon leads to persistent convection and is unique to subtropical South America (Rasmussen et al. 2014).

Previous studies describe the relative depth and role of the SALLJ in convective initiation and contribution to regional rainfall (Marengo et al. 2002, 2004; Salio et al. 2002, 2007; Guedes do Nascimento et al. 2016), but use LLJ identification criteria originally designed for North America (Bonner 1968) that neglects SALLJs in the La Plata Basin that are elevated and/or feature a strong zonal component. Oliveira et al. (2018) created new criteria to address this shortcoming and found SALLJs often reach 700 hPa in and near the La Plata Basin, making them much deeper than their North American counterpart. These findings are similar to those observed in Bolivia and western Paraguay during the South American Low-Level Jet Experiment (SALLJEX; Vera et al. 2006).

Given these impacts and complex initiation modes of MCSs, there is a serious demand for numerical weather prediction (NWP) to accurately represent and forecast such events. Unsurprisingly, convection-permitting models yield the most accurate forecasts, particularly when it comes to warm-season precipitation at long and short forecast lead times, such as the National Center for Atmospheric Research (NCAR) convection-allowing ensemble and the Storm Scale Ensemble Forecast system (Clark et al. 2009; Clark and Coauthors 2012; Schwartz et al. 2015; Iyer et al. 2016). However, these simulations at 1-4 km horizontal resolution, or those truly resolving convection at 100 m, can be computationally expensive (Weisman et al. 1997; Bryan et al. 2003; Petch 2006). As a result, convective parameterizations (CPs) are widely used with coarser resolutions for practical reasons, but carry inherent biases in precipitation forecasts (Davis et al. 2003; Jankov et al. 2005; Liu et al. 2006; Clark et al. 2007; Jeworrek et al. 2019).

Few studies have investigated model performance and parameterization dependence in environments conducive to large precipitating MCSs in South America. Blázquez and Nuñez (2009) reaffirm that CPs have a large influence on accumulated warm-season precipitation, but they verify against reanalysis as opposed to in situ measurements and neglect to explore the accuracy of thermodynamic environment forecasts. Ruiz et al. (2010) shows the tendency for models to underestimate SALLJ strength in addition to the influence of CPs and other parameterizations on precipitation and surface variables; however, this study lacks a direct comparison between CPs and surface variable biases. Müller et al. (2016) analyze precipitation and surface temperature forecasts over various forecast lead times, but use the same model configuration throughout.

Clearly, there has yet to be a robust model verification analysis of atmospheric conditions favorable for MCSs and extreme rainfall, such as temperature, relative humidity, and wind in South America. While surface observations are widespread and available for ensemble-based forecast verification of extreme rainfall and the associated environmental characteristics in North America (Schumacher and Davis 2010; Schumacher and Clark 2014), there is a significant lack of consistent and available observation data in South America, creating challenges in verifying operational model data in this region and also assimilating observations into models to increase their performance. Fortunately, field campaigns such as SALLJEX (Vera et al. 2006) and RELAMPAGO[1] in north-central Argentina provide useful observational data. The latter ensured that most surface stations in Argentina were functioning throughout the campaign, which took place November-December 2018.

The primary goal of this study is to evaluate and compare model forecasts of atmospheric conditions during boreal and austral warm seasons of North and South America, respectively, considering the potential impacts of subsidence flow and the LLJ on convective, heavily precipitating systems set forth by previous work. First, we examine the effects of CP on precipitation forecasts in North America, using a multi-sensor gridded precipitation analysis. Second, we use multiple CPs to assess atmospheric profile forecast error and address the spread between them. We end with investigating interesting cases in each continent to test our hypotheses and exemplify our results.

2.2 Methodology

This study consists of three parts: 1) precipitation forecast evaluation in North America, 2) atmospheric profile forecast evaluation in both North and South America, and 3) analysis of North and South American cases based on results in 2).

2.2.1 Precipitation Forecast Evaluation

Model statistics on precipitation forecast accuracy are calculated over a domain covering the contiguous United States (CONUS). We use the Big Weather Web (BWW; Maltzahn and Coauthors 2016) ensemble to compare forecasts of many members with respect to varying parameterizations. The BWW ensemble subset for this study consists of 19 members with 20-km grid spacing initialized daily at 0000 UTC from February 2016 to July 2017 by various universities over CONUS. All members were run via the Advanced Research Weather and Forecasting model (WRF; Skamarock and Klemp 2008) version 3.7.1 with RRTMG radiation (Houze et al. 2008), Noah land surface (Tewari et al. 2004), 43 vertical levels, and

[1] https://sites.google.com/illinois.edu/relampago/home

a 90-second timestep, but each member uses different initial/lateral boundary conditions, and physical parameterizations (cumulus, PBL, microphysics). The ensemble setup is summarized in Table 2.1; the first two members are also used in the atmospheric profile evaluation.

The authors used METv8.0 (Gotway and Coauthors 2018) to verify precipitation forecasts against NCEP Stage IV analyses (Lin and Mitchell 2005), regridded to the BWW forecast grid. Quantitative precipitation forecast (QPFs) were evaluated on a grid-by-grid basis using the Gilbert Skill Score (GSS; see Gotway and Coauthors 2018) and Roebber Performance Diagrams (Roebber 2009). GSS measures how well forecast "yes" precipitation events correspond to observed "yes" events, taking into account random chance:

$$GSS = \frac{Hits - Hits_{random}}{Hits + Misses + FalseAlarms - Hits_{random}}$$

where

$$Hits_{random} = \frac{(Hits + FalseAlarms)(Hits + Misses)}{Total}$$

and a *Hit* is an accurate forecast "yes" on a grid, a *Miss* is a forecast "no" on an observed "yes", and a *False Alarm* is a forecast "yes" on an observed "no". GSS ranges from $-\frac{1}{3}$ to 1 with 0 indicating zero skill and 1 perfect skill.

TABLE 2.1. BWW ensemble member setup employed for this study. All members were used for precipitation forecast evaluation; only CSU01 and CSU02 (italics) were used for atmospheric evaluation. Cumulus schemes include Kain (2004); Grell and Freitas (2014); New Tiedtke (Zhang and Wang 2017); Tiedtke (Zhang et al. 2011). Microphysics schemes include Thompson et al. (2008); Morrison et al. (2009); WRF single-moment 6-class microphysics scheme (WSM6; Hong and Lim 2006); Milbrandt and Yau (2005). Planetary boundary layer (PBL) schemes include Yonsei University scheme (YSU; Hong et al. 2006); Mellor-Yamada-Janjić scheme (MYJ; Janjić 1994); asymmetric convection model 2 scheme (ACM2; Pleim 2007); Grenier-Bretherton-McCaa scheme (GBM; Grenier and Bretherton 2001); Mellor-Yamada Nakanishi Niino level 2.5 scheme (MYNN; Nakanishi and Niino 2009).

Member	**LC/IBC**	**Cumulus**	**PBL**	**Microphysics**
CSU01	GFS 0.5°	Kain-Fritsch	MYJ	Thompson
CSU02	GFS 0.5°	Grell-Freitas	MYJ	Thompson
ALB01	GFS 0.5°	Kain-Fritsch	MYJ	Thompson
ALB02	GEFSP01	Kain-Fritsch	MYJ	Thompson
ALB03	GFS 0.5°	Kain-Fritsch	YSU (top-down)	Thompson
ALB04	GFS 0.5°	Kain-Fritsch	ACM2	Thompson
ALB05	GFS 0.5°	New Tiedtke	MYJ	Thompson
ALB06	GFS 0.5°	Kain-Fritsch	YSU (no top-down)	Thompson
ALB07	GFS 0.5°	Kain-Fritsch	GBM	Thompson
ALB08	GFS 0.5°	New Tiedtke	MYJ	Thompson
TTU01	GFS 0.5°	Tiedtke	YSU	Morrison
TTU02	GFS 0.5°	Tiedtke	MYNN	Morrison
TTU03	GFS 0.5°	Tiedtke	YSU	Thompson
TTU04	GFS 0.5°	Tiedtke	MYNN	Thompson
TTU05	GFS 0.5°	Tiedtke	YSU	WSM6
TTU06	GFS 0.5°	Tiedtke	MYNN	WSM6
PSU08	GFS 0.5°	Kain-Fritsch	YSU	Milbrandt-Yau
UND01	GFS 0.5°	Kain-Fritsch	MYJ	WSM6
UND02	GFS 0.5°	Grell-Freitas	YSU	Morrison

The Roebber Performance Diagram is used to simultaneously plot Success Ratio (SR; 1 - False Alarm Ratio) and Probability of Detection (POD), and also reveals the critical success index (CSI) and frequency bias. Here, greater skill is represented by an increase in these ratios at 45°. An instance in which POD > SR indicates a wet model bias, and the opposite for a dry bias. An identical analysis is not possible in South America due to a lack of a suitable high-resolution multi-sensor precipitation analysis in the region. This is an interesting area for future work; however, the precipitation evaluation results in North America adequately motivate the atmospheric forecast evaluation (methodology outlined below).

2.2.2 Atmospheric Profile Forecast Evaluation

Routine evaluation of daily BWW forecasts over CONUS indicated there were substantial differences in upper-level temperature and humidity between ensemble members with different CPs. Given this finding and the availability of members at Colorado State University, the authors selected CSU01 and CSU02 with Kain-Fritsch (KF) and Grell-Freitas (GF) CPs, respectively, for the atmospheric profile evaluation in North and South America (Table 2.1). CSU01 and CSU02 in North and South America are identical except for the domain, WRF Version (3.8 in South America), and timeframe, as South America runs were initially used for forecasting during the RELAMPAGO field campaign from 4 October 2018 through 23 February 2019. For the majority of the analysis, we compare the 2018/19 South America warm season to the 2016 North America warm season (initializations from 1 May to 30 September). In *Section 2.4.2*, however, we consider these biases across seasons in North America given the availability of observational soundings and BWW output from January 2016 through October 2017.

Forecasts were verified against operational radiosonde observations occurring daily at 0000 and 1200 UTC (NCEP 2004). These observation locations, topographic features, and other notable landmarks in each continent are presented in Figure 2.1. Both study domains capture the Rocky and Andes Mountains in the west, the plains in the east, and the coastal regions of the Gulf of Mexico and the Atlantic. While the Rockies are wider, the Andes are much taller. The SDC is highlighted east of the high terrain in addition to Mendoza and Córdoba cities, all of which were major focal points of RELAMPAGO (Fig. 2.1b). South America clearly has fewer observation stations than North America (Fig. 2.1a). Furthermore, most South America locations lacked consistent daily 0000 UTC observations (Table 2.2). This was particularly the case for locations in Argentina; Mendoza and Córdoba sites halted observations at the conclusion of RELAMPAGO's intensive observation period in mid-December. September 2016 in North America also had very few 0000 UTC observation/verification pairings, a result of the failure to initialize the model throughout most of the month. We focus on 0000 UTC verification times as this is when most stations tended to take observations, but few, such as Buenos Aires, performed most at 1200 UTC.

We focus our analysis on relative humidity (RH) and temperature at various pressure levels throughout the atmosphere, enabling a model bias assessment of thermodynamic environments that could influence MCSs and large-scale precipitation events. While RH is not an absolute moisture variable as it depends on temperature, it best represents the impacts of clouds and convection, which is what the

CP attempts to describe. We also assess meridional wind (v-component wind) to identify potential LLJ errors.

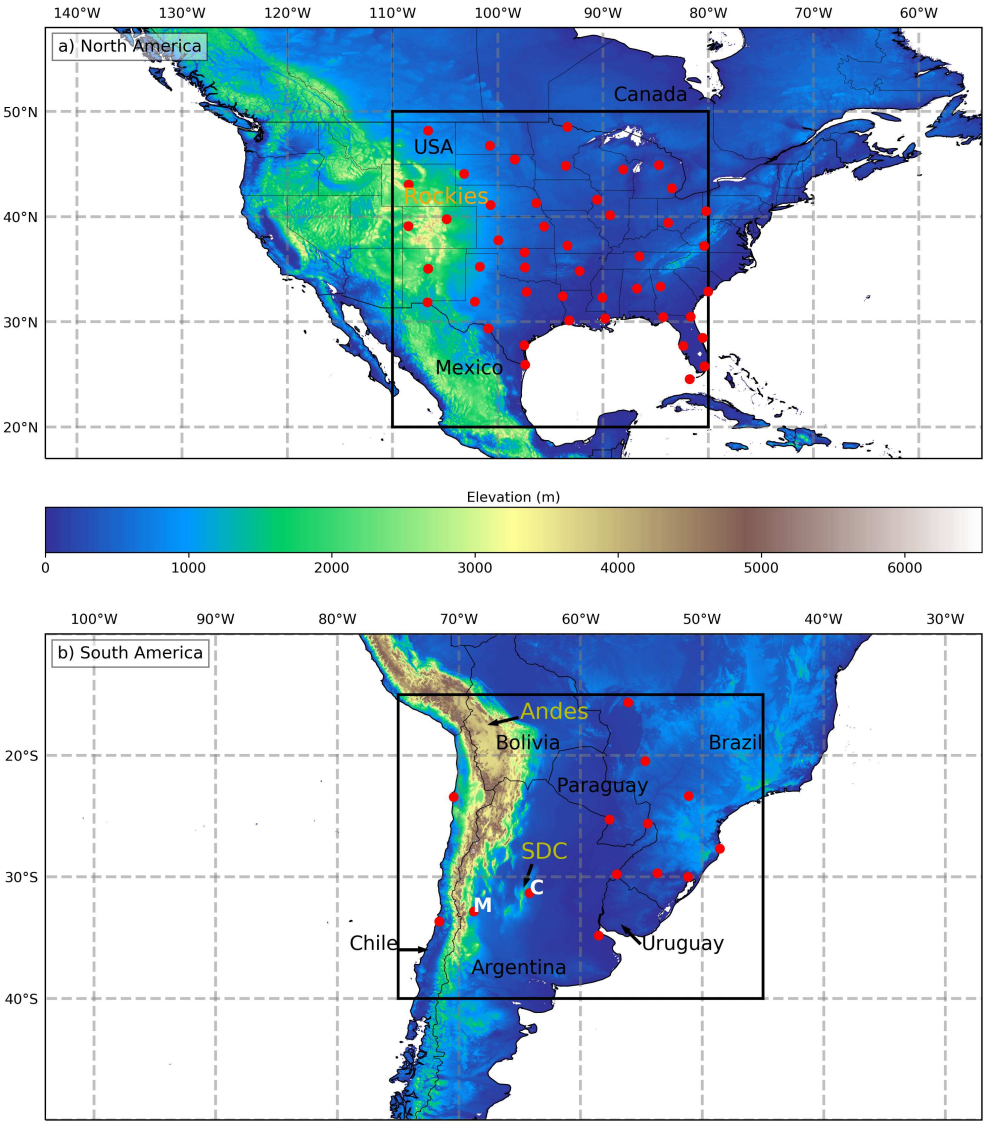

FIG. 2.1. North and South America model domains (entire panel), study domains for this work (black boxes) and radiosonde observation locations (red dots) used for this study. Topographic contours highlight the Rocky Mountains (a) and the Andes Mountains and the Sierras de Córdoba (SDC; b). M and C (b) represent Mendoza and Córdoba cities.

METv8.0 was also implemented to calculate point verification statistics, namely the bias and root mean square error (RMSE):

$$bias = forecast - observation$$

$$RMSE = \sqrt{\frac{1}{n}\sum_{i=1}^{n}(forecast - observation)^2}$$

TABLE 2.2. Number of 24-hr RH forecast observation/verification pairings at 0000 UTC per station in South America (all stations) and North America (most frequent 14 stations) during 4 October 2018 - 23 February 2019 and 1 May - 30 September 2016, respectively.

South America			# Monthly Observations				
LAT	**LON**	**City**	**Oct**	**Nov**	**Dec**	**Jan**	**Feb**
-29.70	-53.68	Santa Maria (SBSM)	22	30	31	29	21
-27.67	-48.55	Florianópolis (SBFL)	22	30	21	30	19
-20.47	-54.67	Campo Grande (SBCG)	22	30	31	29	20
-25.60	-54.48	Foz de Iguacu (SBFI)	22	29	31	30	21
-29.78	-57.03	Uruguaiana (SBUG)	21	25	28	28	21
-25.52	-49.17	Curitiba (SBCT)	21	27	30	29	20
-30.00	-51.18	Porto Alegre (SBPA)	18	30	31	29	21
-15.65	-56.10	Várzea Grande (SBCY)	17	20	25	19	17
-19.00	-57.67	Corumbá (SBCO)	10	0	0	0	0
-33.65	-71.62	Santo Domingo (SCSN)	5	28	26	28	21
-34.82	-58.53	Buenos Aires (SAEZ)	1	0	1	0	0
-32.83	-68.78	Mendoza (SAME)	0	29	14	0	0
-31.31	-64.21	Córdoba (SACO)	0	29	16	6	0
-27.45	-59.05	Resistencia (SARE)	0	2	0	0	0
		Total	**181**	**309**	**285**	**257**	**181**
North America			# Monthly Observations				
LAT	**LON**	**City**	**May**	**Jun**	**Jul**	**Aug**	**Sep**
33.36	-84.57	Atlanta (KATL)	28	29	29	27	5
37.21	-80.41	Blacksburg (KBCB)	28	29	29	27	5
48.21	-106.63	Glasgow (KGGW)	28	29	29	27	5
39.77	-104.87	Denver (KDNR)	28	29	29	27	5
29.37	-100.92	Del Rio (KDRT)	28	29	29	27	5
30.45	-84.30	Tallahassee (TAE)	28	29	29	27	5
44.91	-84.72	Gaylord (APX)	28	29	29	27	5
39.42	-83.82	Wilmington (ILN)	28	29	29	27	5
42.70	-83.47	Detroit/Pontiac (DTX)	28	29	29	27	5
36.25	-86.56	Nashville (OHX)	28	29	29	27	5
32.84	-97.30	Fort Worth Meacham (KFTW)	28	29	29	27	5
31.94	-102.19	Midland (KMAF)	28	29	29	27	5
37.24	-93.40	Springfield-Branson (KSGF)	28	29	29	27	5
44.50	-88.11	Green Bay NWS (KGRB)	28	29	29	27	5
		Total	**392**	**406**	**406**	**378**	**70**

Following the North America precipitation forecast evaluation in *Section 2.3*, we first compare RH and temperature profile biases between continents and CPs at various forecast lead times. We then assess the temporal evolution of RH error with respect to lead time and the seasonal cycle, followed by

the spatial distribution of the RH and meridional wind error among similar North and South America months.

2.2.3 North and South American Case Analysis

Lastly, we highlight particular events in each warm season with substantial errors (or lack thereof) and attempt to diagnose the probable causes of each. For South America, we choose an MCS case during RELAMPAGO given its complex structure, spatial and temporal extent, likelihood of inducing widespread forecast error, and data availability. It also featured elements of upstream propagation, a phenomenon described by Anabor et al. (2008). Helpful tools and resources used for this analysis include the NOAA Hybrid Single-Particle Lagrangian Integrated Trajectory model (HYSPLIT; Stein et al. 2015) for determining parcel backward trajectories via GDAS 1° reanalysis in addition to GOES-16 infrared (IR) temperature and NEXRAD radar[2] for storm identification in South and North America, respectively.

2.3 Precipitation Forecast Evaluation in North America

GSS of 36-60-hr QPF, especially for 50.8 mm over CONUS, has a clear seasonal dependence (Fig. 2.2), maximizing in the cool months (e.g., October 2016) and minimizing in the warm months (e.g., July 2016 and May 2017). Members with the same CP also tended to cluster together (Fig. 2.3). Most notably, the Tiedtke CP had greater skill in the 2016/17 cool months (Figs. 2.2, 2.3c).

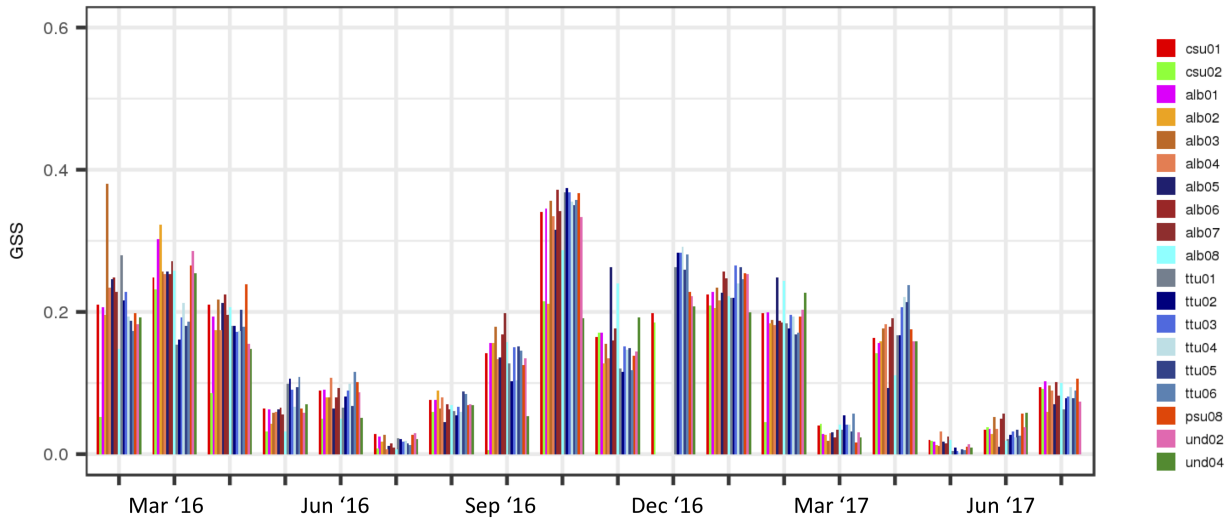

FIG. 2.2. Gilbert Skill Score (GSS) for 36-60-hour QPF 50.8 mm threshold over CONUS for the members shown in Table 2.1 during February 2016 through July 2017. Color distinguishes CP: warm colors indicate KF, green GF, and blue Tiedtke.

[2]http://www2.mmm.ucar.edu/imagearchive/

Forecast skill is greatest at lower precipitation amounts year-round (Fig. 2.3a). CP schemes cluster together the most during the warm season (May-August) when the scheme is most active within the model (Fig. 2.3b). KF members featured a wet bias at lower precipitation amounts, but became less biased at higher amounts. Tiedtke members on the other hand were nearly unbiased at lower amounts, especially during the non-warm season. New Tiedtke members (ALB08 and ALB05) were exceptionally dry at higher amounts in the non-warm season, however (Fig. 2.3c). GF members fell between KF and New Tiedtke members at all amounts. These results are very similar to those in Jeworrek et al. (2019) where GF precipitation forecasts of similar resolution were the most accurate during convective events in the southern Great Plains of the U.S.

CP has the most evident influence on precipitation forecasts compared to other parameterizations in Table 2.1, a conclusion also drawn in Jeworrek et al. (2019). Acknowledging these CP biases is crucial from a forecasting and regional climate analysis standpoint; depending on the application, it might be preferable to be unbiased at high amounts and accept the high bias at low amounts, or alternatively to be unbiased at low amounts that are more frequent.

Though we did not perform an identical analysis in South America, Blázquez and Nuñez (2009) have shown warm-season precipitation forecasts in South America are also substantially impacted by the choice of CP. In *Section 2.4*, we begin the comparison of atmospheric profile forecast biases between North and South America using Kain-Fritsch (KF) and Grell-Freitas (GF) CPs. This allows for identifying differences in bias characteristics associated with these CPs between the different regions.

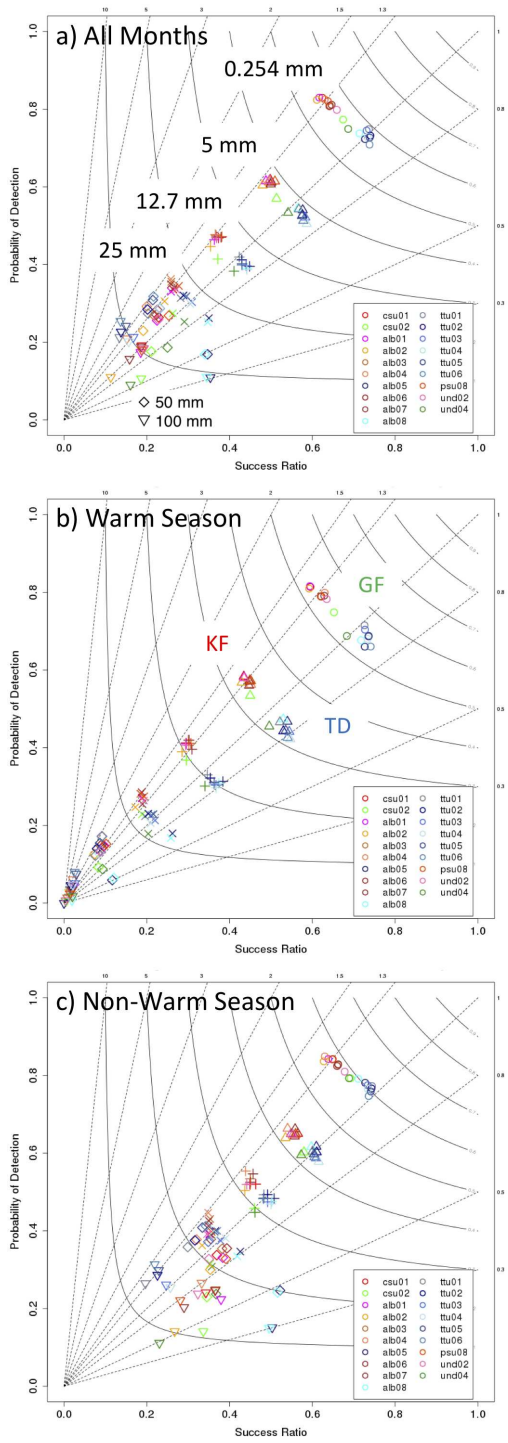

FIG. 2.3. Roebber Performance Diagrams of ensemble members at various precipitation amounts during February 2016 - July 2017 over (a) all months, (b) warm season months (May - August), and (c) non-warm season months. Shape distinguishes precipitation amount and color indicates CP as in FIG. 2.2.

2.4 Atmospheric Profile Evaluation in North and South America

2.4.1 Profile Biases

RH forecast bias, averaged across the 2018/19 (South America) and 2016 (North America) warm seasons, is strongly influenced by continent, CP, and forecast lead (Fig. 2.4). Upon model initialization, a slight wet bias already existed at all levels except for at 925 hPa in South America (Fig. 2.4a). CPs were equal at this time since there had been zero model spin-up; errors are differences between the GFS initial conditions and the point observations.

With a 24-hr forecast lead, the mid-levels, namely 700 hPa, were too dry with the greatest overall bias in South America and with GF approaching -10% (Fig. 2.4b). One continental contrast is that North America featured a wet bias at 925 and 300 hPa for both CPs, where South. America was slightly too dry at 925 hPa and nearly unbiased at 300 hPa (Fig. 2.4b). These trends became more robust with 48- and 72-hr leads: South America GF was nearly -15% at 700 hPa with South America KF not far behind (Fig. 2.4c,d). In general, a mid-level dry bias grew with increased lead time and error maximized in South America and with GF.

There are also notable temperature biases within both continents (Fig. 2.5). Both continents featured a slight cool bias at most levels upon initialization, and like RH, bias was equal among CPs (Fig. 2.5a). At 24-hrs, all agreed on a warm bias slightly less than 1 K at 700 hPa (Fig. 2.5b), becoming greater, particularly for North America runs, at longer forecast leads (Fig. 2.5c,d). There was less agreement aloft and near the surface, however. GF was nearly unbiased at 200 and 300 hPa where KF was slightly cool for both North and South America. North America KF was the warmest at 850 hPa, but there was no clear worst performer at 925 hPa (Fig. 2.5c,d). These results are quite different from those in Grell and Freitas (2014) who found a low-level cool and moist bias and an upper-level warm and dry bias for South America forecasts also using 20-km GF schemes (their Fig. 14). Their verification, however, only focused on a 15-day period in January over the Amazon—the predominant moisture source of the subtropics. The domain in the current study on the other hand relies on the southward advection of moisture from the Amazon via the SALLJ, a process we hypothesize that 20-km models struggle representing and thus likely explaining the discrepancy in GF atmospheric profile verification.

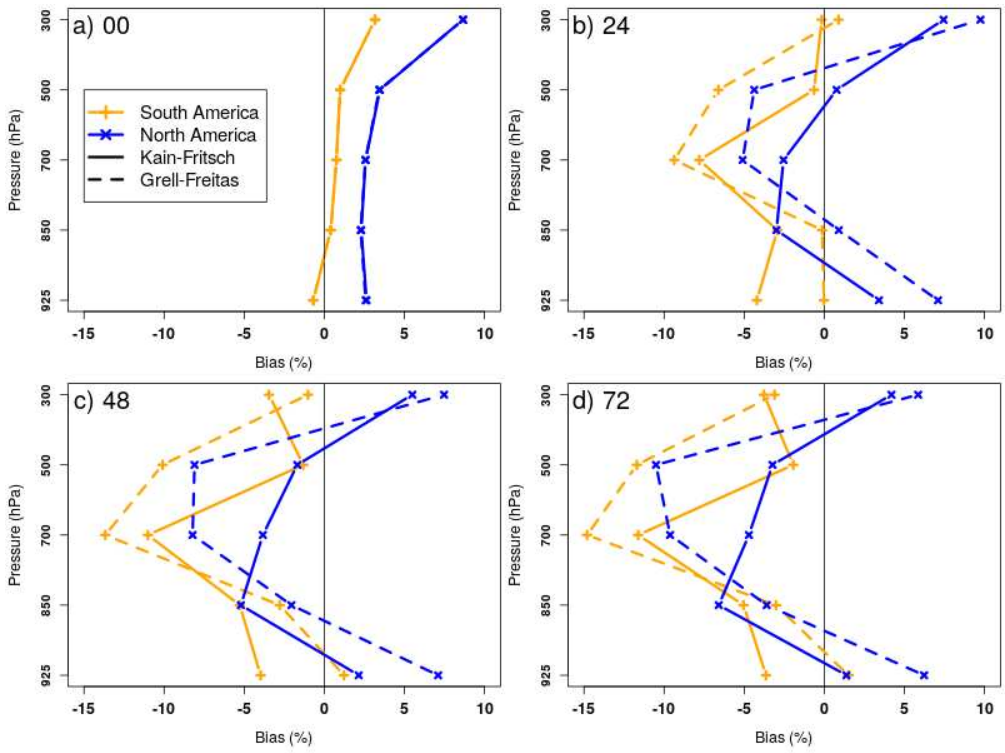

FIG. 2.4. Mean RH forecast bias at various pressure levels (vertical axes) at forecast leads of (a) 00, (b) 24, (c) 48, and (d) 72-hrs. Yellow (blue) indicates South America (North America), and filled (dashed) lines indicate Kain-Fritsch (Grell-Freitas) cumulus parameterization. Biases were calculated by averaging all available stations in the respective domain and warm seasons (4 October 2018 through 23 February 2018 for South America; 1 April 2016 through 30 September 2016 for North America).

This consistent mid-level warm bias partially explains the mid-level low RH bias in Figure 2.4, given that increasing temperature with constant moisture decreases RH. Interestingly, however, North America KF had the warmest bias here (Fig. 2.5d) yet South America GF had the driest (Fig. 2.4d). Furthermore, a warm bias did not always coincide with a dry bias, as seen with South America runs at 300 hPa at 24-hrs (Figs. 2.4b,2.5b). For the remainder of this study, we focus on this bias maximum at 700 hPa and attempt to explain its probable causes. This level is important for models to accurately represent because the SALLJ transports a non-negligible amount of moisture towards the region of convective development even this high in the atmosphere.

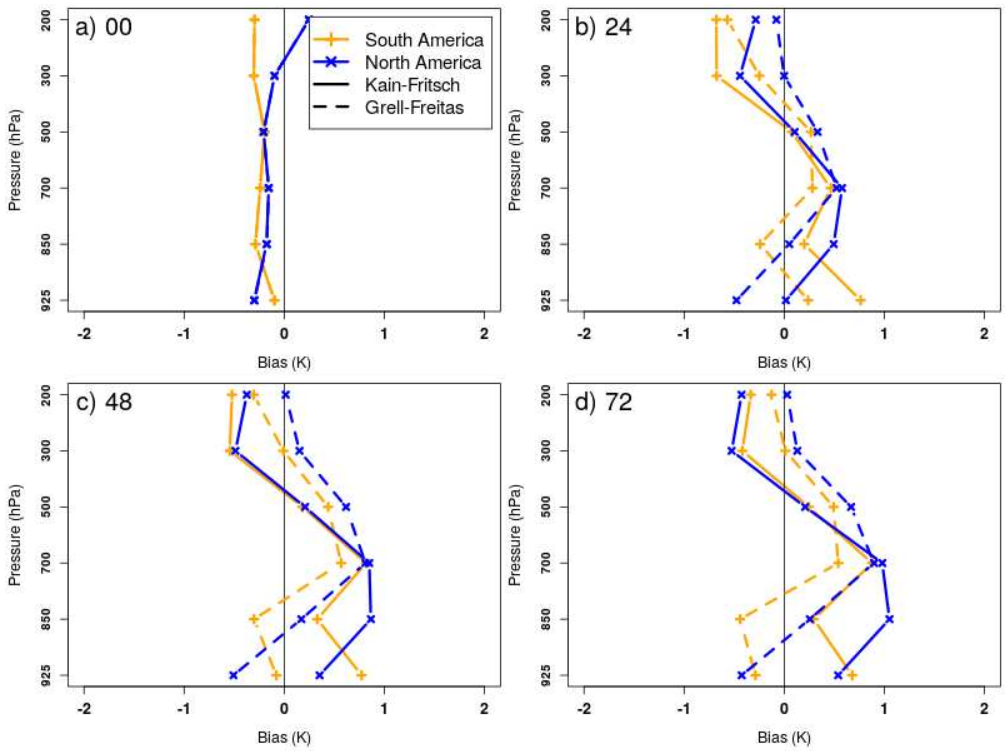

FIG. 2.5. As in FIG. 2.4, for mean temperature bias. Note that 200 hPa was available for temperature but not RH.

2.4.2 Relative Humidity Temporal Variation

As seen in Figures 2.4 and 2.5, forecast lead time influences temperature and RH bias. The overall error (RMSE) for 700 hPa RH forecasts grows with increased lead time (Fig. 2.6). All runs on average begin with 12% RMSE upon initialization, and increase to anywhere from 21-30% as lead increases to 84 hrs. Again, more error occurs in South America and with GF. The increase in RMSE is smaller from 0000 to 1200 UTC verification (e.g., 24- to 36-hrs), and even is a decrease with South America longer lead times. This is likely influenced by morning vs. evening verification and fewer 1200 UTC observations available in South America.

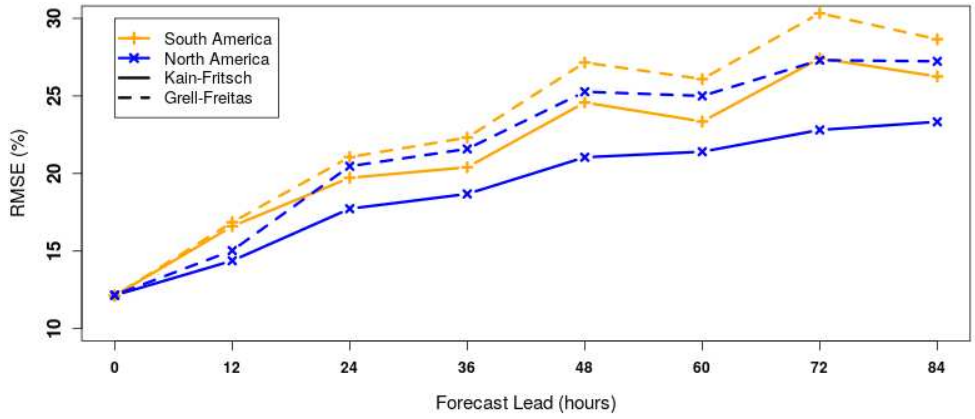

FIG. 2.6. Root mean square error (RMSE) for 700 hPa relative humidity at various forecast lead times, in hours. Colors and line styles match those described in FIG. 2.4.

We can look at 24-hr bias across many months in North America given the availability of both observational soundings and BWW output to find that the type of error also varies with season: a dry (wet) bias occurred during the warm (cool) season in North America, with maximum error in the middle of each season (Fig. 2.7b). While GF error was greater than that of KF in the warm season, the opposite was true in the cool season (Fig. 2.7b). The one South America warm season also showed the same trend as the North America warm season, except bias continued to grow through February 2019 (Fig. 2.7a). We believe this is due to a lack of active stations, and thus a smaller sample size, within the domain in the latter half of this warm season and discuss this further within the context of a particular case in *Section 2.5*. Lastly, as seen before, the South America error was greater than North America during the warm season (Fig. 2.7). To summarize, in both regions, the mid-level dry bias discussed above is most prominent in the warm season, when deep convection is most frequent and the CP schemes are presumably most active.

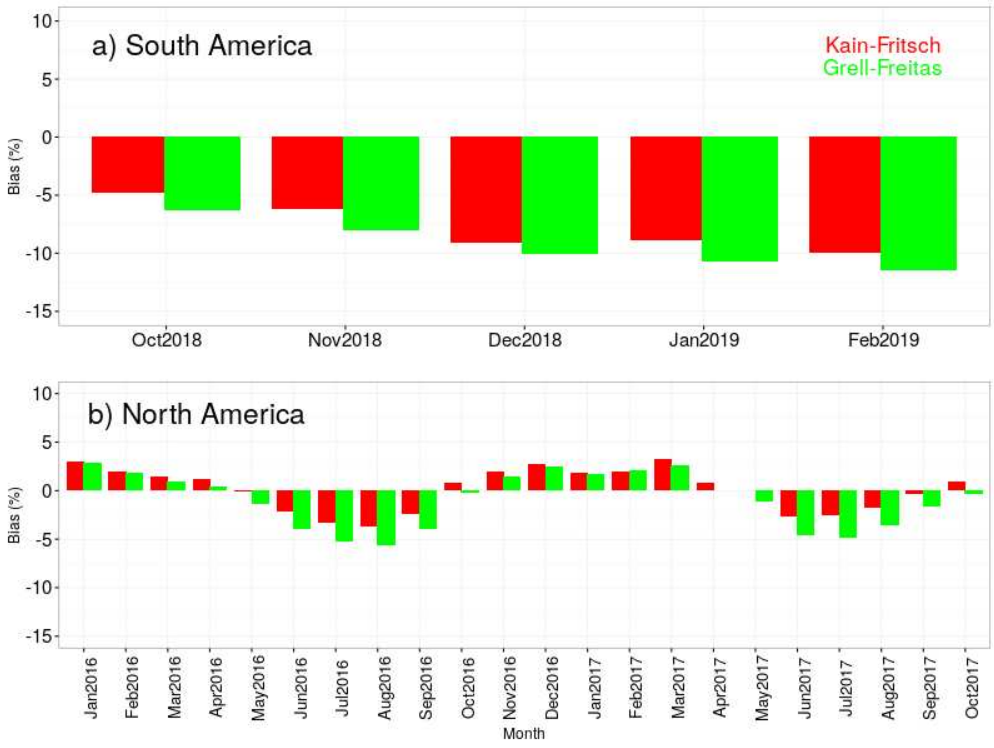

FIG. 2.7. Average monthly RH bias for 24-hr 700 hPa forecasts using Kain-Fritsch (red; left bars) and Grell-Freitas (green; right bars) in (a) South America and (b) North America.

2.4.3 Relative Humidity and Meridional Wind Spatial Variation

December 2018 and June 2016 for South and North America, respectively, exemplified the warm season mentioned above and consisted of enough observations to make direct comparisons between continents (Table 2.2). The following results were similar for KF and GF, but we present GF biases particularly at 24 hrs as they already exceeded 20% RMSE (Fig. 2.6) and were greater overall. On average, 24-hr forecasts for 700 hPa RH using GF were too dry at almost every location in South America, many of which exceeded 20% (Fig. 2.8a). Most of these also featured an equatorward meridional wind bias, thus underrepresenting the SALLJ and the poleward moisture flux. Closer to the high terrain, Córdoba on average also featured a strong equatorward meridional wind bias (2.8 m s^{-1}) in association with a 10% dry bias. Mendoza on the other hand had a greater dry bias in tandem with a slight poleward meridional wind bias (Fig. 2.8a). Its proximity to the Andes Mountains is likely a key influence on this difference as the topography, and thus the wind, is smoothed in the model simulation.

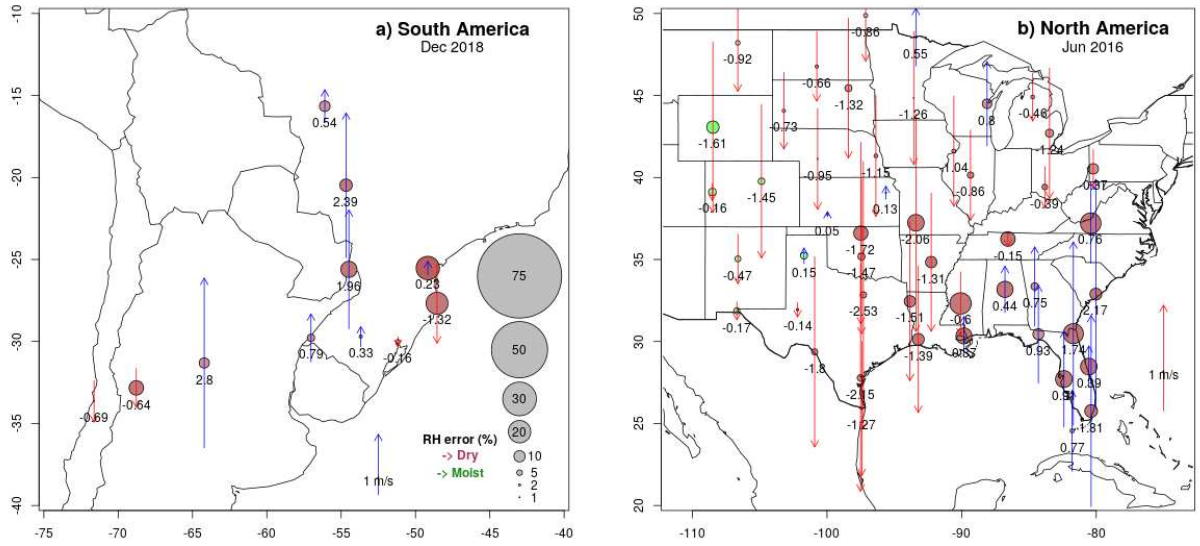

FIG. 2.8. Monthly average 24-hr 700 hPa relative humidity and meridional wind forecast biases in South America (a, December 2018) and North America (b, June 2016) at available sounding locations using the Grell-Freitas cumulus parameterization. Red (green) indicates a dry (wet) RH model bias and size the magnitude. Arrow direction and length indicate the sign and magnitude of meridional wind error; the number at each station gives the actual meridional wind bias rounded to the nearest hundredth m s^{-1}. Color further distinguishes meridional wind bias direction: blue (red) represents positive/northward (negative/southward) model bias. Only locations with multiple 0000 UTC verification times throughout the month are included.

June 2016 in North America was very similar: all locations featured a dry bias east of the elevated terrain (about 100°W), and with the exception of the Southeast US, there was a widespread equatorward meridional wind bias (Fig. 2.8b). Though it cannot be expected for the LLJ to be present at 700 hPa in NA, this meridional wind bias does oppose its direction. The similarities in South and North America biases suggest that error likely occurs due to the same processes, which may not even be LLJ related.

Meridional wind bias can result from an inaccurate forecast of both strength and/or direction; thus, we break down the forecasted and observed meridional wind values that compose the monthly means for two key cities in each continent (Fig. 2.9). In Córdoba (Fig. 2.9a), forecasts were too strong upon observed equatorward wind (opposing SALLJ) and were too weak upon observed poleward wind (with SALLJ). Both of these model errors contribute to the mean of 2.8 m s^{-1} in Figure 2.8a. Alternatively in Mendoza, forecasts missed weak equatorward wind observations and slightly over-forecasted the poleward component (Fig. 2.9b). Both Dallas, TX and Springfield, MO featured equal and opposite

trends as Córdoba, with weak poleward and strong equatorward forecasts (Fig. 2.9c,d), contributing to the -2.53 and -2.06 m s^{-1} errors, respectively. In general, it is clear that under-forecasts of poleward wind speed largely contribute to the overall biases in each continent.

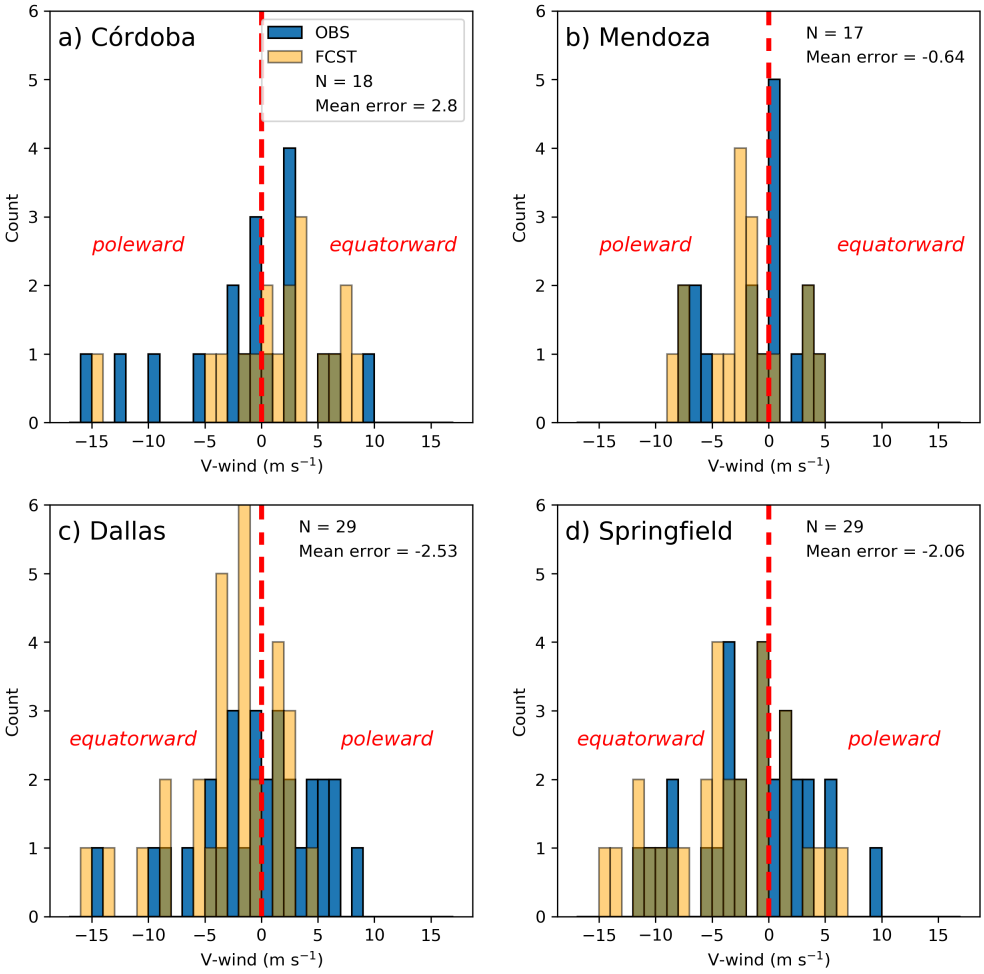

FIG. 2.9. Meridional wind observation (blue) and forecast (yellow) distribution for South American cities (a) Córdoba, AR and (b) Mendoza, AR and North American cities (c) Dallas, TX and (d) Springfield, MO during December 2018 and June 2016, respectively. Positive (negative) meridional wind is northward (southward), indicated by the red text and separated by a red-dashed line at 0 m s^{-1}. The number of observation/forecast pairings, N, in addition to the mean error (m s^{-1}) as shown in FIG. 2.8 is also given for each city.

2.5 SOUTH AND NORTH AMERICAN CASES

As described in *Section 2.1* within the context of previous work, we hypothesized that model error maximizes in association with widespread convection. With this in mind, we identify times of relatively high error and check for the presence of convection, or alternatively, assess the error on days of widespread convection. Daily mean, as opposed to monthly mean 0000 UTC RH RMSE values (as in

Fig. 2.8), not only allows for further comparison between continents, but it also highlights specific instances of error (Fig. 2.10). As previously noted, RMSE in South America tended to be greater, but also varied much more, likely due to the fewer sounding locations considered. 22 December 2018 stands out as a clear maximum, with GF and KF exceeding an average of 40% and 30% error, respectively (Fig. 2.10a). Below we diagnose the error from this day in addition to that of a widespread back-building and upstream propagating MCS case that took place on 11 November 2018. Afterwards we discuss the North America maximum and minimum error days on 17 May and 5 May, respectively (Fig. 2.10b).

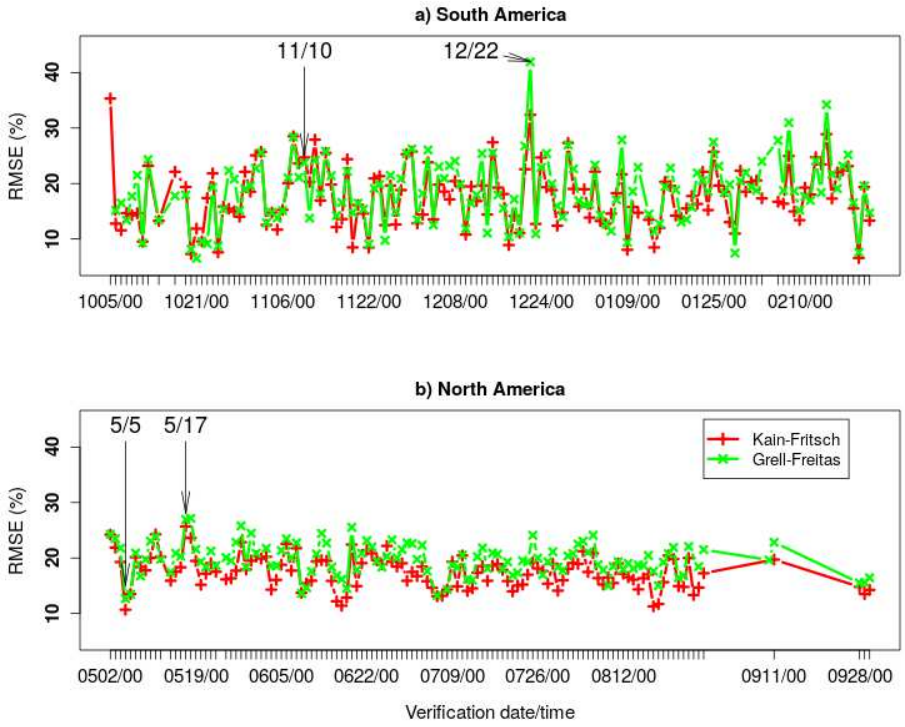

FIG. 2.10. Mean 700 hPa 24-hr RH forecasts in (a) South America and (b) North America. Red (green) indicates Kain-Fritsch (Grell-Freitas).

2.5.1 South America Cases: 22 December & 10-11 November 2018

22 December 2018 featured widespread convection primarily north of 25°S, Argentina, and Uruguay (Fig. 2.11a). On this day, there were some very large positive RH errors in the forecasts in addition to the negative RH errors that were more commonly observed. The largest RH error of +75% occurred at Santa Maria, BR, just south of the convective feature (Fig. 2.11c). This extreme wet bias in the 24-hr GF forecast can be explained by identifying that the model forecast inaccurately predicted this convective band to extend further south and thus rain over Santa Maria (Fig. 2.11b).

There was also a very large discrepancy between forecasted and observed meridional wind at Santa Maria and surrounding locations. The "observed" 48-hr backward parcel trajectories from around Santa Maria, as visualized using GDAS 1° reanalysis and the HYSPLIT model tool, suggest nearly zonal flow approaching the region (blue tracks in Fig. 2.11d). The trajectory ending at Santa Maria actually extends back to the Andes and likely carried dry air as a result (middle blue track in Fig. 2.11d). The model forecast on the other hand had a strong poleward bias of between 2.17 and 5.28 m s^{-1} for locations north of Uruguay (Fig. 2.11c). This poleward direction seems to truly occur farther north where convection actually took place (green tracks in Fig. 2.11d), further alluding to the model misplacement of convection. Figure 2.12 compares the observed and 24-hr GF forecasted soundings from this time and location. While the temperature profiles are similar, the forecasted 600-700 hPa layer is much more moist, featuring a 700 hPa dewpoint temperature of 7.8 °C where -20 °C was observed. It is also interesting that the forecasted low-levels feature moisture and southerly flow as convection occurred to the north, but this is out of the scope of the current study.

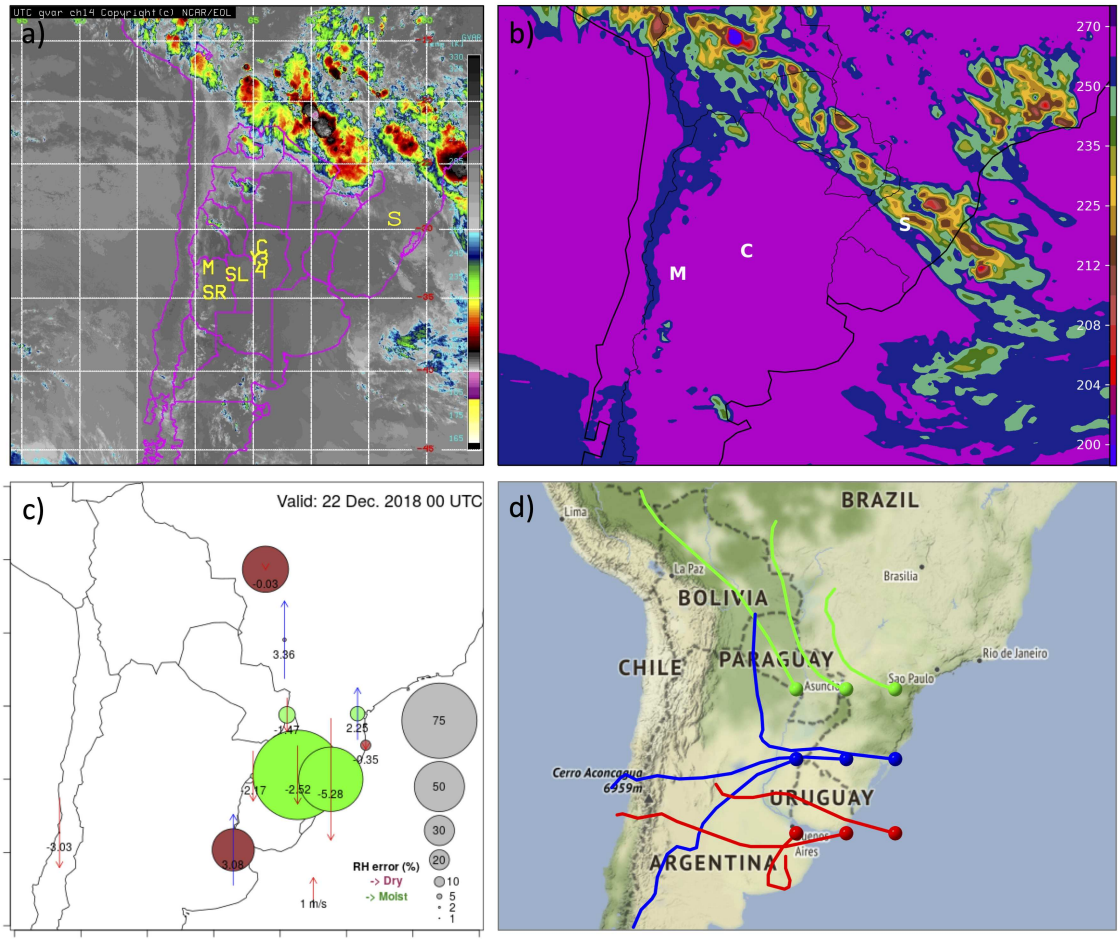

FIG. 2.11. 0000 UTC 22 December 2018 case: observation vs. forecast. (a) GOES-16 IR temperature, (b) WRF simulated IR temperature using GF and 24-hr forecast lead, (c) 700 hPa RH and meridional wind bias as in Figure 2.8b but for the one verification time 0000 UTC 22 December 2018, and (d) GDAS 1° reanalysis 48-hr backward trajectories ending at 0000 UTC via NOAA HYSPLIT model. In the backward trajectories, colors differentiate parcels ending at the same latitude. M, C and S in (a) and (b) indicate locations of Mendoza, Córdoba, and Santa Maria cities.

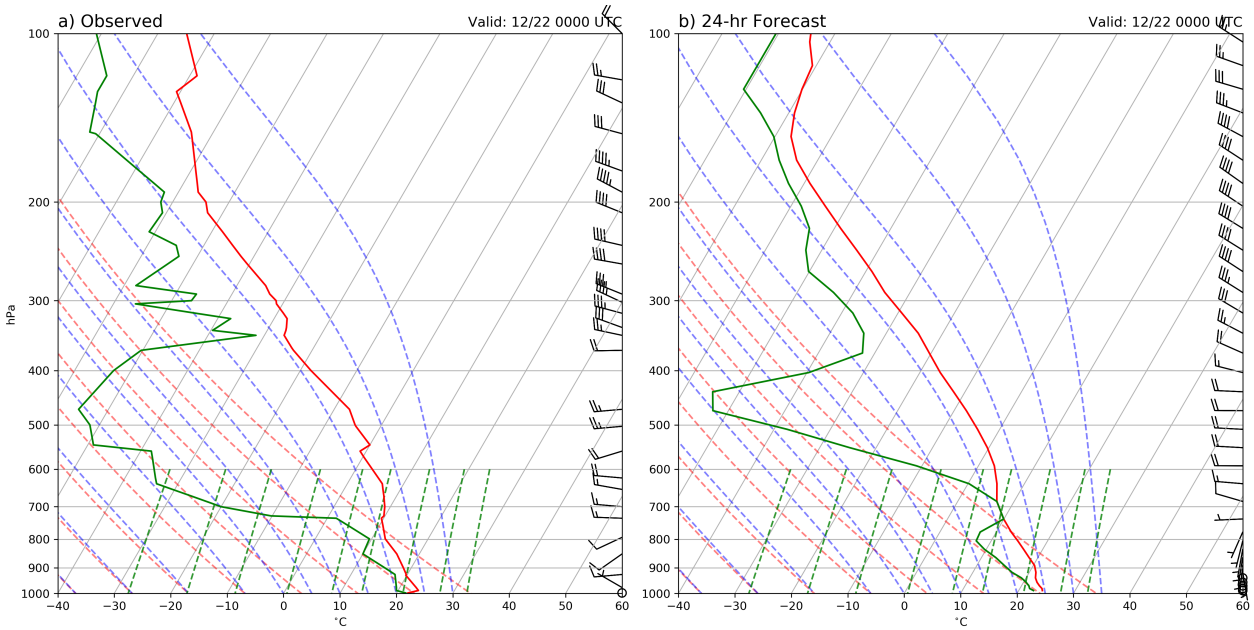

FIG. 2.12. Observed (a) and Grell-Freitas forecasted (b) Santa Maria soundings valid 0000 UTC 22 December 2018. Pressure (hPa) and °C serve as the vertical and horizontal coordinates, respectively. Wind barbs on the right of each Skew-T diagram indicate direction and speed, where a long tick represents 10 m s^{-1} and a short tick 5 m s^{-1}. Temperature (dewpoint temperature) is plotted in red (green). Moist adiabats, dry adiabats, and mixing lines are represented by dashed lines of blue, red, and green, respectively.

While it appears that the main source of both RH and meridional wind error on this day is due to the inaccurate forecast of the convection location, another likely factor is the lack of stations operating in Argentina, namely Córdoba and Mendoza (Fig. 2.11c). This region was clear of any weather and likely would have reduced the mean error if data were available.

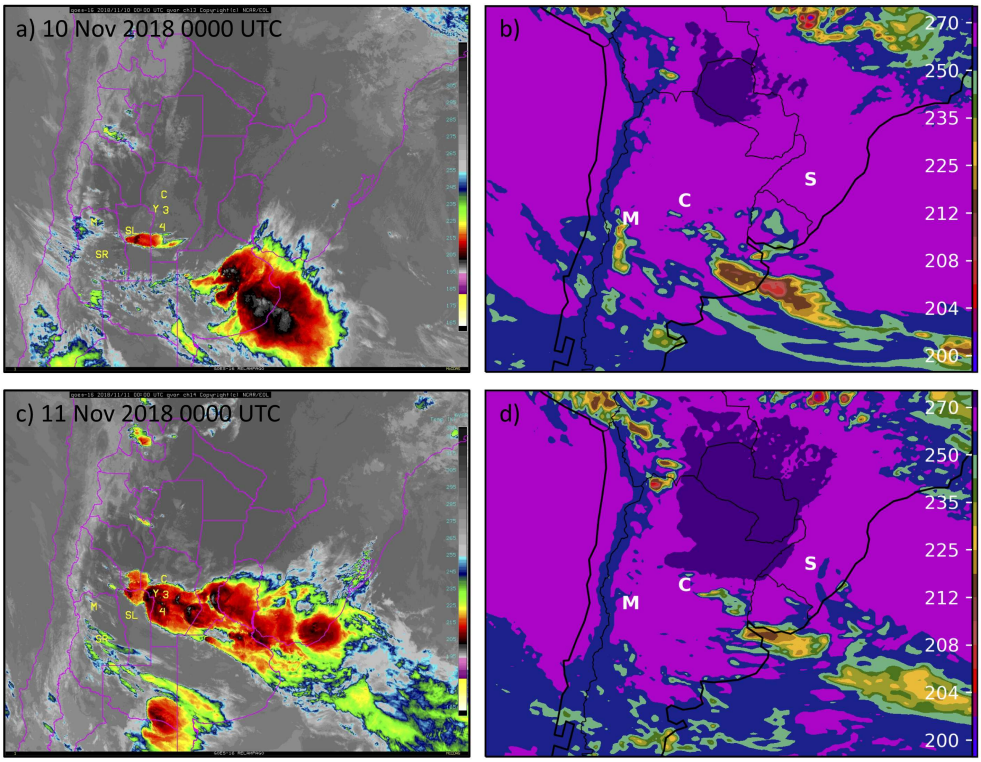

FIG. 2.13. Observed (via GOES-16; left) and forecasted (24-hr lead; WRF with GF; right) IR temperature (K) for 0000 UTC 10 November (a,b) and 0000 UTC 11 November 2018 (c,d). M, C and S on the simulated plots indicate locations of Mendoza, Córdoba, and Santa Maria cities.

One of the more fascinating events during RELAMPAGO initiated around 0000 UTC 10 November 2018 (Fig. 2.13a), featured rapid back-building convection that grew upscale east of the SDC within 24 hours (Fig. 2.13c), and later spawned multiple isolated supercells. As a perfect example of South America convective initiation (Rasmussen and Houze 2016) and upstream propagation (Anabor et al. 2008), this large MCS combined the roles of an extremely deep, slow-moving synoptic trough impinging upon western Chile, lee cyclogenesis, and southward moisture advection along the high terrain (not shown in the current study).

Though the convection during this case was widespread spatially and temporally, the average RMSE at 0000 UTC 10 November was about 25% for both CPs and even smaller on the 11th (Fig. 2.10a). The bulk of this error was in Córdoba and Mendoza, with dry biases around 50% and 30% on the 10th and 11th, respectively (Fig. 2.14a,c). Both locations also featured a strong equatorward meridional wind bias on the 10th, opposing the SALLJ and likely partially explaining the dry bias (Fig. 2.14a). The Córdoba backward trajectory shows northeastward subsidence from the Andes followed by southward flow

likely associated with the SALLJ. Mendoza, located in the immediate foothills of the high terrain, primarily features southeastward subsidence (Fig. 2.14b).

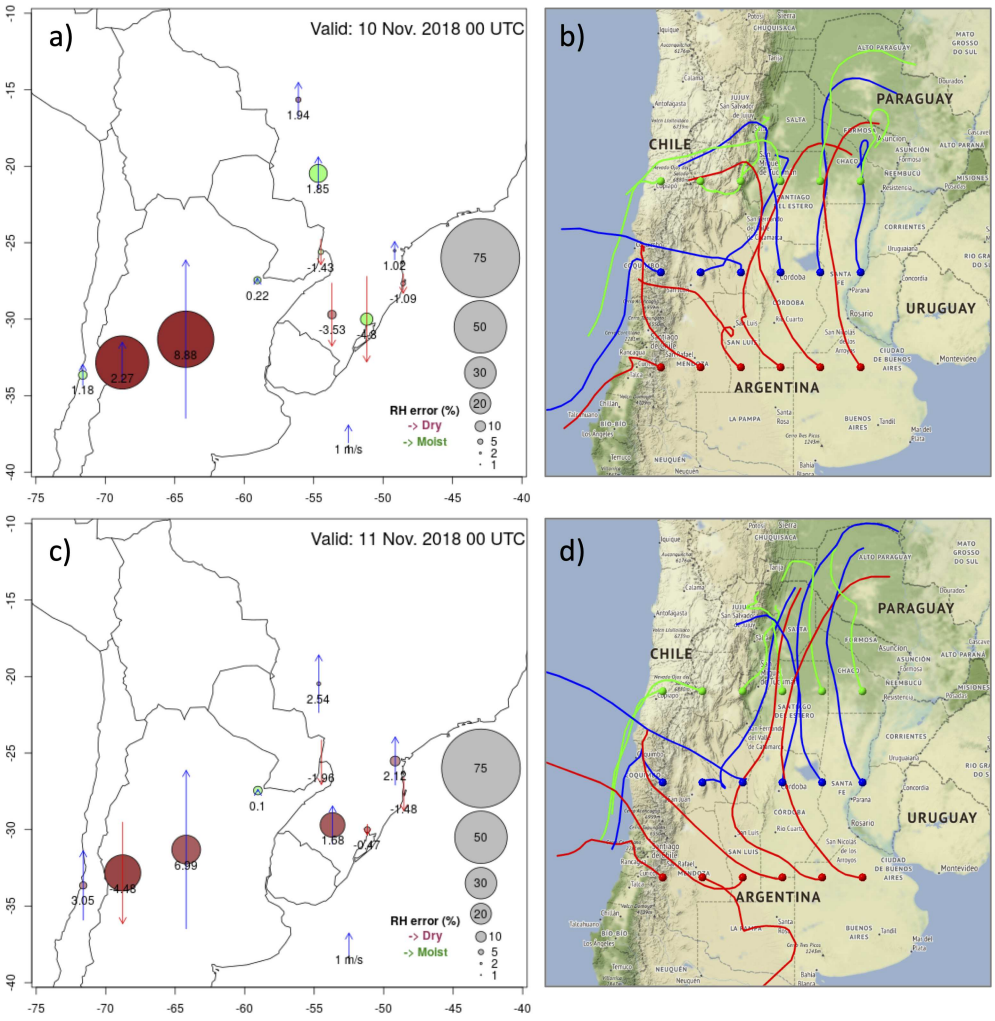

FIG. 2.14. 700 hPa RH and meridional wind 24-hr forecast bias as in Figure 2.11c but for (a)10 and (c) 11 November, and GDAS 1° reanalysis 48-hr backward trajectories ending at 700 hPa at 0000 UTC (b) 10 and (d) 11 November via NOAA HYSPLIT model.

These trends persisted in Córdoba through the 11th while the Mendoza meridional wind bias shifted poleward (Fig. 2.14c) and a northwesterly backward trajectory (Fig. 2.14d). An inaccurate timing of the passage of the low-pressure system within the model likely causes this shift in bias, as the eastward passage of such a system causes a wind shift in Argentina (Rasmussen and Houze 2016).

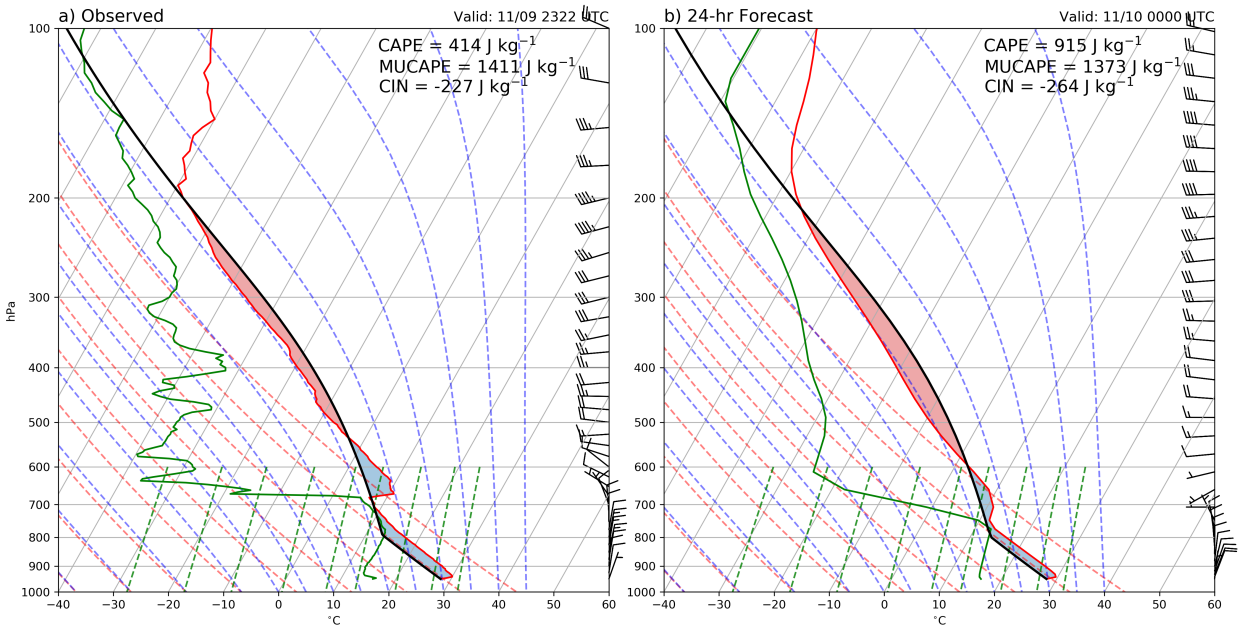

FIG. 2.15. Observed (a) and Grell-Freitas forecasted (b) Córdoba soundings valid 0000 UTC 10 November 2018. Pressure (hPa) and °C serve as the vertical and horizontal coordinates, respectively. Wind barbs on the right of each Skew-T diagram indicate direction and speed, where a long tick represents 10 m s^{-1} and a short tick 5 m s^{-1}. Temperature (dewpoint temperature) is plotted in red (green) and the parcel path in black; areas of CAPE (CIN) are shaded in red (blue). Values of CAPE, MUCAPE, and CIN are shown in the upper-right corner. Moist adiabats, dry adiabats, and mixing lines are represented by dashed lines of blue, red, and green, respectively.

The depth of the SALLJ is evident within the 0000 UTC 10 November Córdoba sounding, as a strong northerly wind component persisted through 700 hPa (Fig. 2.15a). The 24-hr Córdoba forecast on the other hand failed to represent such a depth, extending the northerly component to only about 750 hPa (Fig. 2.15b). The observed and forecasted meridional wind values were approximately -8.1 and 0 m s^{-1}, respectively, leading to the bias shown in Figure 2.14a. The thermodynamic forecast at this level was warm and dry, with temperature and dewpoint temperature at 10.8 and -3.5 °C instead of 8.4 and 7.2 °C, explaining the dry RH bias in Figure 2.14a. While there is much more to compare between the forecasted and observed soundings, such as the differences in CAPE, MUCAPE, and CIN, this is beyond the scope of this study and could be an interesting area for future work.

In summary, the model struggled to accurately represent subsidence from the Andes in addition to the strength of the SALLJ at 700 hPa before and after initiation, both of which seem to contribute to the dry 24-hr forecast bias at 700 hPa. Given that the model forecast did not capture the widespread upscale growth and back-building features of this MCS (Fig. 2.13b,d), the mean error for these days

would likely be even greater had there been more operational soundings to verify against near these features.

2.5.2 North America Cases: 17 May & 5 May 2016

0000 UTC 17 May and 5 May featured the greatest and least average error among North America stations during the 2016 warm season, respectively (Fig. 2.10b). The CONUS NEXRAD radar mosaic on 17 May 2016 reveals discontinuous MCSs across the central US, a convective line through the Great Lakes region, and some convection in LA and FL (Fig. 2.16a). 5 May 2016 on the other hand was rather clear of storm activity in the central US, but featured convection in FL in addition to some stratiform rain associated with a comma-shaped system in the eastern US (Fig. 2.16c). The GF model 24-hr forecast did a reasonable job depicting the location and intensity of these storms on both days (Fig. 2.16b,d).

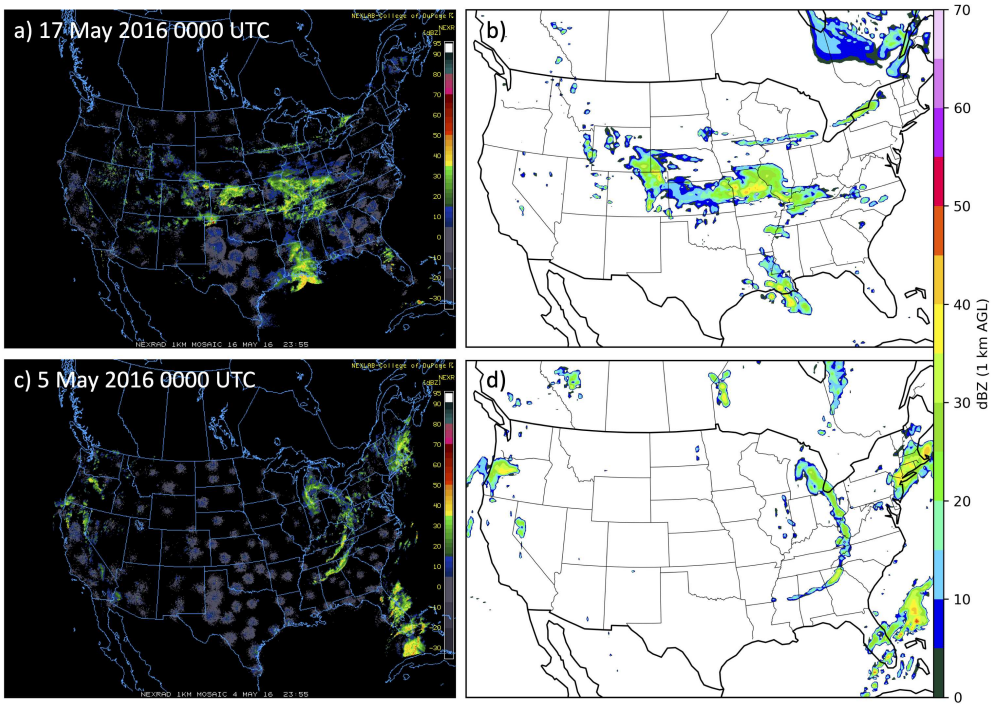

FIG. 2.16. Observed 1 km radar reflectivity (dBZ) via NEXRAD at 0000 UTC (a) 17 May and (c) 5 May versus 24-hr forecasted 1 km radar reflectivity for 0000 UTC (b) 17 May and (d) 5 May 2016.

Robust dry biases greater than or equal to 50% on 17 May occurred near the convection mentioned above, namely KS/OK, WI, and FL (Fig. 2.17a). Various wet biases were also present, some due to model misplacement of storms. Unlike central Argentina, there was mainly a poleward meridional wind bias throughout the central US (Fig. 2.17a). While "observed" backward trajectories within this

region featured a partial northward component, the flow primarily subsided from the high terrain in the west as in South America (Fig. 2.18a).

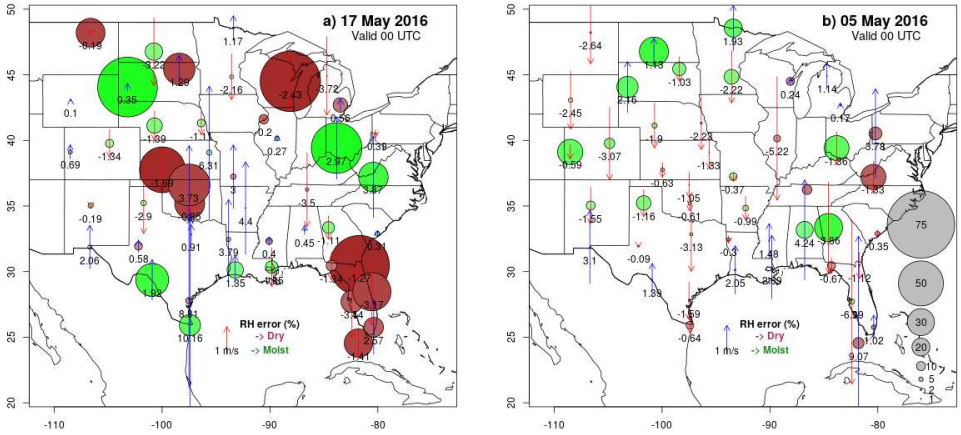

FIG. 2.17. As in Figure 2.14a,c for (a) 17 and (b) 5 May 2016 over North America.

Both RH and meridional wind biases at 700 hPa in the central US on 5 May were substantially smaller (Fig. 2.17b). Additionally, the flow was uniformly southward, avoiding any interaction with the Rockies to the west (Fig. 2.18b), and yielding a relatively straightforward 24-hr forecast.

This comparison between South and North America error days suggests that errors in both continents occur when there is flow from over the western mountainous terrain and large convective systems to the east. Previous work explains this flow by the placement of an upper-level trough over the mountains; EMLs, a capping inversion, and a LLJ along the terrain can occur in tandem as this impinging trough initiates lee cyclogenesis, acting to initiate and strengthen MCS-like systems east of the high terrain (Carlson et al. 1983; Rasmussen and Houze 2011, 2016; Ribeiro and Bosart 2018). Once widespread convection is present, additional error results due to model misplacement of the storms. Above all, these results suggest that thermodynamic model error associated with widespread convection traces all the way back to subsidence flow from the high terrain of the west. Thus, in order to accurately initiate convection over the plains, models must improve their representation of westerly air descending from mountainous terrain.

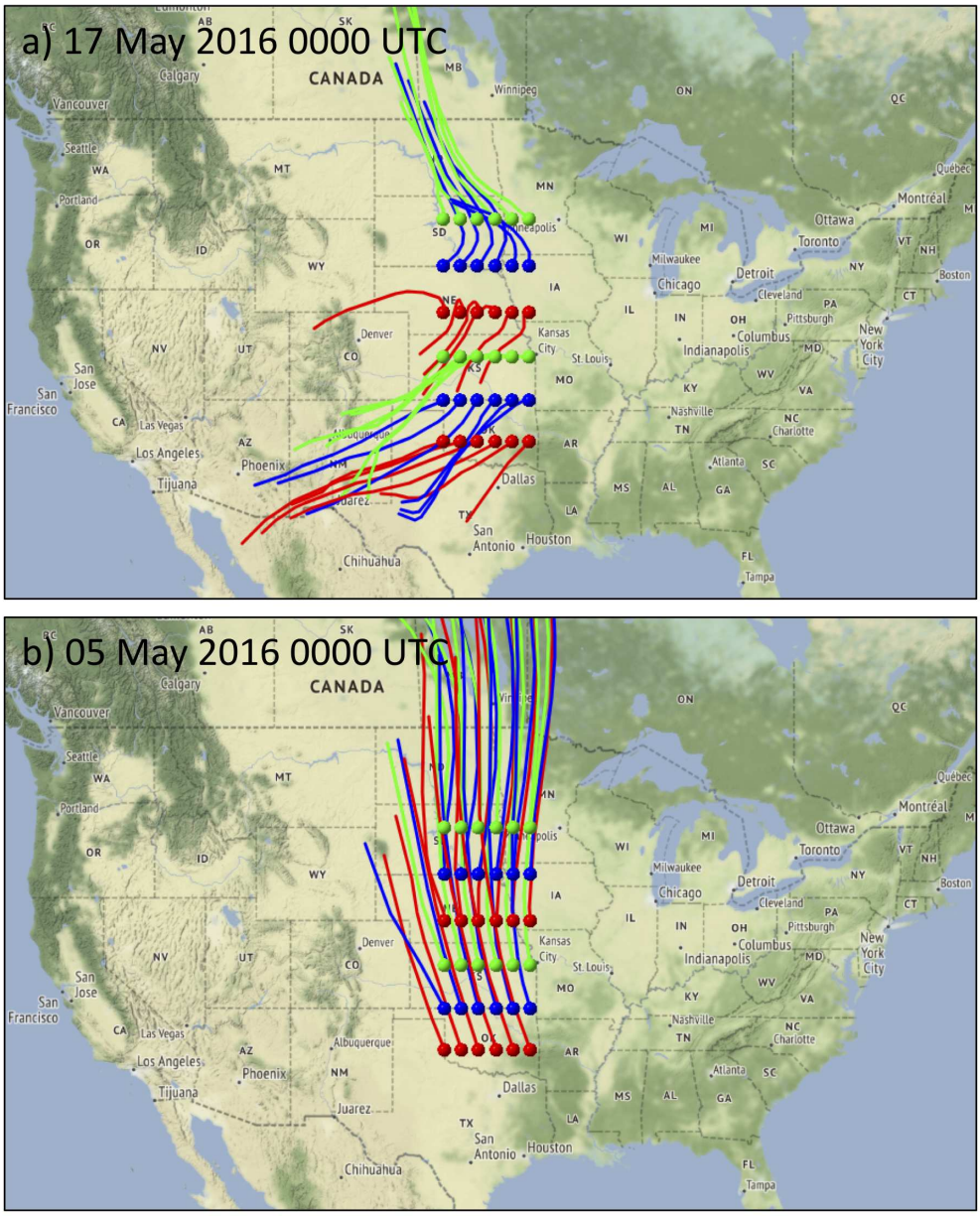

FIG. 2.18. GDAS 1° reanalysis 48-hr backward trajectories ending at 700 hPa on (a) 17 and (b) 5 May 2016 via NOAA HYSPLIT model. Colors indicate latitudes of endpoints.

2.6 SUMMARY AND CONCLUSIONS

In the first part of this study, we verify precipitation forecasts over CONUS of a 19-member 20-km horizontal resolution WRF ensemble against NCEP Stage IV analyses to arrive at three key findings: 1) precipitation forecast skill is greatest during the cool season, 2) skill decreases with increasing precipitation amounts, and 3) ensemble members using the same CP have similar skill throughout the year,

but most notably during the warm season when more convection occurs. Depending on the application, one could sacrifice skill at one time or precipitation threshold to be more accurate at another. This work highlights specific biases among common CPs to guide this sort of decision making within the NWP community.

While previous work suggests that CP also influences precipitation skill in South America using reanalysis data (Blázquez and Nuñez 2009), there is still room for further NWP exploration within this region given the significant impact of extreme rainfall and model error in South America. For example, it would be interesting to compare our North America results to a similar ensemble-based precipitation bias analysis, perhaps employing NASA's Global Precipitation Measurement mission IMERG precipitation data in South America in lieu of Stage IV analyses.

With these results in mind, the second part of this study consists of verifying the forecasted thermodynamic environments against observational sounding networks in North and South America, employing two ensemble members with different CPs. Both continents featured a clear and persistent mid-level dry model bias, particularly at 700 hPa, throughout their respective warm seasons. Large bias occurred in association with westerly flow from the mountainous terrain and large MCS-like systems in the eastern plains. Accurately forecasting flow over mountains in addition to convective initiation and placement of the resulting storms is very challenging, all likely contributing to the error we see in this current study.

Error in South America was consistently greater. The lack of widespread observation stations is a plausible factor in this; fewer points of verification reduces confidence in the mean error and also limits the data assimilation into the model to improve forecasts. There are few to no stations in and west of the Andes Mountains, while there is an abundance within the Rocky Mountains and the western CONUS.

Furthermore, even 20-km resolution models seem to struggle to capture the complex topography of the Andes. The significant height and narrow mountain profile of the Andes allows for a deeper northerly LLJ, often funneled along the high terrain (Insel et al. 2010; Rasmussen and Houze 2016). The Andean foothills and the SDC frequently trigger and terrain-tie convection (Rasmussen and Houze 2011, 2016), which the WRF model forecast inadequately represented for a large, upscale-growing MCS case that occurred during RELAMPAGO. We show that the forecast prior to its convective initiation near the SDC failed to capture the moisture and northerly wind speeds at 700 hPa. With North America cases on the other hand, it appears the mid-level moisture error was solely subsidence flow related.

Thus, it is likely that the model representation of the depth of the SALLJ and the complex topography causes additional errors in South America. Future work could run even finer, convection-permitting resolutions in South America to pinpoint the role of terrain smoothing and parameterized convection in these forecast biases.

Fortunately today it is much more reasonable to forecast weather at convection-permitting resolution and therefore many of the issues we raise here may likely be resolved. However, regional and global climate models usually still rely on CPs, contributing to substantial errors in convective rainfall. Considering the growing importance of understanding convective storms in a future climate, supplemental work should also look into CP bias correction among these larger-scale models, particularly in regard to connecting specific physical processes to model biases. The relation between moisture and precipitation errors could serve as a proper starting point.

Both North and South America are home to some of the deepest convection on the planet, spawning various forms of severe weather that threaten the economic and social welfare of many. As a result, understanding and improving prediction of the thermodynamic environments supporting organized convection is critical for limiting damage today and in a future climate. The impact of large mountain ranges, such as the Rockies and Andes, on weather downstream has been widely studied for decades. However, with the steady advancement of NWP in addition to observational datasets via field campaigns such as RELAMPAGO, we are increasingly able to explain the impacts of terrain and subtle differences in severe weather phenomena between regions of the world. This study in particular suggests that model error comes from similar processes in both North and South America, though certain characteristics of the Andes in contrast with the Rocky Mountains forces models to struggle more. Looking ahead, we hope this work continues the trend of comparing localized severe weather across various regions with similar large-scale environments by taking advantage of advances in technology and global collaboration to obtain ground observations via field campaigns.

CHAPTER 3

A SYNOPTIC EVOLUTION COMPARISON OF THE LARGEST MCSS IN SUBTROPICAL SOUTH AMERICA BETWEEN SPRING AND SUMMER

Subtropical South America (SSA) east of the Andes Mountains is a global hotspot for mesoscale convective systems (MCSs). This study focuses on understanding the synoptic environments supporting wide convective cores (WCCs), which are convective echoes of extreme horizontal dimension, because they are typically embedded within mature MCSs, contribute over 40% of SSA's warm-season rainfall, and are associated with hail, flooding, and tornadoes. Sixteen years of TRMM Precipitation Radar data are used to identify WCCs in SSA and composite environmental conditions associated with the largest and smallest WCCs in austral spring (SON) and summer (DJF). Prior to the occurrence of large WCCs in both seasons, an anomalous mid-level trough impinges upon the Andes from the west, inducing a low-level lee trough and a moisture-rich South American low-level jet (SALLJ) into SSA. Convection initiates near the Sierras de Córdoba (SDC) and grows upscale into WCCs in the presence of low-level convergence, as a result of the lee cyclone's southerly flow interacting with the northerly SALLJ. SON anomalies are greater in magnitude and located farther northeastward. Small WCCs are associated with substantially less synoptic scale forcing, especially in DJF where topography is likely the primary triggering mechanism. These results are corroborated by a large WCC case observed during the RELAMPAGO field campaign (10-13 November 2018), in which convection grew upscale on three consecutive days. Fixed and mobile soundings in tandem with GOES-IR temperature show that strong mid-level vertical wind shear induced by the juxtaposition of the SALLJ and southerly near-surface flow contributes to the organization of elevated MCSs on three consecutive days.

3.1 INTRODUCTION

Thunderstorms maximize in frequency and intensity near large mountain ranges (Zipser et al. 2006); however, ground-based observations are historically sparse in some of these locations around the world. Fortunately, the Tropical Rainfall Measuring Mission (TRMM) precipitation radar (PR) provided a robust dataset of subtropical storm characteristics. Resulting studies using TRMM PR have shown observational evidence that convective echoes east of the Andes Mountains in subtropical South America (SSA) are deeper and more frequent than those east of the Rocky Mountains in North America (Zipser et al. 2006; Houze et al. 2015). Specifically, the cloud shields associated with South American mesoscale convective systems (MCSs) are approximately 60% larger than those occurring in the United

States (Velasco and Fritsch 1987) and their precipitation areas are larger and longer-lived (Durkee et al. 2009; Durkee and Mote 2010), contributing to 95% of warm season rainfall in SSA (Nesbitt et al. 2006; Rasmussen et al. 2016). They are also responsible for the regional maximum in high impact weather such as significant hail (≥2.5 cm diameter), flooding, and tornadoes that are detrimental to society and the economy of the La Plata Basin where agriculture thrives (Rasmussen and Houze 2011; Matsudo and Salio 2011; Cecil and Blankenship 2012; Rasmussen et al. 2014; Bruick et al. 2019).

Prior to the initiation of convection, an enhanced South American low-level jet (SALLJ) guided by the Andes Mountains advects warm and moist air southward from the Amazon basin into the La Plata Basin of northern Argentina (Vera et al. 2006; Insel et al. 2010). A deep mid-level trough simultaneously approaches the mountains from the west, inducing dry mid- to upper-level subsidence flow which creates a strong capping inversion over the moist air mass. This cap is overcome via terrain-induced lift by the Andes foothills and the Sierras de Córdoba (SDC), a secondary mountain range in the La Plata Basin, resulting in vigorous deep convection (Romatschke and Houze 2010; Rasmussen and Houze 2011, 2016). These unique topographic features often act as a platform for "back-building" in which convection continuously initiates and remains tied to the western terrain as storms propagate eastward and grow upscale (Rasmussen and Houze 2011; Rasmussen et al. 2014). Typically in SSA, extremely deep convective echoes form during the evening along the western terrain and grow upscale into extremely wide cores at night as they propagate eastward. Furthermore, because the increased height of the Andes blocks more mid-level flow, enhanced instability and convective inhibition develop downstream relative to shorter mountain ranges (Rasmussen and Houze 2016), providing stronger thermodynamic forcing east of the Andes relative to the Rocky Mountains. These mechanisms of convective initiation in SSA are summarized in a conceptual model by Rasmussen and Houze (2016).

MCS events in SSA can span multiple days, with diurnal resurgences of upscale growth and upstream propagation events (Anabor et al. 2008; Rasmussen and Houze 2016). The long lifetimes seem to be regulated by the slow-moving nature of the mid-level trough approaching the Andes from the west (Rasmussen and Houze 2016), but there has yet to be a direct connection made between persistent instability and trough placement due to lack of high-resolution sounding observations. Similar events have been known to occur in the U.S., though more rarely (Augustine and Howard 1988; Stensrud and Fritsch 1993). After MCSs initiate and organize, where a west-east oriented frontal area or trough meets the southerly low-level jet (LLJ) with strong veering vertical wind shear (Laing and

Fritsch 2000; Coniglio et al. 2010; Peters and Schumacher 2015), positive feedbacks between widespread convection and its significant modification of large-scale flow patterns maintain the organized system (Stensrud 1996). More recently, Chasteen et al. (2019) determine that multiscale phenomena such as LLJ, frontogenesis, cold pools, and terrain interactions contribute to the daytime persistence of a series of nocturnal MCSs in the U.S.

While the large-scale environments supporting organized convection in SSA have been investigated during the austral summer (Rasmussen and Houze 2016), no study has analyzed the synoptic environments associated with organized convection in the austral spring, despite the high impact weather that occurs during this season (Rasmussen et al. 2014). In addition, analysis of the synoptic environments associated with the largest and smallest organized convective systems is presented to find a relationship between the MCS size and magnitude of synoptic-scale forcing and how this changes with season. These results are exemplified through a large organized convective system that occurred over a multi-day period during the 2018 Remote sensing of Electrification, Lightning, And Mesoscale/microscale Processes with Adaptive Ground Observations (RELAMPAGO) field campaign[1]. Fixed and mobile soundings and GOES-16 data made possible from the campaign are used to relate the large-scale conditions to mesoscale phenomena contributing to upscale growth such as vertical wind shear and unique topography; this type of analysis has yet to take place in SSA because of the sparsity of the data prior to the campaign. This work not only improves the understanding of the synoptic environments that lead to large and long-lasting MCSs in Argentina, but also can be applied to other regions around the world that feature widespread or discrete orogenic convection.

3.2 Methodology

Due to the historic the lack of a ground-based radar network in SSA, this study uses 16 years (1998-2013) of V7 TRMM PR data (Iguchi et al. 2000, 2009) to identify storms with extreme characteristics during the austral spring (SON) and summer (DJF). This satellite-borne precipitation radar provided three-dimensional volume scans of reflectivity and rain characteristics with 4-5 km horizontal and 250 m vertical resolution between 37.5°N and 37.5°S during 1997-2014 (Kummerow et al. 1998). We limit our domain to 22°-36°S and 52°-69°W to capture the La Plata Basin and the Andes foothills regions as indicated by Romatschke and Houze (2010) in their Figure 1b (black box in Fig. 3.1). This domain also includes the RELAMPAGO study region which was centered near the Sierras de Córdoba (SDC),

[1] https://sites.google.com/illinois.edu/relampago/home

a smaller, secondary mountain range east of the Andes Mountains. As discussed in Rasmussen and Houze (2016), the height of the Andes in the subtropics is extreme, but decreases poleward (Fig. 3.1).

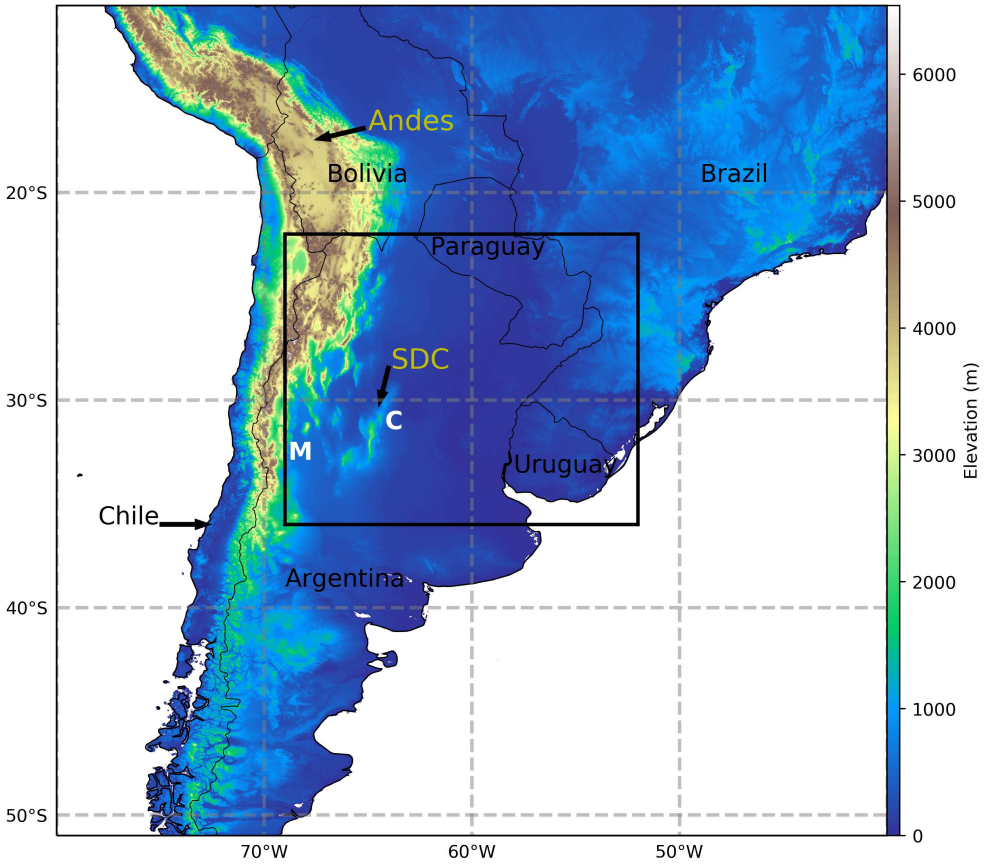

FIG. 3.1. WCC domain used in this study (black box). This region in subtropical South America includes the part of the Andes Mountains, the Sierras de Córdoba (SDC) mountain range, and the cities of Mendoza (M) and Córdoba (C) in Argentina. Color contours represent terrain height. Neighboring nations are also labeled.

TRMM PR is used to identify convective echoes of extreme horizontal or vertical dimension embedded within MCSs. In addition to substantially contributing to the hydrologic cycle (Rasmussen et al. 2016), these echoes imply moments in the MCS life cycle (Houze 2004). Echoes with 40 dBZ heights ≥10 km (deep convective cores; DCCs) indicate young, vigorous convection while those with 40 dBZ areas ≥1000 km^2 when projected onto a horizontal plane (wide convective cores; WCCs) represent more organized convection and often appear among long-lived MCSs that have yet to reach their peak in maturity (Houze 2004; Romatschke and Houze 2010; Rasmussen and Houze 2011, 2016; Zuluaga and Houze 2013; Rasmussen et al. 2016). Because WCCs are much more numerous than DCCs in the La Plata Basin, where they also maximize in size, intensity, and frequency (Romatschke and Houze 2010;

Rasmussen and Houze 2011), they are primarily responsible for the regional maximum in high impact weather and are the focus of the current study.

In order to test the hypothesis that larger and thus more impactful WCCs are supported by enhanced synoptic forcing, WCC echoes, including those featuring a DCC component, are sorted by their size relative to the combined distribution of SON and DJF WCCs during 1998-2013. In particular, the WCCs are divided into two categories: (1) large WCCs as those ≥90th percentile area (4880.165 km^2) and (2) small WCCs ≤10th percentile (1092.679 km^2; Table 3.1). DJF featured 135 more WCCs of any size than SON, but SON WCCs were on average 64 km^2 larger. While the large WCC count was similar between seasons, both the number of small WCCs and unique days on which they occurred was greater in DJF. There were some days in which both small and large WCCs were identified by TRMM; these were counted as large WCC days and excluded for small WCC days in an effort to distinguish the synoptic forcing between the two.

TABLE 3.1. WCC count and size distribution during SON and DJF of 1998-2013 as identified by TRMM PR. Mean and standard deviation (STDEV) of area are shown for all WCCs, regardless of size. The number of large (≥90th percentile) and small (≤10th percentile) WCCs in addition to the number of days of such occurrences is also presented. Small WCC days does not include days that also featured large WCCs..

	# all WCCs	**Mean (km^2)**	**STDEV (km^2)**	**# large WCCs**	**# large WCC days**	**# small WCCs**	**# small WCC days**
SON	1909	2626	2479	195	146	185	112
DJF	2044	2562	2475	201	154	211	147
SONDJF	3953	2576	2477	396	300	396	259

Following the methodology used in (Rasmussen and Houze 2016), a time-lagged depiction of synoptic environments from three days before to two days after the WCC was detected by the TRMM satellite is used to gain an understanding of the evolution of the large-scale forcing for extreme events in the two size categories in SSA. ERA5 reanalysis (Service 2017) is used to create daily synoptic composite maps of meteorological variables for this evolution of WCC environments. ERA5 reanalysis has hourly temporal resolution and quarter degree horizontal resolution that is a significant upgrade from the NCEP-NCAR reanalysis (Kalnay and Coauthors 1996) used in Rasmussen and Houze (2016). Composites are calculated by averaging the conditions on days when WCCs were identified by the TRMM satellite. Composite anomalies result from subtracting the climatological average (1979-2018) of the

corresponding season from the composite field. This format is used to present the synoptic forcing differences between large and small WCCs in SON and DJF.

After the seasonal composite comparison, we test these results against a widespread, long-lived MCS event that occurred during RELAMPAGO on 10-13 November 2018. Here, composite anomalies of meteorological variables are calculated with respect to the November climatological average. In addition to its spatial and temporal extent, this case is unique because it featured back-building convection, serial upstream propagation, and severe weather in the form of hail, tornadoes, and floods. We also combine analyses from high-resolution soundings and GOES-16 IR brightness temperatures available from RELAMPAGO within the context of ERA5 reanalysis to come to various conclusions about synoptic and mesoscale mechanisms supporting this event, including mid-level shear, persistent instability, and upscale growth over the course of multiple days.

3.3 Seasonal variation of WCC synoptic support

To better understand the seasonal differences in synoptic-scale support for widespread organized and severe convection in austral spring and summer, this section presents daily time-lagged composite anomalies both before and after the identification of WCC events by the TRMM PR in the La Plata Basin region (black box in Fig. 3.1) during SON and DJF. However, to place the anomalies into context of the climatology, Figure 3.2 shows the climatological 250-hPa wind speeds over SSA. Both seasons are characterized by enhanced 250-hPa wind speeds over northern Argentina (Fig. 3.2). During SON, the average 250-hPa wind speed maximizes at 30°S as it approaches 40 m s^{-1} over the Andes Mountains (Fig. 3.2a). The northern La Plata Basin is located under the left entrance region of the jet, which in the Southern Hemisphere is a favorable region for divergence aloft and thus large-scale synoptic ascent. In contrast, the DJF wind speed pattern is much weaker at 30°S and maximizes further poleward over the Pacific and Atlantic Oceans (Fig. 3.2b). These climatological differences in jetstream strength and position suggest that there could be stronger synoptic-scale support in SON.

3.3.1 *Synoptic evolution of environments supporting large WCCs*

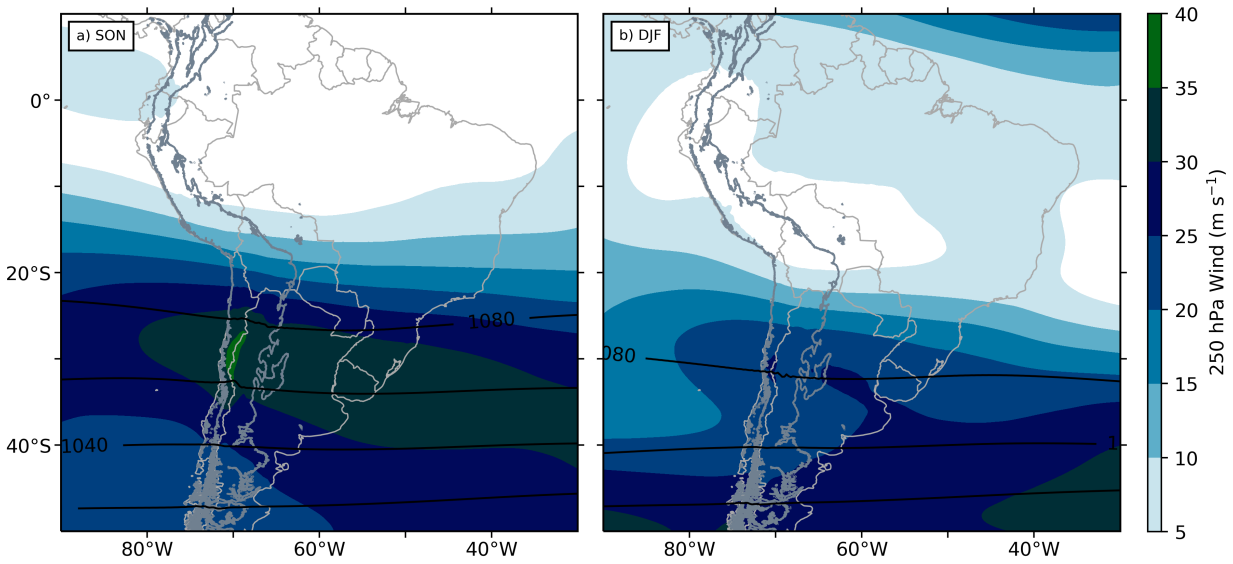

FIG. 3.2. Climatological 250-hPa wind speed (shaded) and height (black contours) averaged from 1979-2018 via ERA5 for SON (a) and DJF (b).

Large WCCs are defined as those with an areal extent greater than or equal to the 90th percentile of all WCCs observed by TRMM PR in the study domain (Fig. 3.1) during SON and DJF from 1998-2013 (Table 3.1). The following time-lagged composite anomaly synoptic maps illustrate the evolution of several meteorological variables that are proxies for large-scale support. These composite anomalies are calculated by subtracting the seasonal climatology (as in Fig. 3.2) from the large WCC composites, which comprise 146 unique days in SON and 154 in DJF (Table 3.1).

Figure 3.3a-c (left) and d-f (right) present 250-hPa wind speed and geopotential height composite anomalies for two days before, the day of, and two days following TRMM detection of a large WCC in SON and DJF, respectively. Two days before WCC identification in both seasons, a 250-hPa wind speed anomaly of about 10 m s^{-1} is present over the Andes just north of 40°S. While the spatial extent of this jet anomaly is greater during SON, 250-hPa heights are anomalously lower east of the southern Andes during DJF where an upper-level trough approaches the continent (Fig. 3.3a,d). On the day of WCC identification, the positive jet and height anomalies have propagated eastward (Fig. 3.3b,e). SON wind speeds have increased at the jet maximum, but decreased to its north (Fig. 3.3b).

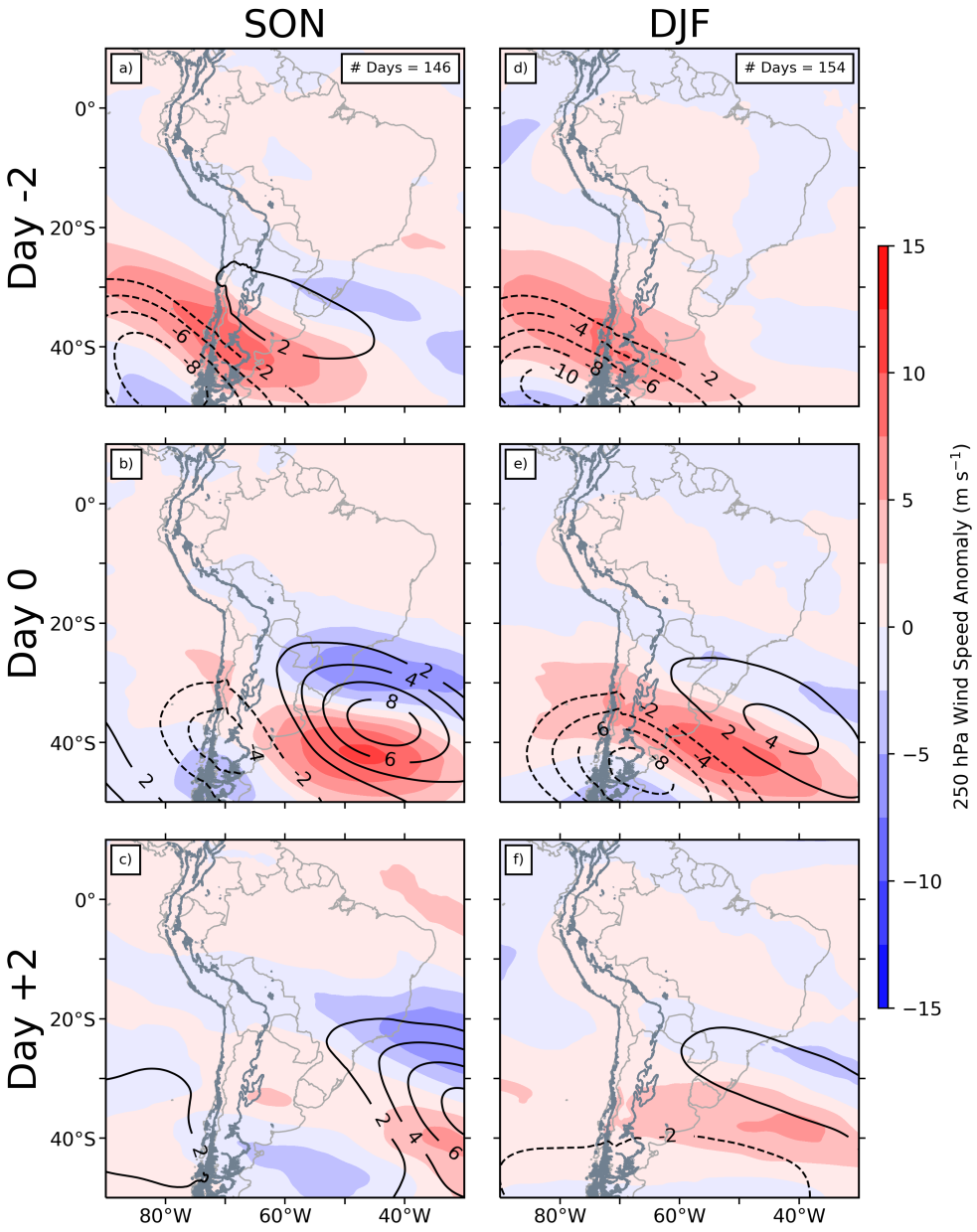

FIG. 3.3. Time-lagged 250-hPa wind speed (shaded) and height (black contours) composite anomalies for days in which TRMM PR identified a large WCC in the study domain during SON (left; a-c) and DJF (right; d-f) on day -2 (top), day 0 (middle) and day +2 (bottom). The gray contour outlines terrain height of 500 m, highlighting the Andes and SDC of western South America. Top panels (a,d) show the number of WCC days that contribute to the composite. These totals are also shown in Table 3.1.

DJF 250-hPa heights remain weaker in magnitude as this deep trough crosses the Andes further to the south than in SON (Fig. 3.3e). The SON jetstreak at this time is further eastward such that its left entrance region over the plains as opposed to the western terrain (Fig. 3.3b). Though an upper-level ridge

builds downstream over the Atlantic during both seasons, the corresponding positive height anomalies are about 40 m greater in SON than in DJF (Fig. 3.3b,e). The wind speed and height anomalies continued eastward two days following the event, though at a slower pace for the less robust DJF anomalies (Fig. 3.3c,f). Both upper-level trough signals virtually vanish, leaving only a trace of a negative height anomaly in DJF. Overall, Figure 3.3 suggests that there are similar jet structures between SON and DJF that create favorable regions for ascent in the La Plata Basin; however, ascent in SON is favored over the eastern plains as opposed to near the western terrain in DJF. An upper-level trough also seems to induce a ridge downstream as it crosses the Andes Mountains. These trough-ridge interactions are diagnosed next via 500- and 850-hPa height anomalies.

To further characterize the large-scale synoptic forcing associated with large WCC events, Figures 3.4 and 3.5 show the daily evolution of 500- (black contours) and 850-hPa (shaded) geopotential height anomalies surrounding such events in SON and DJF, respectively. Three days prior to large WCC identification in SON, substantial negative geopotential height anomalies at both levels, signifying a deep trough, are located west of Chile centered at approximately 45°S (Fig. 3.4a). The 500-hPa geopotential height anomaly minimum exceeded -60 and the 850-hPa exceeded -40 m. Geopotential heights are near average over Argentina at this time, with a weak 850-hPa ridge further downstream over the Atlantic Ocean. The upstream trough intensifies as it starts to impinge upon the Andes two days out (Fig. 3.4b) as the flow is blocked by the substantial barrier. Simultaneously, a low-level lee trough starts to appear over central Argentina through the process of lee cyclogenesis, followed by the ridge downstream. As the synoptic trough crosses the mountainous terrain and weakens (Fig. 3.4c,d) consistent with Davis (1997); Schultz and Doswell III (2000); Rasmussen and Houze (2016), the low-level lee trough continues to intensify, resembling the lee cyclogenesis process that has been observed in this region (Chung 1977; Satyamurty et al. 1990; Gan and Rao 1994; Rasmussen and Houze 2016). By the time the mid-level trough is directly over the Andes near 40°S on Day 0 (Fig. 3.4d), it is weak enough to propagate more rapidly eastward such that the mid-level trough-ridge pattern becomes only slightly out of phase the low-level counterpart (Fig. 3.4e,f).

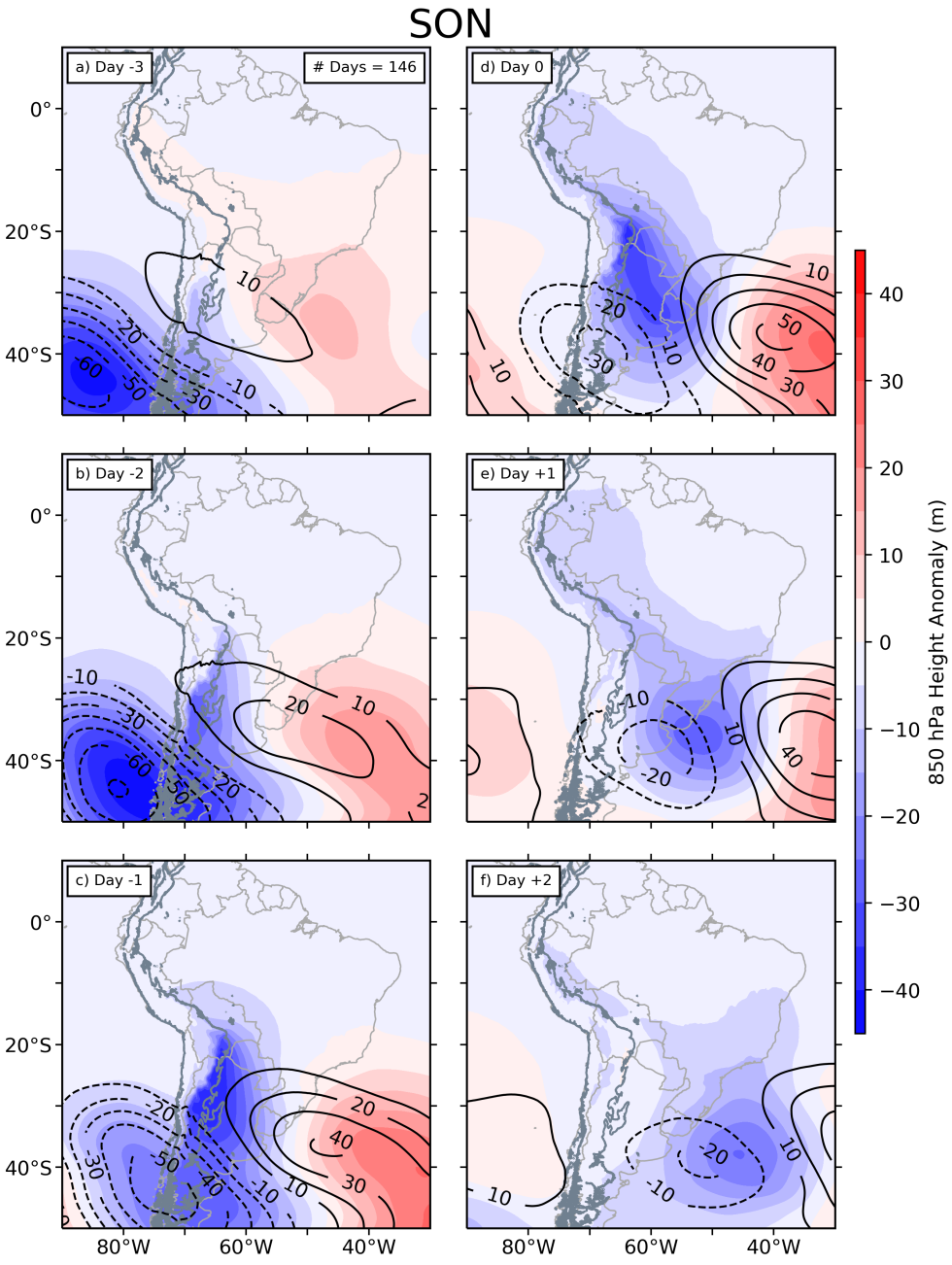

FIG. 3.4. Time-lagged 850-hPa height (shaded) and 500 hPa height (black contours) composite anomalies for days in which TRMM PR identified a large WCC in the study domain during SON on day -3 (a), day -2 (b), day -1 (c), day 0 (d), day +1 (e), and day +2 (f). The gray contour outlines terrain height of 500 m, highlighting the Andes and SDC of western South America. Panel (a) shows the number of WCC days that contribute to the composite. These totals are also shown in Table 3.1.

The DJF 500- and 850-hPa geopotential height anomalies associated with large WCC events (Fig. 3.5) generally follow a similar trend to those of SON (Fig. 3.4) with some differences in intensity and

location. First, the deep trough impinging upon the Andes from the west is weaker and further southeastward initially at both levels (Fig. 3.5a). Its proximity closer to the Andes at Day -3 suggests that the propagation speed was slower initially than SON, consistent with the climatologically weaker jet stream in this season (Fig. 3.2). From Day -2 through Day -1, the impinging trough intensifies at mid-levels such that 500-hPa geopotential height anomalies exceed -70 m (Fig. 3.5b,c) which is larger in magnitude and farther south than SON at this time. It crosses the Andes near 45°S by Day 0, inducing a similar low-level lee trough that is weaker and farther south than that in SON (Fig. 3.5d), which is able to move eastward more rapidly (Fig. 3.5e,f).

While both SON and DJF feature an anomalously deep trough impinging upon the Andes from the west prior to large WCC identification in the La Plata Basin, the SON 850-hPa lee trough is much more robust, which has been shown to induce moisture transport into the region during DJF (Romatschke and Houze 2010; Rasmussen and Houze 2011) through an enhanced north-south pressure gradient force that leads to a stronger SALLJ (Rasmussen and Houze 2016). The lee trough contrast between seasons is likely a result of the poleward shift of the impinging trough from SON to DJF. Because the impinging trough during SON crosses the Andes further equatorward (Figs. 3.4d, 3.5d) where the Andes are substantially taller (Fig. 3.1), more mid-level flow is blocked by terrain. To conserve potential vorticity, additional stretching of an air column via greater downstream descent from high terrain induces enhanced rotation and lee cyclogenesis, resulting in a deeper low-level lee trough (Kasahara 1966; Smith 1984, 1986; Schultz and Doswell III 2000). The key driver of this meridional shift in trough axis with season is radiational heating, which is greatest in the subtropics over the summer, pushing the zone of greatest baroclinic instability poleward in DJF. The result is weaker synoptic forcing over Argentina in summer versus spring. Similarly, Rasmussen and Houze (2016) used terrain modification mesoscale modeling experiments to demonstrate that midlatitude disturbances crossing greater Andes heights lead to stronger synoptic forcing, including a stronger lee trough, and convective instability. The current study also supplements theirs by showing that the DJF synoptic forcing of large WCCs is substantially greater than the forcing for all sizes of WCCs. A similar conclusion for SON is drawn in *Section 3.3.2* where environments supporting small WCCs are analyzed.

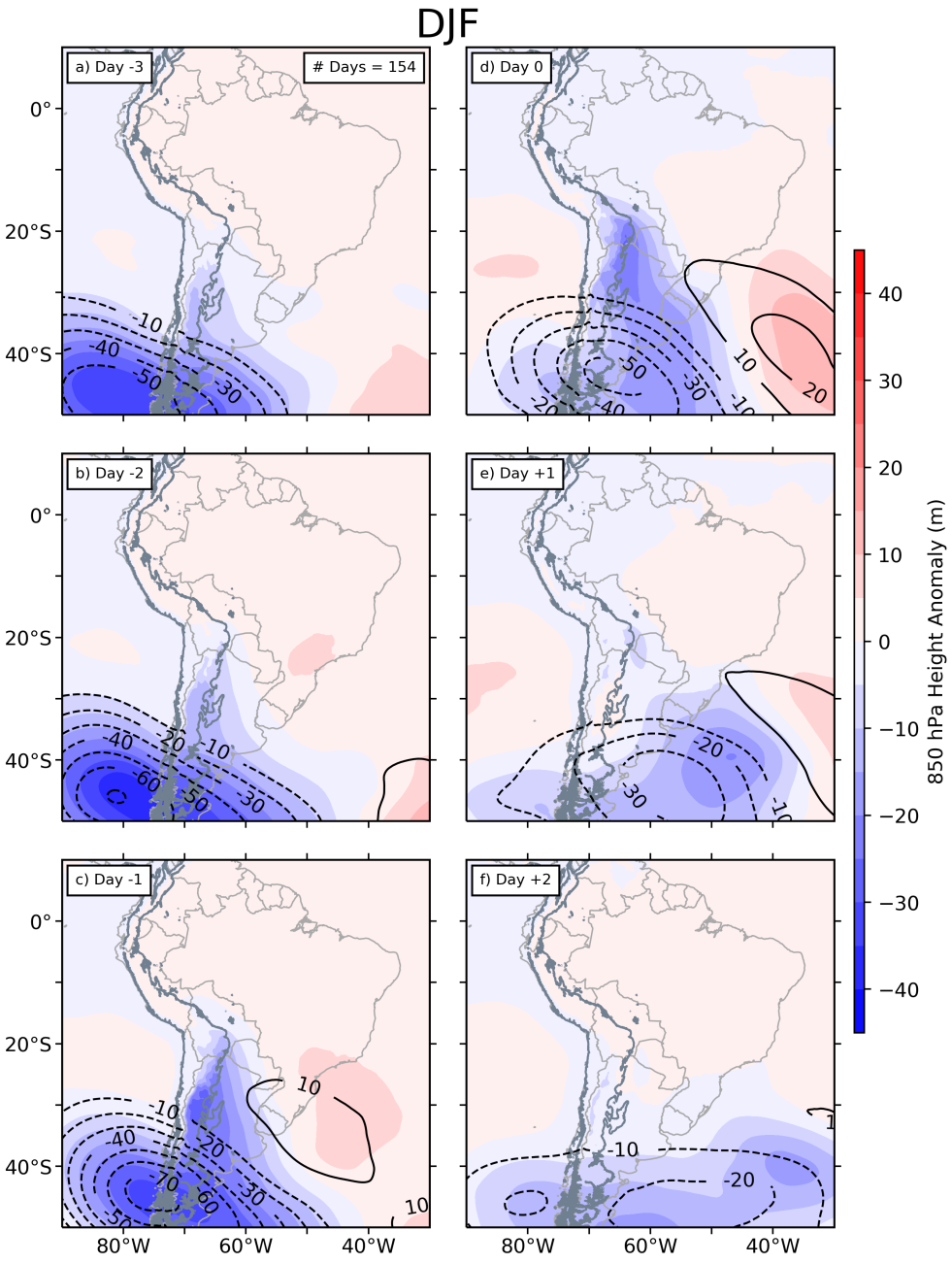

FIG. 3.5. As in FIG 3.4 for DJF.

The SALLJ plays a crucial role in transporting moisture from the Amazon into the region, a key ingredient for convection initiation east of the Andes (Salio et al. 2007; Insel et al. 2010; Romatschke and Houze 2010; Rasmussen and Houze 2011, 2016). Though it can reach depths to 700 hPa, it tends to maximize around 850 hPa (Vera et al. 2006; Oliveira et al. 2018; Piersante et al. 2020). Figures 3.6 and 3.7 present the evolution of 850-hPa wind and integrated water vapor transport composite anomalies,

respectively, where shading represents the meridional anomaly and arrows show the composite vectors in each figure.

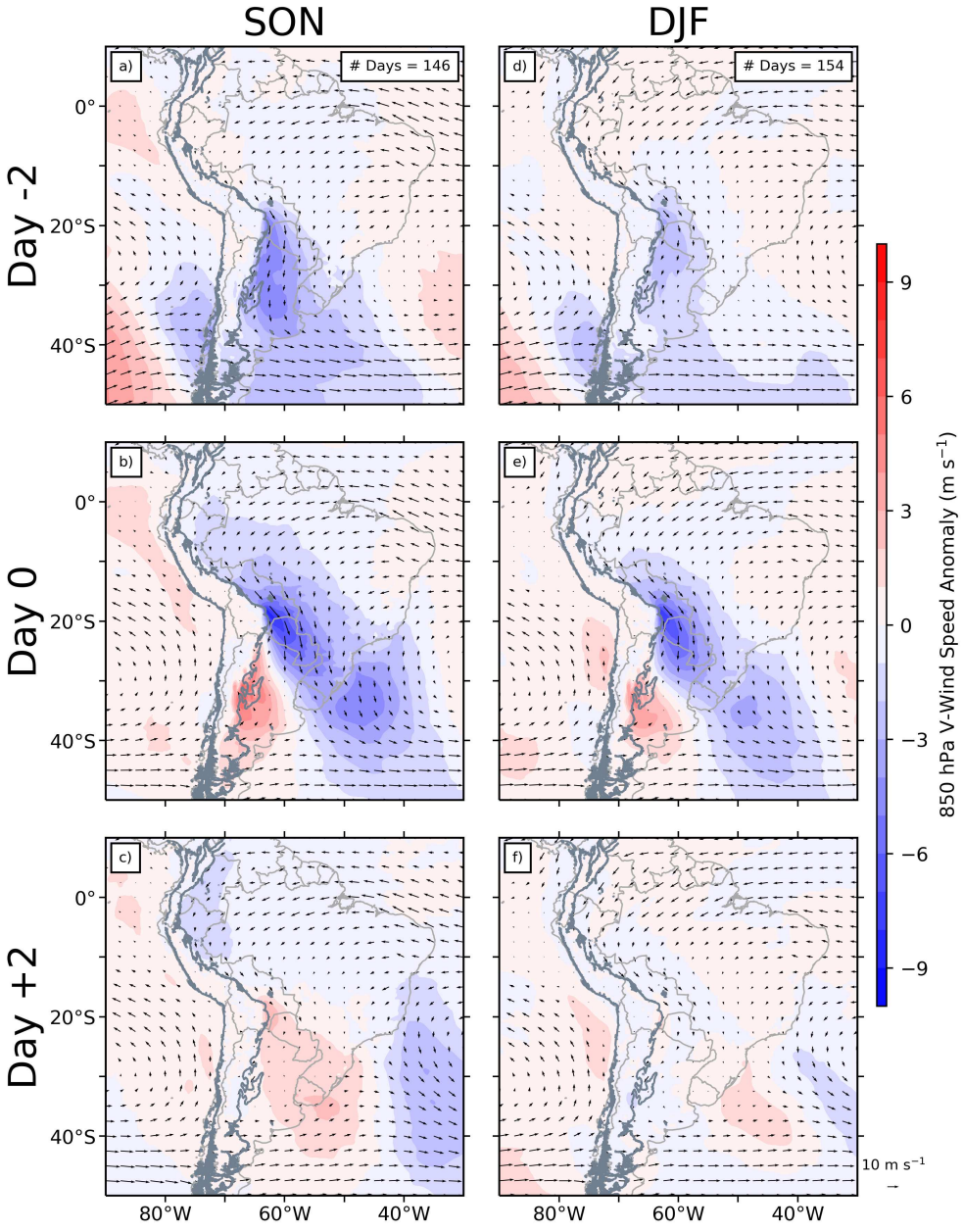

FIG. 3.6. As in FIG 3.3 but for 850-hPa meridional wind speed anomalies (shaded). Arrows represent the composite meridional wind vector, rather than the composite anomaly.

There is widespread northerly 850-hPa wind two days before large WCC events in both SON and DJF (Fig. 3.6a,d) and therefore northerly moisture flux as a result (Fig. 3.7a,d). As expected based on the relative magnitudes of the low-level lee troughs between the spring and summer (Fig. 3.4b, 3.5b), the

wind and moisture flux anomalies in SON are greater. The role the Andes play in channeling moisture is evident as in Insel et al. (2010); Rasmussen and Houze (2016). While the meridional water vapor flux standard anomaly is about 1 sigma near the SDC during both SON and DJF, it exceeds 2 sigma east of the Bolivian Andes as a result of the proximity to the Amazon (not shown).

On Day 0, southerly flow at 850 hPa overcomes central Argentina as the lee cyclone intensifies and propagates eastward while the mid-level synoptic trough moves over the Andes (Figs. 3.4d, 3.5d, 3.6b,e; Rasmussen and Houze 2016). This induces a low-level convergence zone between the two air masses and thus upward motion to aid upscale growth as was shown for MCS case studies in Rasmussen and Houze (2011). While this convergence boundary is centered over the northern SDC in DJF (Fig. 3.6e), it is further northwest in SON (Fig. 3.6b), similar to the meridional placement of the mid-level impinging trough (Figs. 3.4d, 3.5d). The bulk of the northerly wind and moisture flux tapers off near the SDC as the low-level lee trough passes eastward by Day +2, indicating the cease of synoptic forcing in the region (Figs. 3.6c,f, 3.7c,f).

As also shown for all DJF WCCs by Rasmussen and Houze (2016), synoptic troughs induce northerly moisture advection into the La Plata Basin prior to and during the presence of the largest WCCs in SON and DJF (Fig. 3.7). The flux supporting large WCCs appears at least double that of WCCs of all sizes in DJF. Lastly, large WCCs in SON are associated with a slightly greater moisture flux anomaly compared to DJF. However, despite the weaker and western focus in DJF large-scale forcing, the number of large WCCs in both seasons is almost equal. To investigate how essential synoptic support is for any size of WCC during these seasons, we next look at a subset of WCCs with the smallest areal coverage.

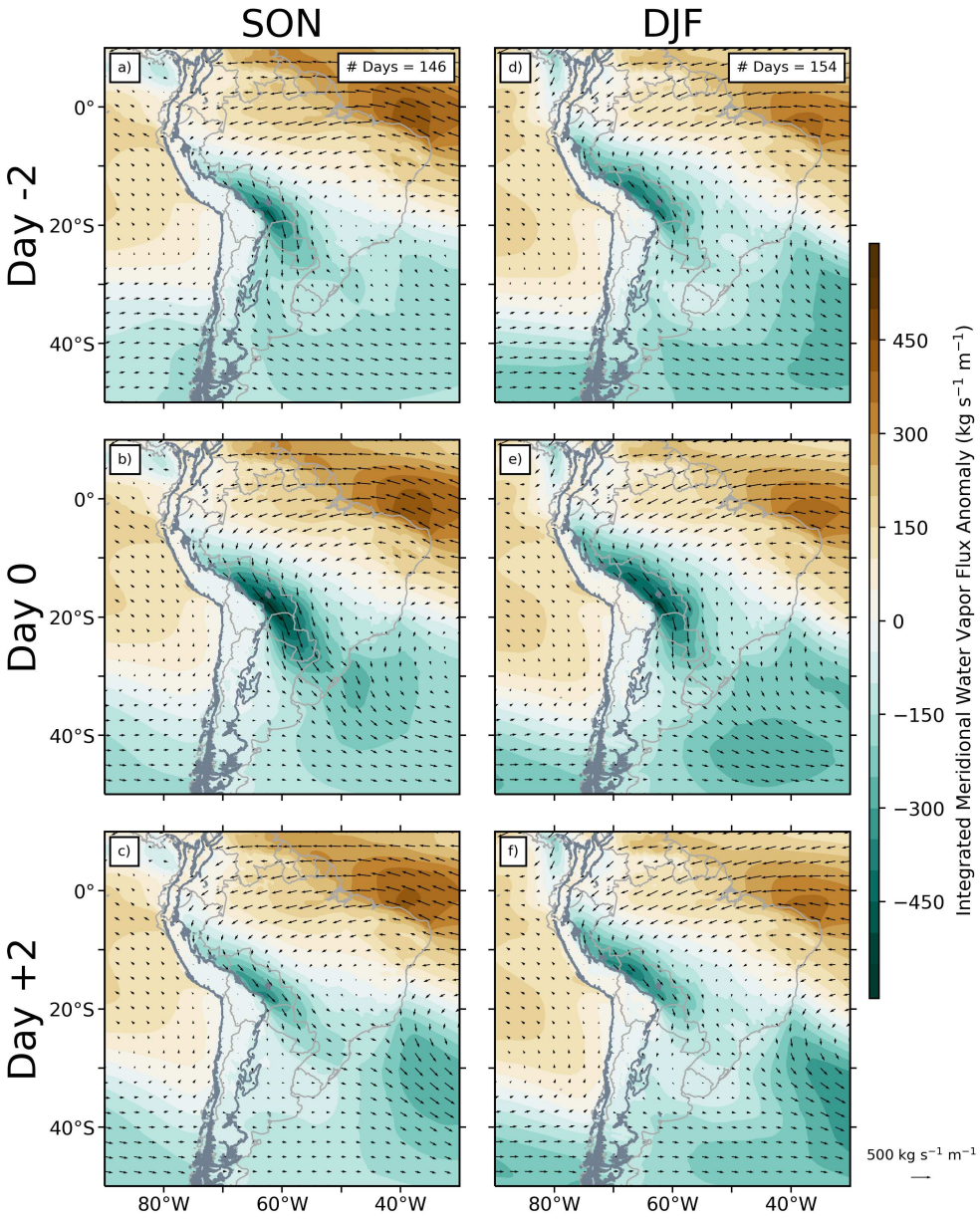

FIG. 3.7. As in FIG 3.3 but for integrated meridional water vapor flux anomaly. Arrows represent the composite meridional water vapor flux vector, rather than the composite anomaly.

3.3.2 Synoptic evolution of environments supporting small WCCs

Small WCCs are those with an areal extent less than or equal to the 10th percentile of all WCCs identified in SON and DJF by the TRMM PR (Table 3.1). While large WCCs are inherently more impactful than small ones because they cover a wider area, this should not dismiss the severe weather impacts small WCCs can have. Small WCC days are just as numerous as large WCC days in DJF (147 vs. 154, respectively) while there are fewer small WCC days in SON (112 vs. 146; Table 3.1). This section examines

the synoptic-scale support associated with small WCCs using a subset of the meteorological variables shown previously.

The 250-hPa wind speed and height anomalies for small WCCs in both seasons is presented in Figure 3.8 as in Figure 3.3. The evolution of 250-hPa SON wind speed and geopotential height anomalies associated with small WCCs is similar to large WCCs; however, the magnitudes are substantially less (Fig. 3.8a-c). For example, the positive wind speed anomaly is about 2.5 m s^{-1} weaker, and the height magnitudes are 20-40 m lower before and during the presence of a WCC (Figs. 3.3a,b, 3.8a,b). Two days following the identification of a WCC in SON, the synoptic setups for small and large WCCs are almost identical (Fig. 3.3c, 3.8c). However, there is a substantial difference between small and large DJF WCC environments. While strong anomalous wind speeds and geopotential heights are clear for large DJF WCCs (Fig. 3.3d-f), synoptic activity at 250 hPa is almost nonexistent for small WCCs suggesting that an upper-level jet is not required for the occurrence of small WCCs during DJF (Fig. 3.8d-f).

The 500- and 850-hPa geopotential height anomaly evolution of small SON WCCs also resembles large WCCs with weaker magnitudes overall such that only a -10 m height anomaly at 500 hPa is over the Andes on Day 0 (Fig. 3.9a-c). The trough-ridge pattern for small DJF WCCs is even weaker but manages to induce a slight low-level lee trough (Fig. 3.9d-f). Though not shown, it can be inferred that the intensities of northerly moisture flux and low-level convergence are generally weaker for small WCCs corresponding to the amount of synoptic support shown in Figures 3.8 and 3.9. Thus, smaller WCCs require less synoptic support compared to large events, but it is striking that small DJF WCCs are not associated with enhanced upper-level winds and only a weak low-level lee trough. Despite this contrast in large-scale support, small WCCs are still more likely to occur in DJF than SON (Table 3.1). Thus, terrain-induced lift by the Andes foothills and the SDC is likely the primary driver of DJF convective initiation, especially for smaller WCCs (Romatschke and Houze 2010; Rasmussen and Houze 2011, 2016). As synoptic waves are known to frequently influence SSA even in the summer (Garreaud and Wallace 1998), the summertime passage of a strong synoptic trough over the Andes is favorable for larger WCCs.

The synoptic composite evolutions presented herein show the large-scale processes that are generally associated with WCCs varying in size and season. However, there are likely additional mesoscale phenomena supporting convective initiation, upscale growth, and back-building within these synoptic environments that require finer spatial and temporal scales to identify and conceptualize. To address

this, *Section 3.4* analyzes a multi-day MCS case that featured WCCs during RELAMPAGO where high-resolution mobile soundings and GOES-16 IR brightness temperature data over SSA were available in addition to ERA5 reanalysis.

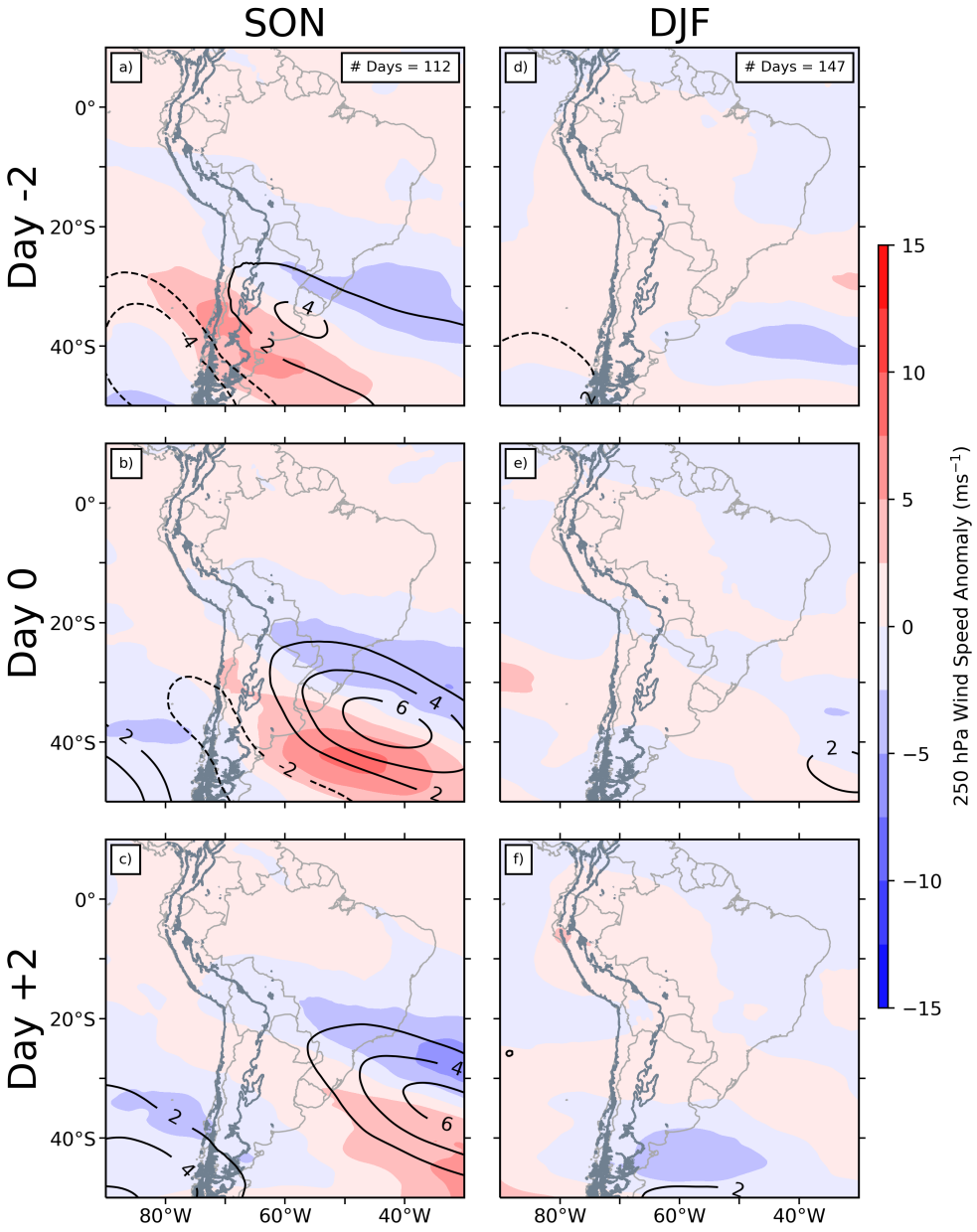

FIG. 3.8. As in FIG 3.3, but for when TRMM PR identified small WCCs in the study domain.

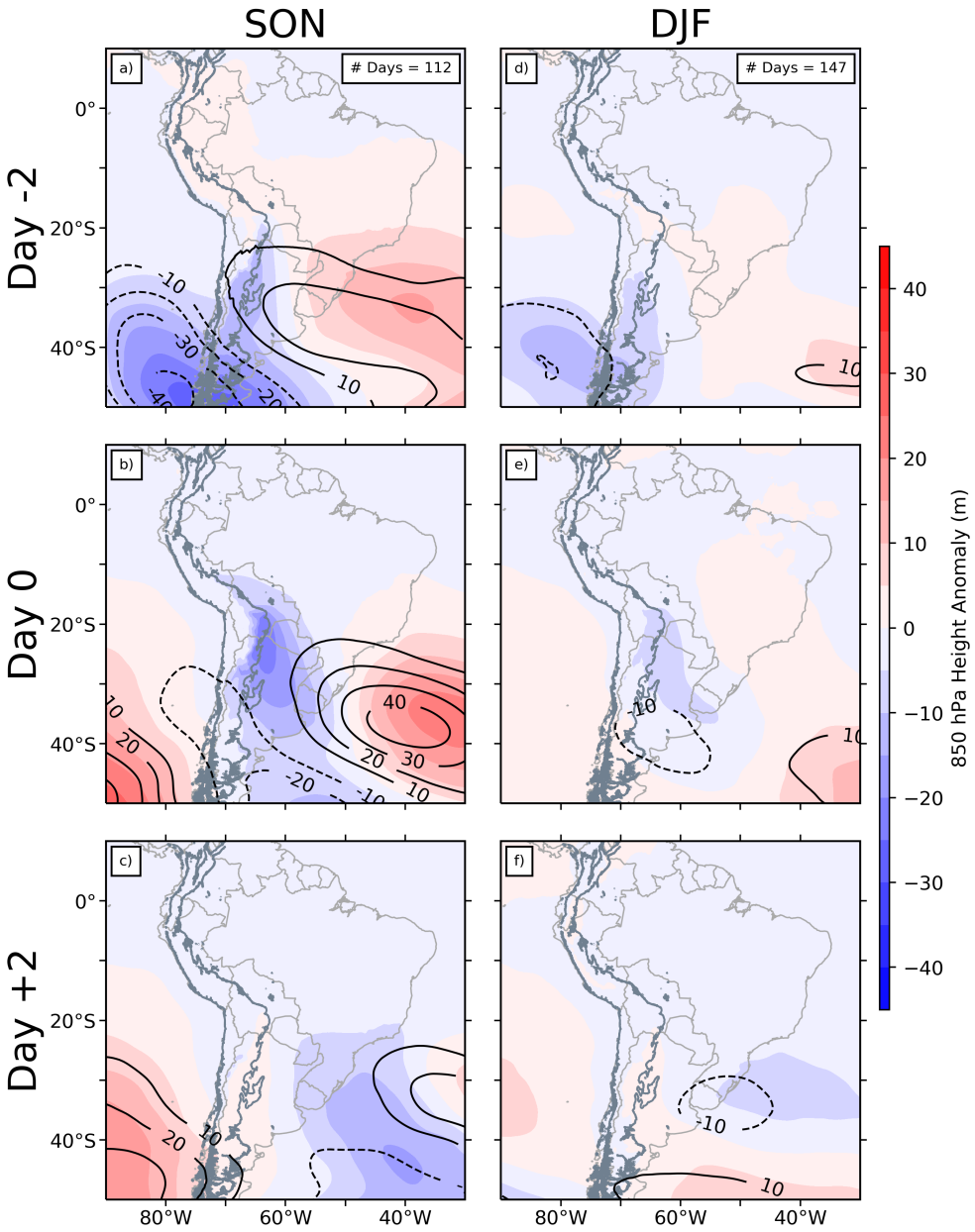

FIG. 3.9. As in FIG 3.3, for 850 hPa (shaded) and 500 hPa (black contours) anomalies where TRMM PR identified a small WCC in the study domain.

3.4 CASE STUDY OF LONG-LIVED LARGE WCC EVENTS ON 10-13 NOVEMBER 2018

The RELAMPAGO field campaign took place in November-December 2018 with primary objectives to observe and collect data from convective storms featuring convective initiation, severe weather, and upscale growth within the vicinity of the SDC. While there were many successful intense observation periods (IOPs), one case in particular met the criteria of all these objectives, including the upscale

growth objectives of capturing back-building and serial upstream propagation. After initiating early on 9 November, elements of deep and organized convection persisted in north-central Argentina through 13 November, including numerous supercells and MCSs. Two IOPs were conducted for this event as a strong jetstreak (Fig. 3.10) and mid-level trough (Fig. 3.11) approached the Andes from the west. Within the framework of these synoptic environments, we highlight key instances of upscale growth via back-building and upstream propagation and identify associated mesoscale phenomena that likely led to these occurrences. Though these processes have been studied extensively in the past as they exemplify the unique ability of storms in this region to frequently persist for hours to days (Stensrud 1996; Anabor et al. 2008, 2009; Romatschke and Houze 2010; Rasmussen and Houze 2011, 2016; Mulholland et al. 2018), the current study provides advances on prior research by utilizing new high-resolution observations from RELAMPAGO such as soundings and GOES IR brightness temperature to connect the synoptic through mesoscale processes in upscale growing MCSs in SSA.

3.4.1 Synoptic environment evolution

Similar to the SON climatology at 250 hPa (Fig. 3.2), a robust upper-level jet streak was present over the Andes and central Argentina during peak convective activity on 11-12 November (Fig. 3.10). This 250-hPa wind speed maximum moved eastward from the west coast on the 10th (Fig. 3.10a), but remained relatively stationary over west-central Argentina on the 11th and 12th as it continued to develop a northerly component (Fig. 3.10b,c). Meanwhile, an anomalous trough-ridge pattern similar to that seen in the composite analysis for large SON WCCs (Fig. 3.4), but much greater in magnitude, slowly propagated eastward as the Andes blocked the extremely deep trough impinging from the west (Fig. 3.11). The movement of this anomalous trough from the Pacific Ocean over South America was slower than the large WCC composite of either season (Figs. 3.4,3.5) as it took an extra day to cross the Andes (Fig. 3.11). The geopotential height minimum crossed the Andes on the 13th at about 32°S, at which point the trough was substantially weakened (Fig. 3.11f), but still much deeper than the seasonal composite anomalies for SON and DJF (Figs. 3.4d,3.5d). The low-level lee trough was present from 9-13 November as a result.

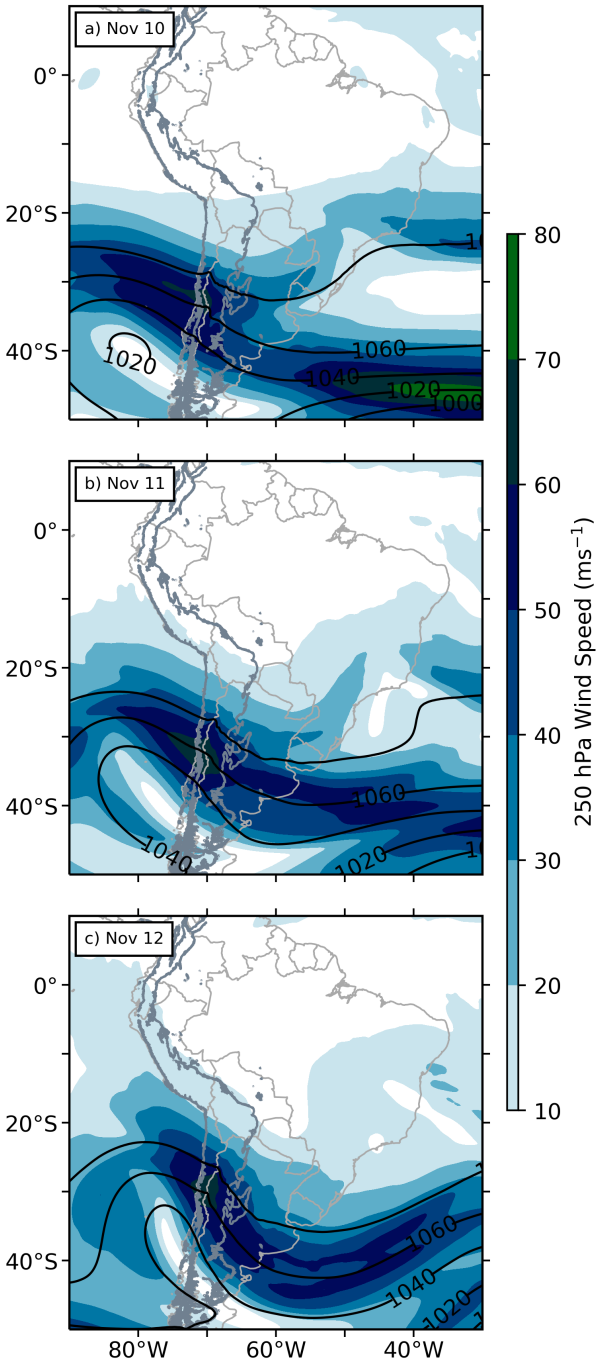

FIG. 3.10. Daily composites of 250-hPa wind speed (shaded) and height (black contours) for November 10 (a), 11 (b), and 12 (c) 2018. The gray contour outlines terrain height of 500 m, highlighting the Andes and SDC of western South America.

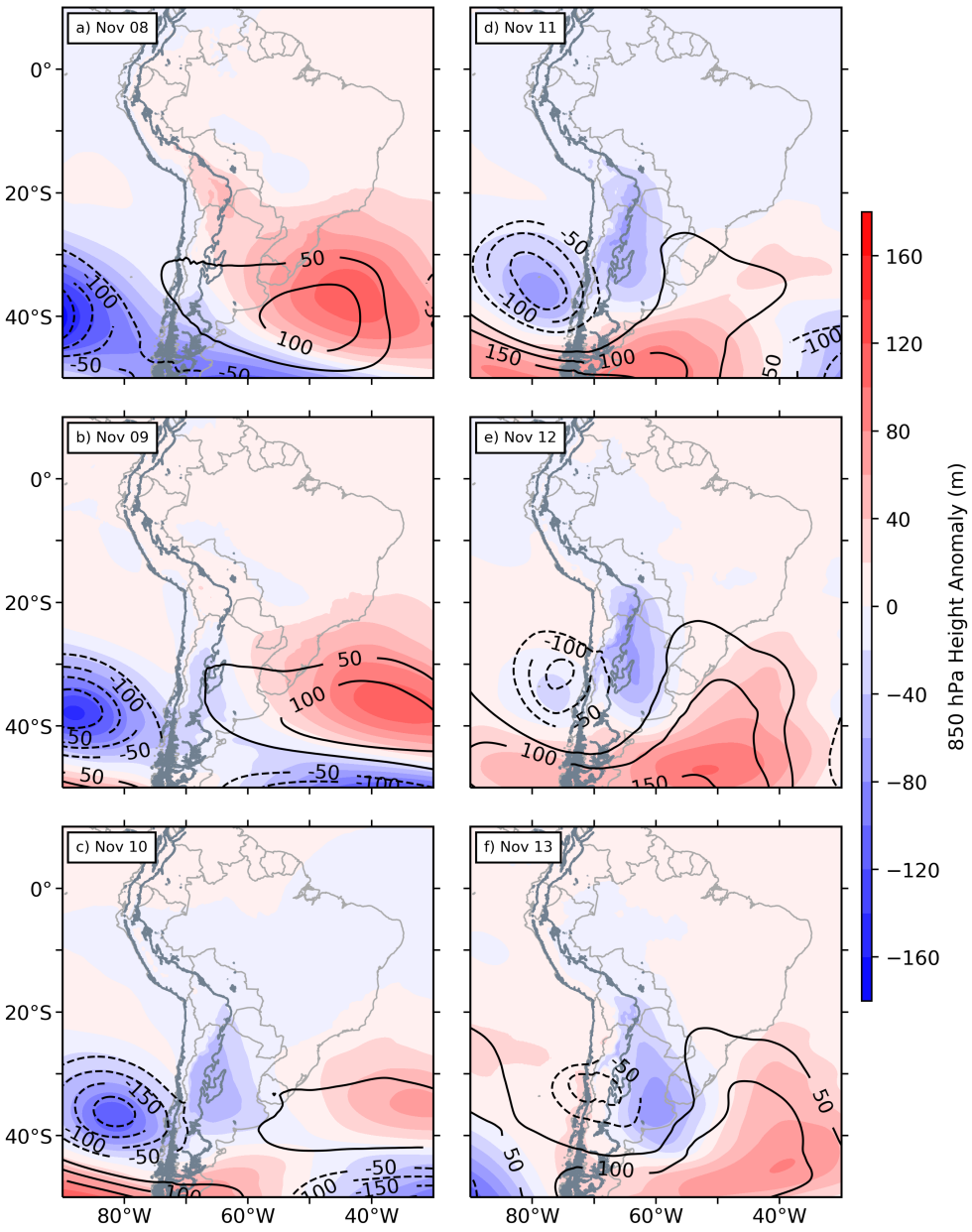

FIG. 3.11. 850-hPa height (shaded) and 500-hPa height (black contours) daily composite anomalies relative to the November 1979-2018 climatology on November 8 (a), 9 (b), 10 (c), 11 (d),12 (e), and 13 (f) 2018. The gray contour outlines terrain height of 500 m, highlighting the Andes and SDC of western South America. Note that the 850 hPa height colorbar has a broader range than in FIGS 3.4 and 3.5.

A strong SALLJ advected moisture southward into the La Plata Basin associated with the long-lasting lee trough (Fig. 3.12). The 850-hPa wind speed and integrated meridional moisture flux anomalies of this case were approximately three times that of the seasonal composite anomalies of large WCCs (Fig. 3.6a-c) owing to the more robust lee trough. The moisture flux maximum also reached

the La Plata Basin (Fig. 3.12f), where it was more than three standard deviations above the mean (not shown), and remained fixed to the Bolivian Andes until it reached the SDC.

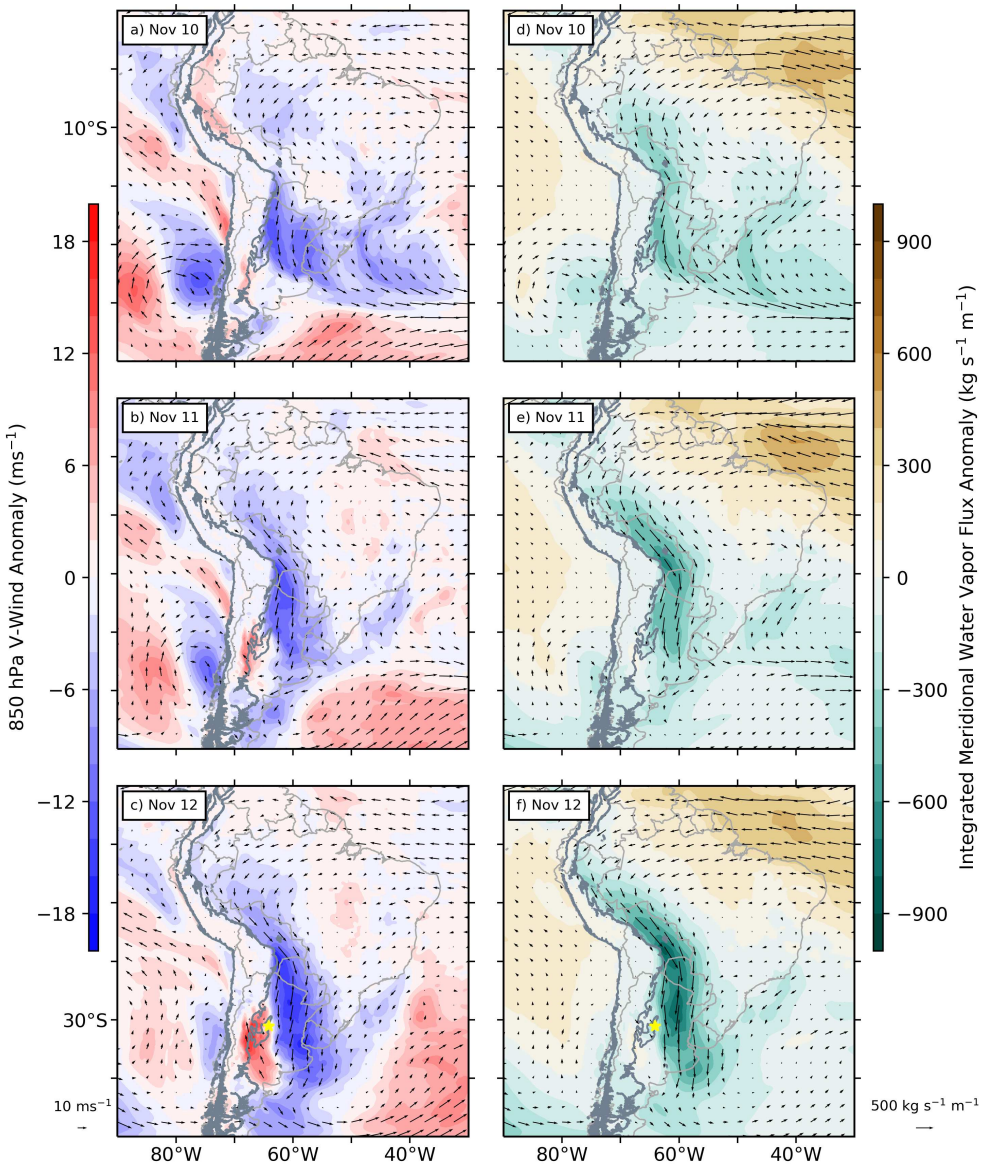

FIG. 3.12. 850-hPa meridional wind (shaded; left; a-c) and integrated meridional water vapor flux (shaded; right; d-f) daily composite anomalies relative to the November 1979-2018 climatology on November 10 (top), 11 (middle), and 12 (bottom) 2018. Arrows represent the composite vector rather than the anomaly. The gray contour outlines terrain height of 500 m, highlighting the Andes and SDC of western South America. The star in (c) and (f) shows the location of Córdoba city. Note that the 850-hPa meridional wind and integrated meridional water vapor flux colorbars have a broader range than in FIGS 3.6 and 3.7, respectively.

This evolution exemplifies the impacts of the robust, quasi-stationary trough off of the coast of Chile; where the seasonal composites feature a more rapid shift toward low-level southerly flow in the

region associated with the more rapid passage of the upper- to low-level trough over the region, this northerly moisture flux lingered for multiple days, allowing for a persistent environment with ingredients favorable for sustained convection. The lee cyclone propagated eastward by 12 November once the mid-level trough started to pass over the Andes (Fig. 3.11e), creating a robust north-south line of convergence east of the SDC such that convection could continue to initiate via low-level convergence in tandem with terrain-induced lift (Fig. 3.12c) that led to rapid and prolonged upscale growth over multiple days. This process was suggested by Rasmussen and Houze (2011, 2016), but RELAMPAGO observations enable a more detailed examination into the mesoscale details of upscale growth as described in the following sections.

3.4.2 Synoptic through mesoscale factors leading to upscale growth

This multi-day event consisted of several long-lived upscale growth episodes that had elements of back-building and serial upstream propagation (Fig. 3.13). Already by 1800 UTC 10 November, a zonal band of cold cloud tops extended eastward from the vicinity of the SDC (Fig. 3.13a). In six hours, the storm grew upscale while building backwards beyond the western terrain of the SDC (Fig. 3.13b). This back-building process that has been described by past studies (Rasmussen and Houze 2011, 2016; Rasmussen et al. 2014) seems to occur in conjunction with the southerly flow west of the SDC associated with the eastward moving lee trough after there has already been adequate moisture supplied to the region (Fig. 3.12a,b).

A second notable upscale growth event occurred when low-level convergence set up east of the terrain (Fig. 3.12c,f). At 0000 UTC, many plumes of convection were triggered along this boundary while storms lingered in eastern Argentina and Uruguay (Fig. 3.13c). Six hours later, convection north of Córdoba grew upscale and organized into a mature MCS as widespread convection to its southeast also intensified (Fig. 3.13d). Convection quickly became organized along the eastern slopes of the SDC as well, showcasing the terrain-locked nature of convective storms associated with this case.

As the low-level lee trough persisted through 12-13 November (Fig. 3.11e,f), convection in northeastern Argentina grew northwestward against the large-scale low-level flow between 1800 UTC 12 and 0000 UTC 13 November to form another mature MCS in northern Argentina (Fig. 3.13e,f). Traces of gravity waves northwest of organized convection can be identified in the IR imagery prior to the upstream propagation (Fig. 3.13e). While Anabor et al. (2008, 2009) attributes serial upstream propagating convection to gravity wave and cold pool interactions, we simply highlight the presence and likely

role gravity waves play with this case. This upscale growth in convection is also likely influenced by the passage of a cold front initiating lift as it cuts northeastward across northern Argentina (Fig. 3.13f).

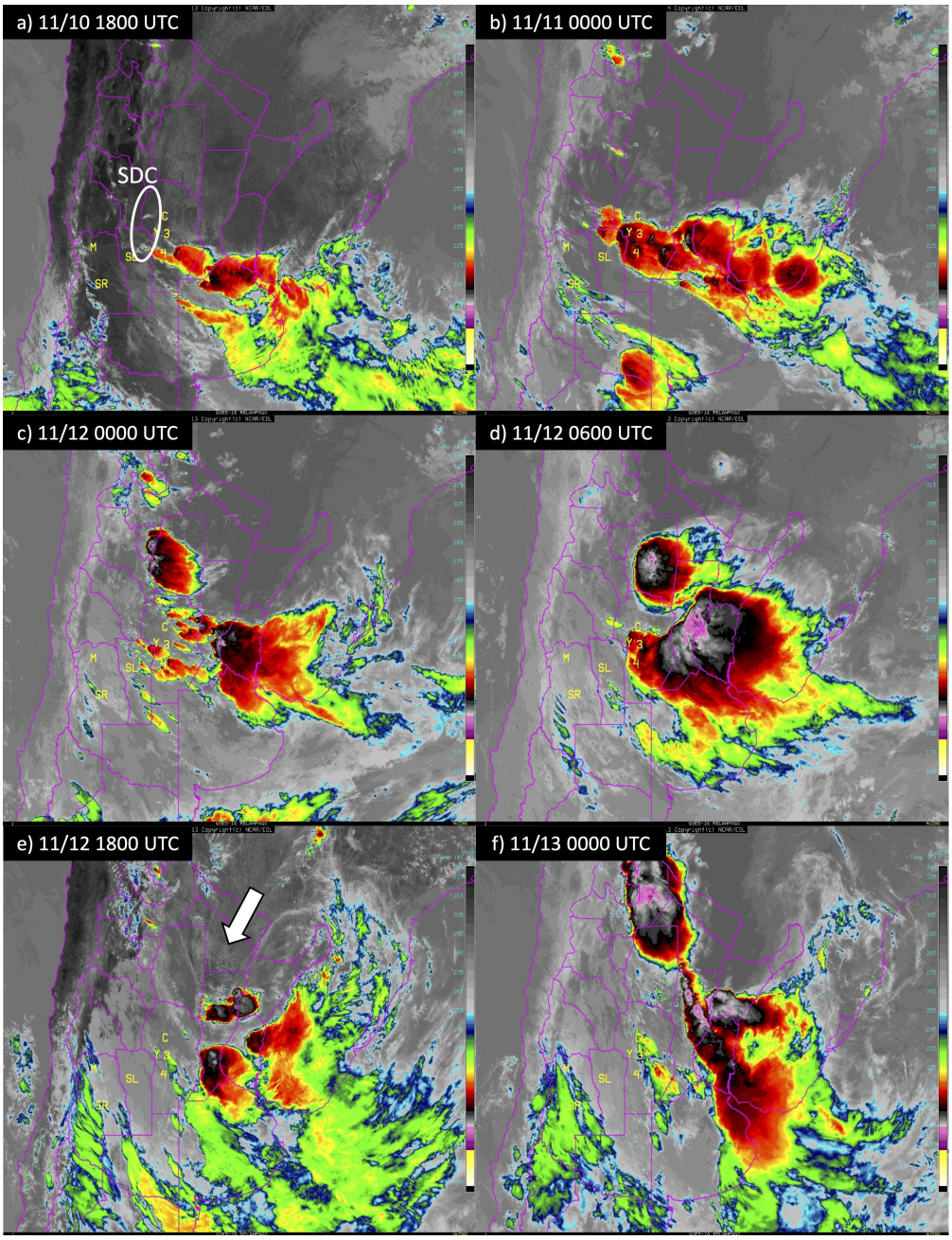

FIG. 3.13. Three six-hour progressions of upscale growth captured by GOES-16 IR temperature during the November 2018 case over the La Plata Basin: 1800 UTC 10 Nov. (a) to 0000 UTC 11 Nov. (b); 0000 UTC 12 Nov. (c) to 0600 UTC 12 Nov. (d); 1800 UTC 12 Nov. (e) to 0000 UTC 13 Nov. (f). M and C indicate the locations of Mendoza and Córdoba cities. The SDC is roughly outlined in (a). Gravity waves are highlighted by a white arrow in (e).

These three episodes of upscale growth are summarized Hovmoller diagram featuring ERA5-derived IR temperature and integrated moisture flux convergence (Fig. 3.14a). Two primary convective episodes initiate around 0000 UTC on 12 and 13 November in addition to a weaker episode on the 11th (Fig. 3.14a), corresponding to the episodes discussed in Figure 3.13. All of which are associated with moisture flux convergence which is a key ingredient for convection in the region (Rasmussen and Houze 2016). The episodes also occur in 24-hr increments with onsets near 0000 UTC (2100 local), marking an evening/nighttime maximum as in Rasmussen and Houze (2011); Rasmussen et al. (2014) and a tie to the diurnal cycle. The outbreak on the 13th that featured upstream propagation was mainly east of the terrain, as its primary trigger was likely the low-level convergence provided by the southerly flow associated with the western edge of the lee trough as it moved eastward over the region in concert with the passage of the mid-level trough over the Andes (Figs. 3.12c, 3.13f). However, lower IR temperatures can be noted at the SDC, as some terrain initiation still occurred separately from the upstream propagation (Figs. 3.13f, 3.14a). The maxima in moisture flux convergence and minima in IR temperature during these episodes align with enhanced 850-hPa northerly wind averaged over the same domain, further highlighting the role of the persistent SALLJ in continued upscale growth (Fig. 3.14b).

The diurnal cycle of organized convection in SSA has been observed using TRMM; typically, DCCs initiate in the evening and grow upscale into WCCs during the evening and night (Rasmussen and Houze 2011; Rasmussen et al. 2014). These peaks in widespread convection (Fig. 3.14a) are tied to nocturnal pulses of the SALLJ (Fig. 3.14b; Vera et al. 2006). Literature has not addressed, however, how this process occurs for multiple days. This knowledge is crucial from a hazardous weather perspective because a nocturnal peak in hail production associated with WCCs in SSA is notably different compared to being associated with discrete supercells in the U.S. (Bruick et al. 2019).

Figures 3.11 and 3.12 suggest that the quasi-stationarity of synoptic waves prolong favorable environments for upscale growth, but to further link the slow movement of the impinging trough to the persistent low-level lee trough and convective initiation, a Hovmoller analysis is presented across a broader longitudinal extent to surround the Andes (Fig. 3.15). During 8-14 November, 500-hPa geopotential heights slowly increased from 5650 m, indicating a weakening trough as it approached the Andes while a ridge built downstream to their east. Around 80°W and 11 November, the trough slowed and 850-hPa geopotential heights and IR temperatures dropped slightly, representing the first convective episode east of the Andes in Figure 3.13a,b and Figure 3.14a. The trough axis was quasi-stationary leading up to 12 November as it started to impinge upon the Andes while average IR temperatures in the

study domain rapidly decreased, indicating the onset of the second convective episode (Figs. 3.13c,d, 3.14a). The trough weakened as it crossed the Andes during 12-13 November and accelerated eastward once the height minimum surpassed 5700 m, inducing a more robust low-level lee trough in addition to widespread low IR temperatures that is the third episode as highlighted by Figures 3.13e,f, and 3.14a.

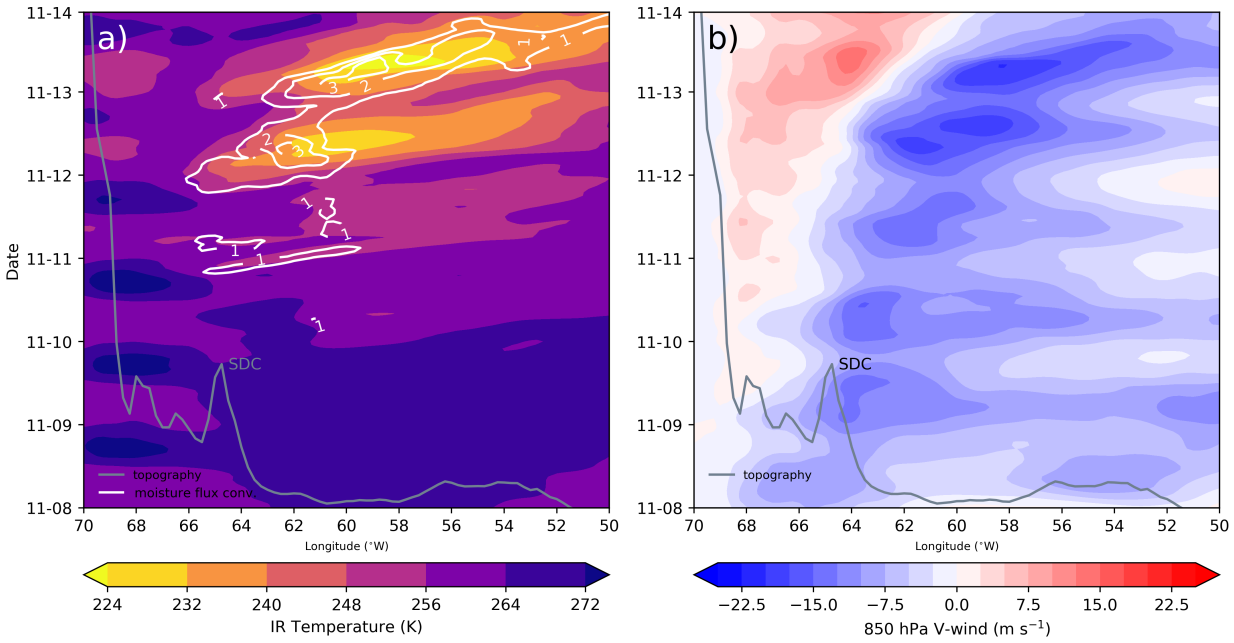

FIG. 3.14. Hovmoller diagrams of ERA5-derived (a) IR temperature (shaded) and vertically integrated moisture flux convergence (white contours; kg^{-2}) and (b) 850-hPa meridional wind speed (shaded) averaged between 22°-36°S for 50°-70°W east of the Andes Mountains during 8-13 November 2018. These arrays were smoothed the SciPy gaussian filter tool using a sigma of 0.85. The gray contour shows the relative topography, with the Andes to the west and the SDC at 65°W, calculated by averaging terrain height between 30°-33°S. Ticks on the y-axis represent 0000 UTC of that day.

The hourly resolution of the synoptic evolution depicted by Figure 3.15, as opposed to the daily resolution of the composite synoptic maps, further connects the relation between the approaching 500-hPa trough and its propagation speed, the low-level lee trough, and the onset of convection in the region initially hypothesized by Rasmussen and Houze (2011, 2016). In the current study, not only is it established that the magnitudes of such phenomena are substantially greater for a multi-day event relative to composites combining even the largest WCC cases, but the propagation of synoptic waves is also much slower. The quasi-stationarity of the trough-ridge system is critical for the continued development and maintenance of organized convection in SSA. The resulting question becomes: why does upscale growth oscillate at diurnal life-cycles and maximize over night?

Because previous work suggests that convection in SSA initiates in unstable environments following the breaking of a strong capping inversion (Rasmussen and Houze 2011, 2016), this question is addressed by analyzing high-resolution stationary and mobile soundings in the vicinity of this case where most unstable convective available potential energy (MUCAPE) and convective inhibition (CIN) are calculated as proxies for instability and capping inversion magnitudes, respectively. MUCAPE is used over CAPE because previous studies suggest that instability is often elevated in the region, especially at night. Hourly atmospheric profile observations such as these provided by RELAMPAGO are historically extremely rare to the region and yield a new opportunity for robust analysis of impactful cases like this.

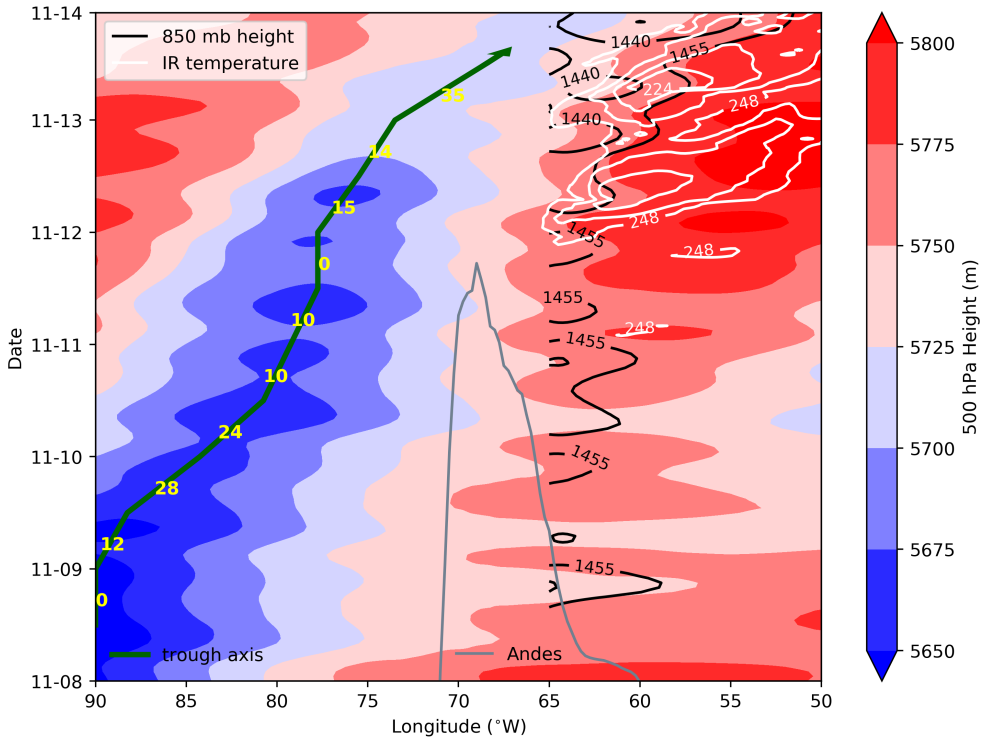

FIG. 3.15. Hovmoller diagram of ERA5-derived 500-hPa height (shaded) for 50°-90°W and 850-hPa height (m; black contours) for 50°-65°W averaged between 15°-50°S during 8-13 November 2018. IR temperatures, averaged between 22°-36°S as in Figure 3.14a, are also shown (white contours). These arrays were smoothed the SciPy gaussian filter tool using a sigma of 0.85. The gray contour shows the position of the Andes Mountains. The green arrow indicates the trough axis, with 12-hr averaged propagation speeds (km hr^{-1}) in yellow, computed assuming that 85 km separates 1° of longitude, which is true at 40°N/S (Williams 2018). Ticks on the y-axis represent 0000 UTC of that day.

Generally, MUCAPE and CIN values at the Córdoba airport (star in Fig. 3.12e,f) were very large throughout the event (Fig. 3.16). MUCAPE featured two maxima of 3520 and 3370 J kg^{-1} at 1603 UTC 10 November and 2021 UTC 11 November, respectively, which was just a few hours before the first

two convective episodes over the region; most other launches around this time exceeded 1000 J kg^{-1} (Fig. 3.16). CIN reached extreme values of almost 400 J kg^{-1} multiple times during 10-12 November, also aligning with the hours before a major convective outbreak (Fig. 3.16). There was a consistent reduction in CIN to 0 J kg^{-1} between episodes, indicating the generation of a new capping inversion on back-to-back days. To further investigate the changes of MUCAPE and CIN with respect to the synoptic evolution, we analyze three soundings in detail that were launched before, during, and after the southerly low-level flow shown in Figure 3.12. These instances are marked by red in Figure 3.16 and the full soundings are shown in Figure 3.17, where the black line traces the most unstable parcel path and thus the red shading indicates MUCAPE.

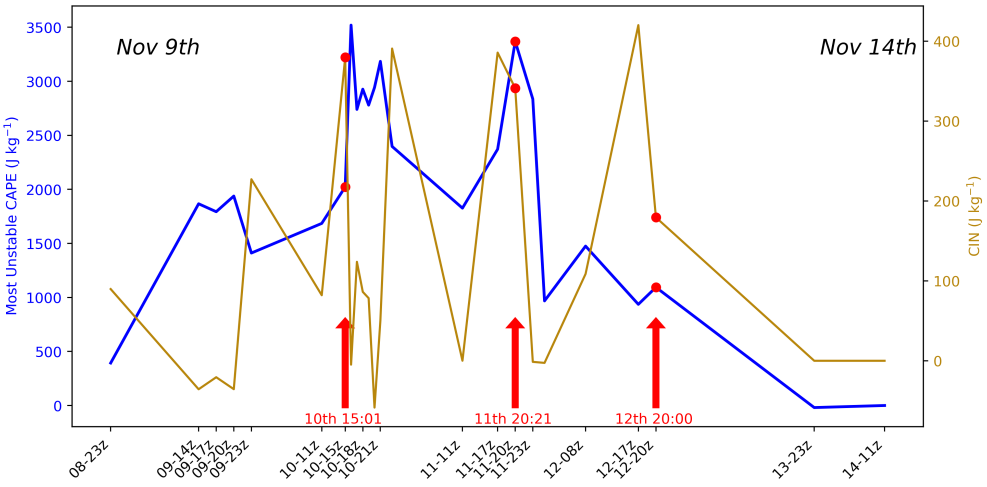

FIG. 3.16. MUCAPE (blue) and CIN (yellow) values from all available Córdoba City Airport sounding launches between 2300 UTC 8 November through 1100 UTC 14 November 2018. Red arrows, points, and text indicate three soundings and their corresponding MUCAPE/CIN values and launch times that are plotted in Figure 3.17.

Before the southerly flow started, the 1501 UTC 10 November sounding indicates a strong capping inversion, with a CIN value of -380 J kg^{-1} and a moderately dry boundary layer with elevated instability. Low-level winds were northerly, but shifted westerly with height as dry air descended from the Andes, likely contributing to this cap (Fig. 3.17a). At 2021 UTC the next day, low-level winds started to turn southerly, while an elevated SALLJ centered near 700 hPa induced northerly moisture advection; this is indicative of the onset of southerly flow at low levels and a sudden increase in mid-level vertical wind shear that is favorable for mesoscale organization and upscale growth (Fig. 3.17b; Laing and Fritsch 2000; Coniglio et al. 2006, 2010). MUCAPE increased to 3370 J kg^{-1} and the strong cap was maintained. Vertical wind shear was enhanced as southerly flow increased and the elevated SALLJ persisted into

2000 UTC 12 November (Fig. 3.17c). Despite a reduction in MUCAPE and CIN, storms soon matured over Córdoba and northern Argentina that organized into the third episode of upscale growth during this period (Fig. 3.17f). In general, this sounding analysis shows that convection organizes in strongly sheared environments following maxima in MUCAPE and CIN.

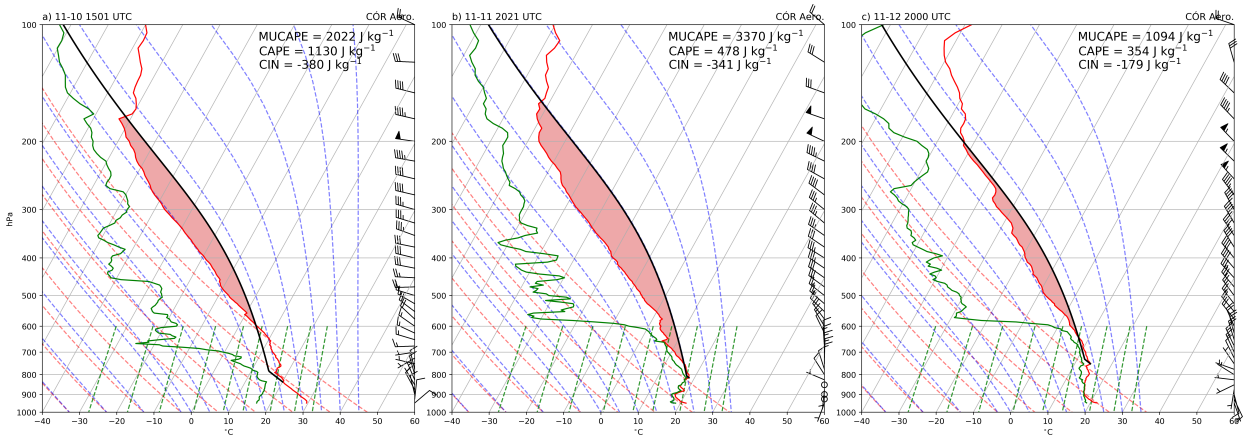

FIG. 3.17. Skew-T log-P diagrams from three soundings launched at 1501 10 Nov. (a), 2021 11 Nov. (b), and 2000 12 Nov. (c) 2018 from Córdoba City Airport. Pressure (hPa) and °C serve as the vertical and horizontal coordinates, respectively. Wind barbs on the right of each Skew-T diagram indicate direction and speed, where a long tick represents 10 m s^{-1} and a short tick 5 m s^{-1}. Temperature (dewpoint temperature) is plotted in red (green) and the most unstable parcel path in black; areas of MUCAPE are shaded in red. Values of MUCAPE, CAPE, and CIN are shown in the upper-right corner. Moist adiabats, dry adiabats, and mixing lines are represented by dashed lines of blue, red, and green, respectively.

During RELAMPAGO, numerous mobile sounding vehicles were deployed to collect soundings at high temporal resolution; here hourly soundings from one of those units (SCOUT2) located in Córdoba during 2300-0600 UTC 11-12 November, provide a brief window of high-resolution vertical profiles to provide insight into the evolution of the vertical wind shear and its connection to the development of upscale growth. Specifically, we analyze the meridional wind component derived from these soundings (Fig. 3.18a) relative to the reanalysis (Fig. 3.18b). The observation shows an elevated strong northerly SALLJ centered near 700 hPa persisted throughout the timeframe with wind speeds approaching 20 m s^{-1} while low-level southerly flow below 850 hPa maximized at 0300 UTC with speeds near 10 m s^{-1} (Fig. 3.18a). ERA5 reanalysis generally represents the observed strong vertical wind shear (Fig. 3.18b) that provides confidence in the synoptic composite analysis presented in the previous section. However, the representation of the nocturnal northerly SALLJ maximum is too weak and is likely due

to a well-known issue associated with the low vertical resolution in reanalyses in general. The low-level southerly flow was also slightly weaker and more elevated compared to the observations (Fig. 3.18a,b). Overall, there was persistent and robust mid-level vertical wind shear throughout the second convective upscale growth episode due to the juxtaposition of the northerly SALLJ and southerly flow associated with the western edge of the lee trough.

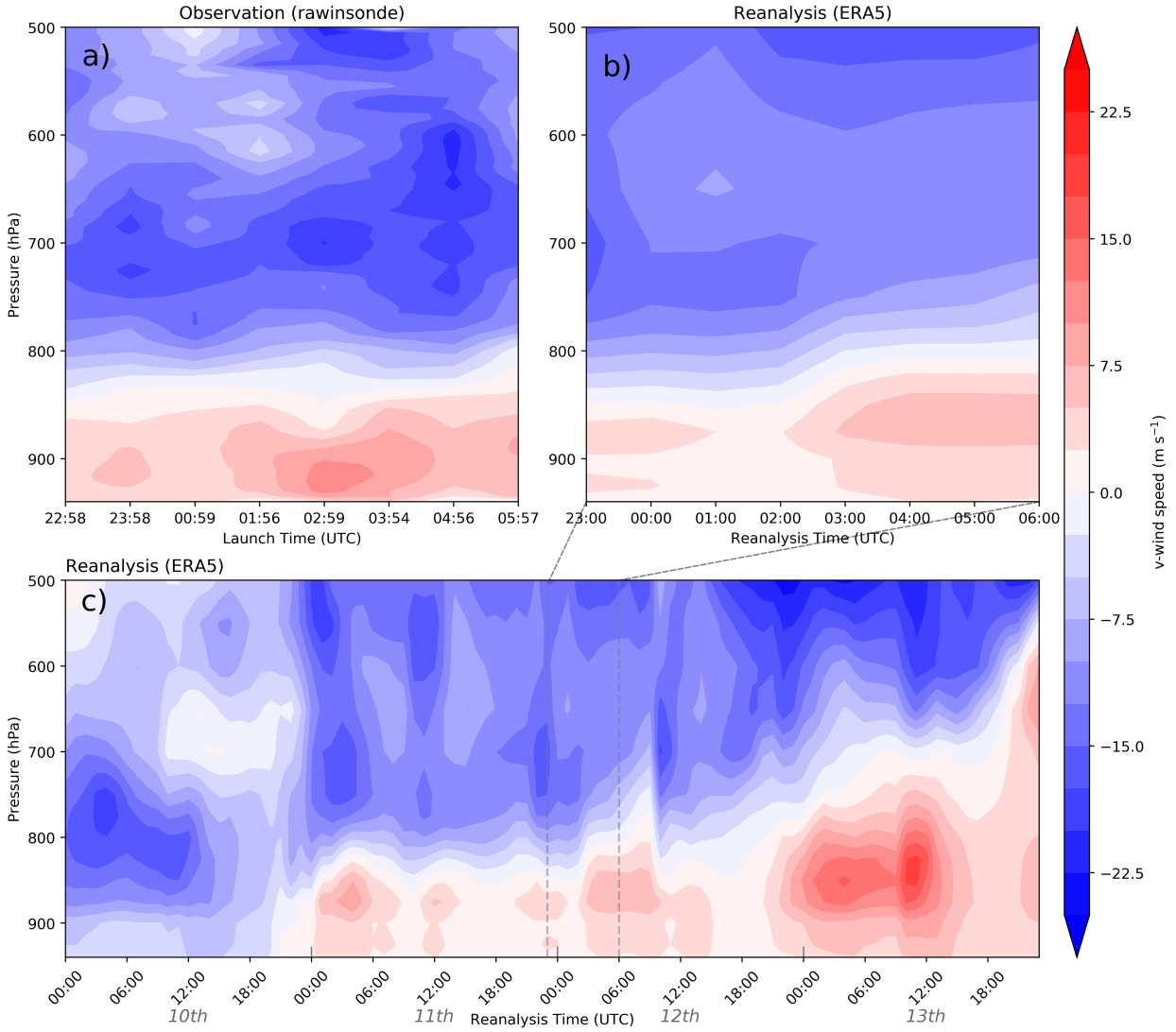

FIG. 3.18. Meridional wind speed at mobile unit SCOUT2 (31.113°S, 64.138°W) via hourly sounding launches from 2258 UTC 10 Nov. to 0537 UTC 11 Nov. (a), hourly ERA5 reanalysis from 2300 UTC 10 Nov. to 0600 UTC 11 Nov. (b), and hourly ERA5 reanalysis during 10-13 Nov. 2018 (c). Panel (b) is a subset of (c) as indicated by dashed black lines. ERA5 pressure levels are interpolated to every 5 hPa as in the observational sounding data.

To provide a broader view of the vertical distribution of meridional winds extending well before and after the period of high-resolution observations shown in Figure 3.18a, ERA5 reanalysis is used to

examine the period from 0000 UTC 10 November through 0000 UTC 14 November (Fig. 3.18c). Reanalysis suggests that a SALLJ maximum near 800 hPa on the 10th was shifted aloft under the low-level southerly flow just before 0000 UTC 11 November (Fig. 3.18c). Nocturnal maxima in the low-level southerly wind occurred 11-13 November (local time = UTC-3), aligning with the onset of the convective episodes discussed in this study (Figs. 3.13, 3.14). The final southerly wind pulse on the 13th was much more robust, likely induced by the cold front passing over Córdoba (Fig. 3.18c). With the lee trough moving through the region (Fig. 3.11), the SALLJ shifted northwest of Córdoba (not shown) and is no longer observable at this time (Fig. 3.18c).

3.5 Discussion

The work presented in the current and preceding sections adds significant insight to the generation and maintenance of organized convection in SSA relative to North America. In the U.S., MCS development is generally associated with strong vertical wind shear where the southerly flow of the LLJ intercepts westerly flow of a frontal area aloft (Laing and Fritsch 2000; Coniglio et al. 2010; Peters and Schumacher 2015). Additionally, elevated nocturnal convection initiation often takes place in large-scale baroclinic regions above a stable boundary layer (Geerts et al. 2017). The recurrence of strong capping inversions and unstable environments that allow for multi-day outbreaks, as exhibited by this November case, is not common in the U.S. because traditionally evaporative cooling from stratiform and convective precipitation restores stability to the environment and decays the MCS (Maddox 1983). When multi-day outbreaks of MCSs do occur, it is during quasi-stationary synoptic conditions that allow for persistent favorable environments via convective feedbacks (Stensrud 1996; Chasteen et al. 2019).

Multi-day convective outbreaks in South America are similar in the sense that quasi-stationary synoptic waves also lead to persistent westerly flow over the Andes and a SALLJ from the Amazon that contribute to instability and capping inversions; however, the extreme height of the Andes forces the flow further aloft such that the low- to mid-level shear may be more important for organizing storms in South America. Southerly flow as a result of lee cyclogenesis and the eastward propagation of the cyclone delivers cold, stable air at the low-levels towards the terrain of the La Plata Basin where ingredients for convection initiation have persisted for many hours. This stable boundary layer elevates the SALLJ which rapidly enhances vertical wind shear during the night. Rather than a front or shortwave trough, terrain often initiates convection in the afternoon/evening such that storms originate

further westward. After storms grow upscale at night, the quasi-stationary synoptic forcing that allows nocturnal elevated convection to persist into the daytime likely explains the longer lifetimes of South American MCSs relative to North American ones (Durkee et al. 2009; Durkee and Mote 2010). Within this large-scale environment, back-building (Rasmussen and Houze 2011, 2016) and upstream propagation (Anabor et al. 2008, 2009) in addition to multi-scale interactions that occur in the U.S. MCSs (Chasteen et al. 2019) that are also likely true in Argentina further act to prolong convective episodes. This multi-day setup seems to occur much more frequently in South America than in the U.S. likely owing to the low-level vertical wind shear and terrain-induced convection that will always occur if a deep enough trough passes over the Andes.

The work presented herein expounds on the conceptual model for convective initiation in SSA from Rasmussen and Houze (2016) using TRMM to come to new conclusions regarding the relationships between areal extent of organized convection, seasonality, and the magnitude of synoptic-scale forcing. Furthermore, reanalysis and observations from an event during RELAMPAGO suggest that synoptic waves and thus ingredients for convective initiation are quasi-stationary during multi-day outbreaks. In addition to back-building and upstream propagating convection (Anabor et al. 2008, 2009; Rasmussen and Houze 2011; Rasmussen et al. 2014), there is unique formation of strong mid-level vertical wind shear east of the mountainous terrain in this region; all of these phenomena likely explain why multi-day events are much more common in SSA compared to the U.S. Additional detailed analysis is required to adequately differentiate mechanisms between continents, however.

3.6 Conclusions

The current study compares the synoptic forcing that supports the largest (≥90th percentile) and the smallest (≤10th percentile in area) WCCs in the La Plata Basin during DJF and SON using TRMM PR to identify WCCs and ERA5 reanalysis to create composites of meteorological variables. Generally, the synoptic evolution associated with large WCCs is similar among seasons: an anomalous mid-level trough impinges upon the Andes Mountains from the west multiple days prior to WCC identification in the La Plata Basin, leading to an anomalous low-level lee trough over Argentina. This induces a meridional pressure gradient force associated with the geopotential height difference and enhances the terrain-funnelled, northerly SALLJ which advects low-level moisture from the Amazon into Argentina before and during the formation of WCCs. Aloft, the left-entrance region of a 250-hPa jet streak over the La Plata Basin causes synoptic-scale forcing for ascent. The impinging trough crossing the Andes

induces lee cyclogenesis through potential vorticity conservation and the eastward propagation of the lee cyclone away from the mountains produces a southerly wind shift on the western edge of the lee cyclone and low-level convergence opposing the SALLJ. This evolution and decay of synoptic environments favorable for large WCCs lasts about six days as mountain blocking and downstream ridge amplification over the Atlantic slow synoptic wave propagation.

The scale of synoptic forcing for large WCCs differs between seasons: the anomalies of the impinging 500- and 850-hPa troughs, 850-hPa lee trough, 250-hPa wind, and SALLJ at 850 hPa are all substantially greater in SON. In addition to greater synoptic activity during the spring in general, there appears to be an influence of the impinging trough shifting poleward from SON to DJF; since the height of the Andes decreases poleward, flow blocking, and thus leeside synoptic forcing, decreases into the summer. Furthermore, a reduction in mountain height and flow blocking decreases CAPE and CIN downstream (Rasmussen and Houze 2016). Despite differences in large-scale environments between spring and summer, the number of large SON and DJF WCCs is almost equal. Thus, terrain and local processes must be important in initiating DJF WCCs (Romatschke and Houze 2010; Rasmussen and Houze 2011, 2016). Our finding that ingredients of ascent and upscale growth are more favorable along the western terrain during DJF aligns with this theory and is consistent with Rasmussen et al. (2016) who found that SON WCC peak frequency and contribution to rainfall are farther east relative to DJF.

Synoptic forcing generally decreases for small WCCs of both seasons. However, while SON still features a 250-hPa wind maximum, DJF lacks an anomalous jet streak over Argentina at any point in the large-scale evolution. A weak impinging trough does lead to a slight low-level lee trough during DJF, but the magnitude of the anomaly is approximately half the magnitude of the SON anomaly. This dearth of robust synoptic forcing for small WCC accentuates the role of terrain in initiating and organizing summertime convection.

To exemplify these findings, we analyze a large and very long-lasting case from the RELAMPAGO field campaign that spawned multiple MCSs while back-building and propagating upstream over the course of four days. Its synoptic evolution followed the large WCC composite, but with much greater anomaly magnitudes and slower synoptic wave propagation speeds that enabled a persistent unstable environment over the La Plata Basin. Three upscale growth episodes in northern Argentina lasting approximately 24 hrs occurred in a row following maxima in MUCAPE and CIN and exemplified the conceptual model of Rasmussen and Houze (2016). Their model, however, leaves out the importance of mid-level vertical wind shear in initiating and organizing convection in the region. In the U.S.,

MCS-organizing vertical wind shear mainly develops at the intersection of a front and LLJ (Laing and Fritsch 2000; Coniglio et al. 2010; Peters and Schumacher 2015); in SSA, however, this case and the synoptic composites presented herein suggest that enhanced vertical wind shear results from the juxtaposition of the southerly flow induced by the lee cyclone and the northerly SALLJ. Since convection is often initiated along and tied to the Andes foothills and the SDC, MCSs in SSA tend to mature closer to mountainous terrain than in the U.S. A slowly propagating synoptic trough impinging upon the Andes precedes the most widespread upscale growth cases; as it becomes quasi-stationary as MCS size increases, moisture flux and mid-level vertical wind shear can persist for multiple days leading to consecutive convective outbreaks. Because quasi-stationary synoptic waves are rare in the U.S. relative to near the Andes, these multi-day outbreaks occur infrequently.

While this study substantially expands our knowledge regarding MCS storm environments in one of the world's convective hotspots using new ground-based observations from RELAMPAGO, there is still much to learn about mesoscale processes that contribute to the longevity of organized convection. These data provide many opportunities for future work such as investigating the precise roles of gravity waves, cold pools, and terrain interactions on back-building and upstream propagation in the context of these large-scale environments using radar data and mobile soundings. Continued understanding of these MCSs that threaten the socioeconomic livelihood of a large region in the current climate is crucial for determining how their impacts will change in the future. SSA is a mere example of one of the most convectively active locations on the planet that historically has lacked ground-based observations. Though TRMM has proven useful for similar regions such as central Africa and the Himalayas, the current study makes it clear that high-resolution in situ measurements reveal phenomena that remote sensing cannot. Thus, the authors hope this work encourages further global collaboration to acquire the needed ground observations for robust investigations of unique and threatening phenomena worldwide in this ever-changing climate.

CHAPTER 4

CONCLUSIONS

East of the Andes of South America and the Rockies of North America are global hotspots of convection. As a result, hazardous weather, such as large hail, floods, and tornadoes regularly impacts people and property of these regions. While the same general ingredients lead to widespread thunderstorms in each continent, numerical weather models struggle more to predict those in South America, which tend to be larger and longer-lasting. Previous studies using satellite radar attribute this intensity difference to the region's complex terrain; however, the RELAMPAGO field campaign of 2018 allows for a more deterministic analysis as it provides the first ground-based observation dataset targeting thunderstorms in north-central Argentina. The resulting research will not just improve the prediction of severe storms here, but can also be applied elsewhere to similar regions of the world like the Himalayas or northern Africa.

This thesis consists of two studies that will improve the prediction of hazardous weather in subtropical South America utilizing these new data, particularly by diagnosing causes of model forecast error relative to North America and evaluating the synoptic and mesoscale forcing for large thunderstorms in the La Plata Basin. As hypothesized, the error associated with warm-season environments, including specific convective events, is greater in South America. Most notably, simulations over South America feature a dry bias at the mid-levels of the atmosphere such that the timing and scale of convection is miscalculated. This is most likely due to the coarse model resolution inadequately capturing the extreme height and unique foothills of the Andes, leading to a poor model representation of the depth of the SALLJ that in reality advects non-negligible moisture up to 700 hPa.

Cases during RELAMPAGO exemplified the inaccurate model portrayal of synoptic phenomena in addition to the mesoscale. For example, simulated anomalously deep mid-level troughs propagate over the Andes too rapidly, leading to an earlier (and weaker) onset of convection over the La Plata Basin. The synoptic evolution analysis presented herein provides a better understanding of the large-scale influence variability on widespread convection between seasons. Interestingly, while a similar number of thunderstorms occur in the austral spring and summer over the La Plata Basin, synoptic forcing is greater and further away from the terrain during the spring. This indicates that terrain plays a more important role in initiating convection during the summer. Furthermore, southerly return flow

from the passage of the lee cyclone initiates convergence and strong vertical wind shear over the La Plata Basin.

The work presented within this thesis adds substantial knowledge to the climatology and the day-to-day forecasting of severe thunderstorms in subtropical South America, both of which vital for decision-makers who are responsible for saving lives and property. The RELAMPAGO field campaign has already proved to be extremely useful because 1) it provides data necessary to draw conclusions on convective processes in a remote but convective-rich region of the world, but it also 2) accentuates the importance of global collaboration as face the mysteries of an ever-changing climate. In order to predict how dangerous phenomena will evolve, it is necessary to first grasp their mechanisms of today. The Himalayas and central Africa like subtropical South America face frequent hazardous weather but lack robust datasets capable of dissecting key processes. It is the hope that in the wake of climate change and technological advances, there are continued inclusive efforts such as RELAMPAGO to address the phenomena that threaten the livelihood of the global community.

REFERENCES

Anabor, V., D. J. Stensrud, and O. L. de Moraes, 2008: Serial upstream-propagating mesoscale convective system events over southeastern South America. *Mon. Wea. Rev.*, **136**, 3087–3105, doi: 10.1175/2007MWR2334.1.

Anabor, V., D. J. Stensrud, and O. L. de Moraes, 2009: Simulation of a serial upstream-propagating mesoscale convective system event over southeastern South America using composite initial conditions. *Mon. Wea. Rev.*, **137 (7)**, 2144–2163, doi: 10.1175/2008MWR2617.1.

Augustine, J. A. and K. W. Howard, 1988: Mesoscale convective complexes over the United States during 1985. *Mon. Wea. Rev.*, **116 (3)**, 685–701.

Blázquez, J. and M. N. Nuñez, 2009: Sensitivity to convective parameterization in the WRF regional model in southern South America. 9th Int. Conf. Southern Hemisphere Meteorology and Oceanography, Melbourne, AU. *Amer. Meteor. Soc. and Aus. Meteor. Ocean. Soc.*, 1–6.

Bonner, W. D., 1968: Climatology of the low level jet. *Mon. Wea. Rev.*, **96 (12)**, 833–850, doi: 10.1175/1520-0493(1968)096<0833:COTLLJ>2.0.CO;2.

Bruick, Z. S., K. L. Rasmussen, and D. J. Cecil, 2019: Subtropical South American hailstorm characteristics and environments. *Mon. Wea. Rev.*, **147 (12)**, 4289–4304, doi: 10.1175/MWR-D-19-0011.1.

Bryan, G. H., J. C. Wyngaard, and J. M. Fritsch, 2003: Resolution requirements for the simulation of deep moist convection. *Mon. Wea. Rev.*, **131 (10)**, 2394–2416, doi: 10.1175/1520-0493(2003)131<2394:RRFTSO>2.0.CO;2.

Carlson, T. N., S. G. Benjamin, G. S. Forbes, and Y.-F. Li, 1983: Elevated mixed layers in the regional severe storm environment: Conceptual model and case studies. *Mon. Wea. Rev.*, **111**, 1453–1474, doi: 10.1175/1520-0493(1983)111<1453:EMLITR>2.0.CO;2.

Cecil, D. J. and C. B. Blankenship, 2012: Toward a global climatology of severe hailstorms as estimated by satellite passive microwave imagers. *J. Climate*, **25**, 687–703, doi: 10.1175/JCLI-D-11-00130.1.

Chasteen, M. B., S. E. Koch, and D. B. Parsons, 2019: Multiscale processes enabling the longevity and daytime persistence of a nocturnal mesoscale convective system. *Mon. Wea. Rev.*, **147 (2)**, 733–761, doi: 10.1175/MWR-D-18-0233.1.

Chung, Y.-S., 1977: On the orographic influence and lee cyclogenesis in the Andes, the Rockies and the east Asian mountains. *Archiv für Meteorologie, Geophysik und Bioklimatologie, Serie A*, **26 (1)**, 1–12, doi: 10.1007/BF02246530.

Clark, A. J. and Coauthors, 2012: An overview of the 2010 Hazardous Weather Testbed experimental forecast program spring experiment. *Bull. Amer. Meteor. Soc.*, **93**, 55–74, doi: 10.1175/BAMS-D-11-00040.1.

Clark, A. J., W. A. Gallus Jr, and T.-C. Chen, 2007: Comparison of the diurnal precipitation cycle in convection-resolving and non-convection-resolving mesoscale models. *Mon. Wea. Rev.*, **135**, 3456–3473, doi: 10.1175/MWR3467.1.

Clark, A. J., W. A. Gallus Jr, M. Xue, and F. Kong, 2009: A comparison of precipitation forecast skill between small convection-allowing and large convection-parameterizing ensembles. *Wea. Forecasting*, **24**, 1121–1140, doi: 10.1175/2009WAF2222222.1.

Coniglio, M. C., J. Y. Hwang, and D. J. Stensrud, 2010: Environmental factors in the upscale growth and longevity of mcss derived from rapid update cycle analyses. *Mon. Wea. Rev.*, **138 (9)**, 3514–3539, doi: 10.1175/2010MWR3233.1.

Coniglio, M. C., D. J. Stensrud, and L. J. Wicker, 2006: Effects of upper-level shear on the structure and maintenance of strong quasi-linear mesoscale convective systems. *J. Atmos. Sci.*, **63 (4)**, 1231–1252.

Cordeira, J. M., N. D. Metz, M. E. Howard, and T. J. Galarneau Jr, 2017: Multiscale upstream and in situ precursors to the elevated mixed layer and high-impact weather over the Midwest United States. *Wea. Forecasting*, **32**, 905–923, doi: 10.1175/WAF-D-16-0122.1.

Davis, C. A., 1997: The modification of baroclinic waves by the Rocky Mountains. *J. Atmos. Sci.*, **54 (7)**, 848–868, doi: 10.1175/1520-0469(1997)054<0848:TMOBWB>2.0.CO;2.

Davis, C. A., K. W. Manning, R. E. Carbone, S. B. Trier, and J. D. Tuttle, 2003: Coherence of warm-season continental rainfall in numerical weather prediction models. *Mon. Wea. Rev.*, **131**, 2667–2679, doi: 10.1175/1520-0493(2003)131<2667:COWCRI>2.0.CO;2.

Durkee, J. D. and T. L. Mote, 2010: A climatology of warm-season mesoscale convective complexes in subtropical South America. *Int. J. Climatology*, **30 (3)**, 418–431, doi: 10.1002/joc.1893.

Durkee, J. D., T. L. Mote, and J. M. Shepherd, 2009: The contribution of mesoscale convective complexes to rainfall across subtropical South America. *J. Climatol.*, **22 (17)**, 4590–4605.

Fritsch, J. M., R. J. Kane, and C. R. Chelius, 1986: The contribution of mesoscale convective weather systems to the warm-season precipitation in the United States. *J. Climate Appl. Meteor.*, **25**, 1333–1345, doi: 10.1175/1520-0450(1986)025<1333:TCOMCW>2.0.CO;2.

Gan, M. A. and V. B. Rao, 1994: The influence of the Andes Cordillera on transient disturbances. *Mon. Wea. Rev.*, **122 (6)**, 1141–1157, doi: 10.1175/1520-0493(1994)122<1141:TIOTAC>2.0.CO;2.

Garreaud, R. and J. M. Wallace, 1998: Summertime incursions of midlatitude air into subtropical and tropical South America. *Mon. Wea. Rev.*, **126 (10)**, 2713–2733.

Geerts, B., et al., 2017: The 2015 Plains Elevated Convection at Night Field Project. *Bull. Amer. Meteor. Soc.*, **98 (4)**, 767–786, doi: 10.1175/BAMS-D-15-00257.1.

Gotway, J. H. and Coauthors, 2018: Model evaluation tools version 8.0 (METv8.0). Dev. Testbed Ctr., Boulder, CO.

Grell, G. A. and S. R. Freitas, 2014: A scale and aerosol aware stochastic convective parameterization for weather and air quality modeling. *Atmos. Chem. Phys.*, **14**, 5233–5250, doi: 10.5194/acp-14-5233-2014.

Grenier, H. and C. S. Bretherton, 2001: A moist PBL parameterization for large-scale models and its application to subtropical cloud-topped marine boundary layers. *Mon. Wea. Rev.*, **129**, 357–377, doi: 10.1175/1520-0493(2001)129<0357:AMPPFL>2.0.CO;2.

Guedes do Nascimento, M., D. L. Herdies, and D. Oliveira de Souza, 2016: The South American water balance: the influence of low-level jets. *J. Climate*, **29 (4)**, 1429–1449, doi: 10.1175/JCLI-D-15-0065.1.

Haberlie, A. M. and W. S. Ashley, 2019: A radar-based climatology of mesoscale convective systems in the United States. **32 (5)**, 1591–1606.

Hong, S.-Y. and J.-. J. Lim, 2006: The WRF single-moment 6-class microphysics scheme (WSM6). *J. Korean Meteor. Soc.*, **42**, 129–151.

Hong, S.-Y., Y. Noh, and J. Dudhia, 2006: A new vertical diffusion package with an explicit treatment of entrainment processes. *Mon. Wea. Rev.*, **134**, 2318–2341.

Houze, R. A., 2004: Mesoscale convective systems. *Rev. Geophys.*, **42 (4)**, doi: 10.1029/2004RG000150.

Houze, R. A., K. L. Rasmussen, and S. R. Zuluaga, M D Brodzik, 2008: Radiative forcing by long-lived greenhouse gases: Calculations with the AER radiative transfer models. *J. Geophys. Res.*, **113**, D13 103, doi: 10.1029/2008JD009944.

Houze, R. A., K. L. Rasmussen, and S. R. Zuluaga, M D Brodzik, 2015: The variable nature of convection in the tropics and subtropics: A legacy of 16 years of the Tropical Rainfall Measuring Mission satellite. *Rev. Geophys.*, **53**, 994–1021, doi: 10.1002/2015RG000488.

Iguchi, T., T. Kozu, J. Kwiatkowki, R. Meneghini, J. Awaka, and K. Okamoto, 2009: Uncertainties in the rain profiling algorithm for the TRMM precipitation radar. *J. Meteor. Soc. Japan*, **87A**, 1–30.

Iguchi, T., T. Kozu, R. Meneghini, J. Awaka, and K. Okamoto, 2000: Rain-profiling algorithm for the TRMM precipitation radar. *J. Appl. Meteor.*, **39 (12)**, 2038–2052.

Insel, N., C. J. Poulsen, and T. A. Ehlers, 2010: The influence of the Andes Mountains on South American moisture transport, convection, and precipitation. *Clim. Dyn.*, **35**, 1477–1492, doi: 10.1007/s00382-009-0637-1.

Iyer, E. R., A. J. Clark, M. Xue, and F. Kong, 2016: A comparison of 36–60-h precipitation forecasts from convection-allowing and convection-parameterizing ensembles. *Wea. Forecasting*, **31**, 647–661, doi: 10.1175/WAF-D-15-0143.1.

Janjić, Z. I., 1994: The step-mountain eta coordinate model: Further developments of the convection, viscous sublayer and turbulence closure schemes. *Mon. Wea. Rev.*, **122**, 927–945, doi: 10.1175/1520-0493(1994)122<0927:TSMECM>2.0.CO;2.

Jankov, I., W. A. Gallus, M. Segal, B. Shaw, and S. E. Koch, 2005: The impact of different WRF Model physical parameterizations and their interactions on warm season MCS rainfall. *Wea. Forecasting*, **20**, 1048–1060, doi: 10.1175/WAF888.1.

Jeworrek, J., G. West, and R. Stull, 2019: Evaluation of cumulus and microphysics parameterizations in WRF across the convective gray zone. *Wea. Forecasting*, **34 (4)**, 1097–1115.

Kain, J., 2004: The Kain-Fritsch convective parameterization: An update. *J. Appl. Meteor.*, **43**, 170–181, doi: 10.1175/1520-0450(2004)043<0170:TKCPAU>2.0.CO;2.

Kalnay, E. and Coauthors, 1996: The NCEP/NCAR 40-year reanalysis project. *Bull. Amer. Meteor. Soc.*, **77**, 437–471, doi: 10.1175/1520-0477(1996)077<0437:TNYRP>2.0.CO;2.

Kasahara, A., 1966: The dynamical influence of orography on the large-scale motion of the atmosphere. *J. Atmos. Sci.*, **23 (3)**, 259–271.

Kumjian, M. R., S. W. Nesbitt, P. Maldonado, L. M. Luna, J. Marquis, K. A. Bowley, M. A. Imaz, and P. Salio, 2020: Gargantuan hail in Argentina. *Bull. Amer. Meteor. Soc.*, doi: 10.1175/BAMS-D-19-0012.1.

Kummerow, C., W. Barnes, T. Kozu, J. Shiue, and J. Simpson, 1998: The tropical rainfall measuring mission (TRMM) sensor package. *J. Atmos. Oceanic Technol.*, **15 (3)**, 809–817, doi: 10.1175/1520-0426(1998)015<0809:TTRMMT>2.0.CO;2.

Laing, A. and J. Fritsch, 1997: The global population of mesoscale convective complexes. *Quart. J. Roy. Meteor. Soc.*, **123**, 389–405, doi: 10.1002/qj.49712353807.

Laing, A. G. and J. M. Fritsch, 2000: The large-scale environments of the global populations of mesoscale convective complexes. *Mon. Wea. Rev.*, **128 (8)**, 2756–2776, doi: 10.1175/1520-0493(2000)128<2756:TLSEOT>2.0.CO;2.

Lin, Y. and K. Mitchell, 2005: The NCEP Stage II/IV hourly precipitation analyses: Development and applications. *19th Conf. on Hydrology , San Diego, CA, Amer. Meteor. Soc*, 1.2.

Liu, C., M. Moncrieff, J. Tuttle, and R. Carbone, 2006: Explicit and parameterized episodes of warm-season precipitation over the continental United States. *Adv. Atmos. Sci.*, **23**, 91–105.

Maddox, R. A., 1980: Mesoscale convective complexes. *Bull. Amer. Meteor. Soc.*, **61**, 1374–1387, doi: 10.1175/1520-0477(1980)061<1374:MCC>2.0.CO;2.

Maddox, R. A., 1983: Large-scale meteorological conditions associated with midlatitude, mesoscale convective complexes. *Mon. Wea. Rev.*, **111**, 1475–1493, doi: 10.1175/1520-0493(1983)111<1475:LSMCAW>2.0.CO;2.

Maltzahn, C. and Coauthors, 2016: The Big Weather Web: A common and sustainable big data infrastructure in support of weather prediction research and education in universities. doi: http://bigweatherweb.org.

Marengo, J., M. Douglas, and P. Silva Dias, 2002: The South American low level jet east of the Andes during the 1999 LBATRMM and LBA-WET AMC campaign. *J. Geophys. Res.*, **107**, 8079, doi: doi.org/10.1029/2001JD001188.

Marengo, J., W. Soares, C. Saulo, and M. Nicolini, 2004: Climatology of the low-level jet east of the Andes as derived from the NCEP–NCAR reanalyses: Characteristics and temporal variability. *J. Climate*, **17**, 2261–2280, doi: 10.1175/1520-0442(2004)017<2261:COTLJE>2.0.CO;2.

Matsudo, C. and P. V. Salio, 2011: Severe weather reports and proximity to deep convection over Northern Argentina. *Atmos. Res.*, **100 (4)**, 523–537, doi: 10.1016/j.atmosres.2010.11.004.

Milbrandt, J. and M. Yau, 2005: A multimoment bulk microphysics parameterization. part i: Analysis of the role of the spectral shape parameter. *J. Atmos. Sci.*, **62 (9)**, 3051–3064, doi: 10.1175/JAS3534.1.

Morrison, H., G. Thompson, and V. Tatarskii, 2009: Impact of cloud microphysics on the development of trailing stratiform precipitation in a simulated squall line: Comparison of one-and two-moment schemes. *Mon. Wea. Rev.*, **137 (3)**, 991–1007, doi: 10.1175/2008MWR2556.1.

Mulholland, J. P., S. W. Nesbitt, R. J. Trapp, K. L. Rasmussen, and P. V. Salio, 2018: Convective storm life cycle and environments near the Sierras de Córdoba, Argentina. *Mon. Wea. Rev.*, **146 (8)**, 2541–2557, doi: 10.1175/MWR-D-18-0081.1.

Müller, O. V., M. A. Lovino, and E. H. Berbery, 2016: Evaluation of WRF model forecasts and their use for hydroclimate monitoring over southern South America. *Wea. Forecasting*, **31 (3)**, 1001–1017, doi: 10.1175/WAF-D-15-0130.1.

Nakanishi, M. and H. Niino, 2009: Development of an improved turbulence closure model for the atmospheric boundary layer. *J. Meteor. Soc. Japan*, **87 (5)**, 895–912, doi: 10.2151/jmsj.87.895.

NCEP, 2004: NCEP ADP global upper air observational weather data, october 1999 - continuing. Research Data Archive at the National Center for Atmospheric Research, Computational and Information Systems Laboratory, Boulder CO, URL https://doi.org/10.5065/39C5-Z211.

Nesbitt, S. W., R. Cifelli, and S. A. Rutledge, 2006: Storm morphology and rainfall characteristics of TRMM precipitation features. *Mon. Wea. Rev.*, **134 (10)**, 2702–2721, doi: 10.1175/MWR3200.1.

Oliveira, M. I., E. L. Nascimento, and C. Kannenberg, 2018: A new look at the identification of low-level jets in South America. *Mon. Wea. Rev.*, **146 (7)**, 2315–2334, doi: 10.1175/mwrâĂŘdâĂŘ17âĂŘ0237.1.

Petch, J., 2006: Sensitivity studies of developing convection in a cloud-resolving model. *Quart. J. Roy. Meteor. Soc.*, **132 (615)**, 345–358, doi: 10.1256/qj.05.71.

Peters, J. M. and R. S. Schumacher, 2015: Mechanisms for organization and echo training in a flash-flood-producing mesoscale convective system. *Mon. Wea. Rev.*, **143 (4)**, 1058–1085, doi: 10.1175/MWR-D-14-00070.1.

Piersante, J. O., R. S. Schumacher, and K. L. Rasmussen, 2020: Comparison of biases in warm-season WRF forecasts in North and South America. *Submitted to Wea. Forecasting*.

Pleim, J. E., 2007: A combined local and nonlocal closure model for the atmospheric boundary layer. Part I: Model description and testing. *J. Appl. Meteor. Climatol.*, **46 (9)**, 1383–1395, doi: 10.1175/JAM2539.1.

Porter, J. M., L. Means, J. Hovde, and W. Chappell, 1955: A synoptic study on the formation of squall lines in the north central United States. *Bull. Amer. Meteor. Soc.*, **36 (8)**, 390–396, doi: 10.1175/1520-0477-36.8.390.

Rasmussen, K., M. Chaplin, M. Zuluaga, and R. Houze Jr, 2016: Contribution of extreme convective storms to rainfall in South America. *J. Hydrometeor.*, **17 (1)**, 353–367, doi: 10.1175/JHM-D-15-0067.1.

Rasmussen, K. L. and R. A. Houze, 2011: Orogenic convection in subtropical South America as seen by the TRMM satellite. *Mon. Wea. Rev.*, **139 (8)**, 2399–2420, doi: 10.1175/MWR-D-10-05006.1.

Rasmussen, K. L. and R. A. Houze, 2016: Convective initiation near the andes in subtropical South America. *Mon. Wea. Rev.*, **144 (6)**, 2351–2374, doi: 10.1175/MWR-D-15-0058.1.

Rasmussen, K. L., M. D. Zuluaga, and R. A. Houze Jr, 2014: Severe convection and lightning in subtropical South America. *Geophys. Res. Lett.*, **41 (20)**, 7359–7366, doi: 10.1002/2014GL061767.

Ribeiro, B. Z. and L. F. Bosart, 2018: Elevated mixed layers and associated severe thunderstorm environments in South and North America. *Mon. Wea. Rev.*, **146 (1)**, 3–28, doi: 10.1175/MWR-D-17-0121.1.

Roebber, P. J., 2009: Visualizing multiple measures of forecast quality. *Wea. Forecasting*, **24 (2)**, 601–608, doi: 10.1175/2008WAF2222159.1.

Romatschke, U. and R. A. Houze, 2010: Extreme summer convection in South America. *J. Climate*, **23 (14)**, 3761–3791, doi: 10.1175/2010JCLI3465.1.

Ruiz, J. J., C. Saulo, and J. Nogués-Paegle, 2010: WRF model sensitivity to choice of parameterization over South America: validation against surface variables. *Mon. Wea. Rev.*, **138 (8)**, 3342–3355, doi: 10.1175/2010MWR3358.1.

Salio, P., M. Nicolini, and A. C. Saulo, 2002: Chaco low-level jet events characterization during the austral summer season. *J. Geophys. Res.*, **107 (D24)**, ACL–32, doi: 10.1019/2001JD001315.

Salio, P., M. Nicolini, and E. J. Zipser, 2007: Mesoscale convective systems over southeastern South America and their relationship with the South American low-level jet. *Mon. Wea. Rev.*, **135 (4)**, 1290–1309, doi: 10.1175/MWR3305.1.

Satyamurty, P., C. Ferreria, and M. A. Gan, 1990: Cyclonic vortices over South America. *Tellus*, **42 (1)**, 194–201, doi: 10.1034/j.1600-0870.1990.00016.x.

Schultz, D. M. and C. A. Doswell III, 2000: Analyzing and forecasting Rocky Mountain lee cyclogenesis often associated with strong winds. *Wea. Forecasting*, **15 (2)**, 152–173, doi: 10.1175/1520-0434(2000)015<0152:AAFRML>2.0.CO;2.

Schumacher, R. S. and A. J. Clark, 2014: Evaluation of ensemble configurations for the analysis and prediction of heavy-rain-producing mesoscale convective systems. *Mon. Wea. Rev.*, **142 (11)**, 4108–4138, doi: 10.1175/MWR-D-13-00357.1.

Schumacher, R. S. and C. A. Davis, 2010: Ensemble-based forecast uncertainty analysis of diverse heavy rainfall events. *Wea. Forecasting*, **25 (4)**, 1103–1122, doi: 10.1175/2010WAF2222378.1.

Schumacher, R. S. and R. H. Johnson, 2005: Organization and environmental properties of extreme-rain-producing mesoscale convective systems. *Mon. Wea. Rev.*, **133 (4)**, 961–976, doi: 10.1175/MWR2899.1.

Schumacher, R. S. and R. H. Johnson, 2006: Characteristics of US extreme rain events during 1999–2003. *Wea. Forecasting*, **21 (1)**, 69–85, doi: 10.1175/WAF900.1.

Schwartz, C. S., G. S. Romine, R. A. Sobash, K. R. Fossell, and M. L. Weisman, 2015: NCAR's experimental real-time convection-allowing ensemble prediction system. *Wea. Forecasting*, **30 (6)**, 1645–1654, doi: 10.1175/WAF-D-15-0103.1.

Service, C. C. C., 2017: ERA5: Fifth generation of ECMWF atmospheric reanalyses of the global climate.

Skamarock, W. C. and J. B. Klemp, 2008: A time-split nonhydrostatic atmospheric model for weather research and forecasting applications. *J. Comput. Phys.*, **227 (7)**, 3465–3485.

Smith, R. B., 1984: A theory of lee cyclogenesis. *J. Atmos. Sci.*, **41 (7)**, 1159–1168.

Smith, R. B., 1986: Further development of a theory of lee cyclogenesis. *J. Atmos. Sci.*, **43 (15)**, 1582–1602.

Stein, A., R. R. Draxler, G. D. Rolph, B. J. Stunder, M. Cohen, and F. Ngan, 2015: NOAA's HYSPLIT atmospheric transport and dispersion modeling system. *Bull. Amer. Meteor. Soc.*, **96 (12)**, 2059–2077, doi: 10.1175/BAMS-D-14-00110.1.

Stensrud, D. J., 1996: Effects of persistent, midlatitude mesoscale regions of convection on the large-scale environment during the warm season. *J. Atmos. Sci.*, **53 (23)**, 3503–3527, doi: 10.1175/1520-0469(1996)053<3503:EOPMMR>2.0.CO;2.

Stensrud, D. J. and J. M. Fritsch, 1993: Mesoscale convective systems in weakly forced large-scale environments. Part I: Observations. *Mon. Wea. Rev.*, **121 (12)**, 3326–3344.

Tewari, M., et al., 2004: Implementation and verification of the unified NOAH land surface model in the WRF model (formerly paper number 17.5). *Proceedings of the 20th Conference on Weather Analysis and Forecasting/16th Conference on Numerical Weather Prediction, Seattle, WA, USA*, 11–15.

Thompson, G., P. R. Field, R. M. Rasmussen, and W. D. Hall, 2008: Explicit forecasts of winter precipitation using an improved bulk microphysics scheme. Part II: Implementation of a new snow parameterization. *Mon. Wea. Rev.*, **136 (12)**, 5095–5115, doi: 10.1175/2008MWR2387.1.

Velasco, I. and J. M. Fritsch, 1987: Mesoscale convective complexes in the Americas. *J. Geophys. Res.*, **92 (D8)**, 9591–9613, doi: 10.1029/JD092iD08p09591.

Vera, C., et al., 2006: The South American low-level jet experiment. *Bull. Amer. Meteor. Soc.*, **87 (1)**, 63–78, doi: 10.1175/BAMS-87-1-63.

Weisman, M. L., W. C. Skamarock, and J. B. Klemp, 1997: The resolution dependence of explicitly modeled convective systems. *Mon. Wea. Rev.*, **125 (4)**, 527–548, doi: 10.1175/1520-0493(1997)125<0527:TRDOEM>2.0.CO;2.

Williams, E., 2018: Latitude/longitude distance calculator. *National Hurricane Center., accessed April*, **11**.

Zhang, C. and Y. Wang, 2017: Projected future changes of tropical cyclone activity over the western North and South Pacific in a 20-km-mesh regional climate model. *J. Climate*, **30 (15)**, 5923–5941, doi: 10.1175/JCLI-D-16-0597.1.

Zhang, C., Y. Wang, and K. Hamilton, 2011: Improved representation of boundary layer clouds over the southeast Pacific in ARW-WRF using a modified Tiedtke cumulus parameterization scheme. *Mon. Wea. Rev.*, **139 (11)**, 3489–3513, doi: 10.1175/MWR-D-10-05091.1.

Zipser, E. J., D. J. Cecil, C. Liu, S. W. Nesbitt, and D. P. Yorty, 2006: Where are the most intense thunderstorms on Earth? *Bull. Amer. Meteor. Soc.*, **87 (8)**, 1057–1072, doi: 10.1175/BAMS-87-8-1057.

Zuluaga, M. D. and R. A. Houze, 2013: Evolution of the population of precipitating convective systems over the equatorial Indian Ocean in active phases of the Madden–Julian oscillation. *J. Atmos. Sci.*, **70 (9)**, 2713–2725, doi: 10.1175/JAS-D-12-0311.1.